FAR-FIELD EVOLUTION OF TURBULENCE-EMITTED INTERNAL WAVES AND REYNOLDS NUMBER EFFECTS ON A LOCALIZED STRATIFIED TURBULENT FLOW

A Dissertation

Presented to the Faculty of the Graduate School

of Cornell University

in Partial Fulfillment of the Requirements for the Degree of

Doctor of Philosophy

by

Qi Zhou

August 2015

© 2015 QI ZHOU
ALL RIGHTS RESERVED

FAR-FIELD EVOLUTION OF
TURBULENCE-EMITTED INTERNAL WAVES
AND REYNOLDS NUMBER EFFECTS ON
A LOCALIZED STRATIFIED TURBULENT FLOW

Qi Zhou, Ph.D.
Cornell University 2015

In this dissertation, internal waves (IWs) and turbulence in the stably stratified ocean are studied via a series of numerical simulations. First of all, internal wave beams that are representative of high-mode internal tide originated from the ocean topography and constituent element of turbulence-emitted IWs are studied via direct numerical simulations (DNS), with an emphasis on their reflection at the sea surface as modelled by a free-slip rigid lid. Nonlinear effects due to wave-wave interaction, such as mean flow and harmonics, are investigated; in particular, the amplitude of the wave-driven Eulerian mean flow is found to match the theoretical prediction of an inviscid weakly nonlinear theory. The IW beams can also degrade at late time of reflection due to parametric subharmonic instability. Subsequent particle tracking is performed based the DNS dataset, in an attempt to examine the mass transport driven by the reflecting IW beams. These fully nonlinear computations reveal a horizontal dispersion of ocean tracers with a dispersivity scaling with $O(A^4)$, where A is the steepness of the IW beam, while small-amplitude analysis accurate to $O(A^2)$ suggests an exact cancellation of Eulerian mean flow due to wave-wave interaction and the wave-driven Stokes drift.

The second topic of the dissertation investigates the manifestation of submerged-turbulence-emitted IWs at the sea surface and the correlation between

the IW characteristics to turbulent source of IW. The turbulent wake of a sphere of diameter D towed at speed U is investigated using three-dimensional implicit large-eddy simulations, in a linearly stratified Boussinesq fluid with buoyancy frequency N and kinematic viscosity ν. Six simulations are performed at Reynolds numbers $Re \equiv UD/\nu \in \{5 \times 10^3,\ 10^5\}$ and Froude numbers $Fr \equiv 2U/(ND) \in \{4, 16, 64\}$, with the wave-emitting wake located at a fixed distance of $9D$ below the surface. As the wake evolves for up to $O(300)$ units of buoyancy time scale $1/N$, IW characteristics, such as horizontal wavelength λ_H and wave period T, are sampled at the sea surface via wavelet transforms of surface horizontal divergence signals. The statistics of amplitudes and orientations of IW-induced surface strains are also reported. The normalized mean observable wavelength $\overline{\lambda}_H/D$ at the sea surface decays in time as $(Nt)^{-1}$, which is due to the waves' dispersion, the dominant process in the far-field, and is in agreement with a linear propagation model that is independent of the wake Re and Fr. This agreement suggests that, within the Re range considered, the most energetic waves impacting the surface originate from the early-time wake that is adjusting to buoyancy. Questions remain about the efficiency of late-time buoyancy driven stratified turbulence in radiating waves with considerable energy content. The most energetic wavelength $\hat{\lambda}_H$, when normalized by D, is found to scale as $Fr^{1/3}$ and decrease with Re, which causes the arrival time (in Nt units) of the strongest waves at the surface to scale as $Fr^{-1/3}$ and increase with Re. This wavelength $\hat{\lambda}_H$ is also found to correlate with the vertical integral scale, ℓ_V, of the wake turbulence. IW-driven phenomena at the surface that are of interest to an observer, such as the local enrichment of surfactant and the transport of ocean surface tracers, are also discussed. The local enrichment ratio of surfactant scales linearly with the steepness of IWs that reach the surface and often exceeds a possible visibility threshold. The nonlinear Lagrangian drifts

of ocean tracers create a local divergence in lateral mass transport right above the wake centreline, an effect that intensifies strongly with increasing Fr.

The final portion of the dissertation focuses on massively-parallel, implicit large-eddy simulations of stratified towed-sphere wakes at $Re = 4 \times 10^5$, a previously unattained Reynolds number of such flow. The analyses focus on the vortical structures within the wake, evolution of mean flow, turbulent length scales and turbulent viscosities. The key finding is that, the wake Reynolds number Re has a significant impact on the evolution of the dynamically critical buoyancy Reynolds number, $\mathcal{R}$, i.e., as Re increases, the $\mathcal{R}$ at a given dimensionless time Nt is higher, and thus the transition from the inviscid regime at $\mathcal{R} > 1$ to the viscous regime at $\mathcal{R} < 1$ is delayed to a higher value of Nt. As $\mathcal{R}$ is found to be linked to the local Richardson number $\mathcal{R} \sim Ri_{loc}^{-1}$, the delay of $\mathcal{R}$ dropping below $O(1)$ implies a delay of Ri_{loc} reaching beyond $O(1)$, the latter being the requirement for the buoyancy-driven shear layers to restabilize. The prolongation of shear instabilities due to higher $\mathcal{R}$ in a higher-Re wake during the NEQ regime is confirmed through visual observations of the vortical structures and estimates of horizontally averaged Ri_{loc}. During both the inviscid and viscous regimes, the theoretical scalings of the vertical integral scale seem to hold. In order to improve upon an existing self-similarity model of the mean wake evolution, turbulent viscosities in both horizontal and vertical directions are estimated from the LES data set. The results question the validity of the constant turbulent viscosity in the horizontal direction and zero turbulent viscosity in the vertical (after $Nt = 2$) that were assumed in the self-similarity model. When parameterized by the buoyancy Reynolds number $\mathcal{R}$, the vertical turbulent viscosity, albeit insignificant after $Nt \approx 10$ in the average sense, seems to be comparable to the prediction by a canonical diapycnal diffusivity model for a range of $\mathcal{R}$ values.

BIOGRAPHICAL SKETCH

Qi Zhou is originally from Nanjing, China, where he was brought up. He went to college in Singapore and graduated with a B.Eng. degree (with First Class Honors) in Environmental Engineering from Nanyang Technological University in December 2008. He was named the Lee Kuan Yew Gold Medalist for Environmental Engineering in 2009. He then studied at Stanford University under a fellowship and earned an M.S. degree in Civil and Environmental Engineering (CEE) with an emphasis on Environmental Fluid Mechanics and Hydrology (EFMH) in June 2010. Since then he has been a Ph.D. student in the School of CEE at Cornell University pursuing further study in the EFMH area. In particular, he has been interested in studying the physics of stratified fluids via computational fluid dynamics (CFD) tools. Upon receiving his Ph.D. degree, Qi is going to join the Department of Applied Mathematics and Theoretical Physics (DAMTP) at the University of Cambridge as a postdoc to continue his research on stratified turbulence.

To My Family with Love

ACKNOWLEDGEMENTS

This year marks a whole decade since I left my home country to pursue higher education overseas. During this journey, I have been through two countries and three universities, many joys and pains. With all the experiences finally culminating in this Ph.D. dissertation, I am most indebted to my parents, Madam Jiying Chen and Professor Yuxing Zhou, who have always believed in me and the not-so-easy career path that I have chosen. I am most thankful for the independent character they cultured in me since my childhood, and the curiosity towards the unknowns. This dissertation would not have been possible without the tireless guidance and encouragement from Professor Peter Diamessis, my dearest advisor. Pete has been extremely humble and humorous, giving me the most freedom possible and encouraging independent thinking. Not only instrumental in my research, Pete has been a fantastic role model as a devoted and enthusiastic teacher and lovable human being with true passion in life. Professor William Philpot has been the most patient listener of my research on remote sensing of the sea surface and provided many insights during our chats in summer 2013. Professor Stephen Pope has helped me gain a much deeper grasp on turbulent flows via his extraordinarily organized class; he is also thanked for examining this entire thesis meticulously and providing many insights, especially on §7. I thank Professors Diamessis, Philpot and Pope for serving on my Special Committee. Professors Todd Cowen, James Jenkins and Phillip Liu are also thanked for being invaluable members of the EFMH family.

My study has benefited tremendously through collaborations with researchers outside Cornell. I am thankful to Professor Triantaphyllos Akylas (MIT) for guidance on weakly nonlinear internal wave beam theory. Professor Oliver Fringer (Stanford) is thanked for sharing insights on interpreting free surface displacement due to internal wave. I thank Dr. Louis Gostiaux (Ecole Centrale de Lyon) and Professor

Nicolas Grisouard (U. Toronto) for many constructive comments on the manuscript on internal-wave-dirven Lagrangian transport. Professor Geoffrey Spedding (USC) is most gratefully thanked for proving many deep insights on stratified turbulent wakes and very sharply pointing out a bug in my adaptation of his wavelet analysis code. Dr. Scott Wunsch (Johns Hopkins) is thanked for sharing insights on experimental studies on internal wave beams. Professors James Riley (U. Washington) and Stephen de Bruyn Kops (U. Massachusetts) are our collaborators through a High Performance Computing Modernization Program (HPCMP) Frontier projec titled *Multiscale Interactions in Stratified Turbulence*. They kindly helped to secure the supercomputing resources which enabled the simulation of the very high Re flows, and shared many physical insights. Dr. Patrice Meunier (IRPHE, Marseille) helped interpret the rationale of the self-similar model of mean wake evolution.

I would like to thank the following people for instrumental guidance in my early scientific career prior to Cornell: Professors Nian-Sheng Cheng (my undergraduate thesis advisor and my first-ever coauthor), Siow Yong Lim, Yee Meng Chiew and Soon Keat Tan at Nanyang Technological University, and Professors Jefferey Koseff (my M.S. advisor) and Stephen Monismith at Stanford University. Dr. Erin Hult is thanked for a fantastic early summer in 2010 exploring waves and turbulence in a laboratory stratified flume. Looking forward, I thank Professor Paul Linden and Drs. Colm Caulfield, John Taylor and Stuart Dalziel at the University of Cambridge for offering me a postdoc position in the research team probing into the *Mathematical Underpinnings of Stratified Turbulence*.

My colleagues in the EFMH group are cordially thanked for their company and camaraderie (listed in chronological order of initial acquaintance): Ammar Abidilganie, Jorge Escobar, Blair Johnson, Jose Gonzalez, Seth Schweitzer, Allie King, Rafael Tinoco, P. J. Russelo, Yong Sung Park, Erika Johnson, Nimish Pujara,

Patricio Winckler (and his lovely family), Mahmoud Sadek, Ravi Mohandie, Chao An, Sumedh Joshi, Peter Lo, Tak Sakai, Che-Wei Chang, Diego Muriel, Anil Aksu, Gustavo Rivera, Ignacio Sepulveda, Jiajun Gu and Veronica Citerone. I also thank the Cornell undergraduate students in ENGRD 3200 *Engineering Computation* who I taught as a TA in springs 2014 and 2015. I thank them for making my first teaching experience an enjoyable and highly rewarding one, and for nominating me for the *John Perry TA Prize* in 2014. The support from the staff members of the CEE department is also very gratefully acknowledged.

I am grateful for the financial and technical support I have received. Support through Office of Naval Research grants N00014-08-1-0235 and N00014-13-1-0665 administered by Dr. Ronald Joslin, and through the DeFrees Fellowship at Cornell CEE, is very gratefully acknowledged. Supercomputing resources were made available through the HPCMP allocations on clusters Chugach, Copper, Garnet and Pershing. I especially thank the technical support on supercomputing at the HPC Help Desk, who answered hundreds of emails from me over the years, provided timely services, and taught me so much know-how in performing HPC.

The material presented in §4 is a reprint of an article in *Phys. Fluids* (Zhou and Diamessis, 2013); materials in §5 and §6 are currently under consideration for publication in *Phys. Fluids* and *J. Fluid Mech.* respectively (Zhou and Diamessis, 2015a,b). §7 is part of a manuscript in preparation.

TABLE OF CONTENTS

LIST OF TABLES

LIST OF FIGURES

CHAPTER 1

INTRODUCTION

1.1 Internal waves and stratified turbulence

The ocean and atmosphere on the Earth are often stably stratified, with the density of the fluid increasing with depth (in the ocean) or decreasing with height (in the atmosphere) (Turner, 1973). Stably stratified media support internal wave (IW) motions (Lighthill, 1978; Sutherland, 2010) and can modify the dynamics the turbulent flows (Riley and Lelong, 2000; Riley and Lindborg, 2012). Internal waves are effective energy and momentum carriers in the ocean interior (Thorpe, 1975), and their breaking often leads to turbulence and mixing, which introduces bottom nutrients to the upper ocean and modifies the local biology. Stratified turbulence is the main driver of the mixing of nutrient and heat in the ocean (Ivey *et al.*, 2008), and at the same time, the loalized turbulent flow in the ocean interior can emit internal waves to the ambient (e.g., Abdilghanie and Diamessis (2013)) and possibly create impact in the far-field. In this dissertation, we report research efforts, mainly driven by numerical simulations, that are devoted to investigate the physics of IWs and stratified turbulent flows in several prototypical settings.

The subsequent sections of this chapter provide a broad picture of the way in which the various topics examined in this dissertation have developed: §1.2 introduces the nonlinear dynamics within internal wave beams, a typical form of oceanic internal waves originated from high-mode internal tide or constituent element of turbulence-emitted IWs; §1.3 reviews stratified turbulence and highlights the difference between stratified turbulence that is homogeneous in space and its spatially localized counterpart, which is prototyped by a tow-sphere wake in this disserta-

tion; §1.4 focuses on the internal waves emitted by stratified turbulence, and §1.5 discusses the mechanisms through which internal waves may create their signatures on the sea surface and possibly reveal information about these submerged flow to a remote observer.

1.2 Nonlinear effects in reflecting internal wave beams

1.2.1 Eulerian aspects

Internal wave (IW) beams are a frequently occurring type of wave motion in the stratified ocean (Lien and Gregg, 2001; Cole *et al.*, 2009; Johnston *et al.*, 2011). The natural generation mechanism of IW beams is mainly associated with tidal flow over bottom topography (Garrett and Kunze, 2007; Gostiaux and Dauxois, 2007; Peacock *et al.*, 2008). Moreover, the anthropogenic origins of these beams in natural environment are often linked to submerged turbulent flows and their interactions with the stratified medium (Keeler *et al.*, 2005; Marmorino *et al.*, 2010); for example, an isolated component of the quasi-random IW field emitted by a turbulent wake (Abdilghanie, 2010; Abdilghanie and Diamessis, 2013), may be approximated to leading order as a wave beam.

In the idealized setting of the laboratory, IW beams generated by an oscillating cylinder in a uniformly stratified fluid form the well-known St Andrew's cross pattern (Mowbray and Rarity, 1967). Instead of emanating four beams simultaneously, a new experimental apparatus has been developed by Gostiaux *et al.* (2007) to generate one single unidirectional beam, as desired by laboratory study of an isolated IW beam, e.g., on their interactions with the oceanic pycnocline (Mercier *et al.*, 2012). In the numerical setting, IW beams have been generated from bot-

tom topography (Echeverri *et al.*, 2009) or by appropriately designed forcing terms (Javam *et al.*, 2000).

This dissertation investigates the reflection of a finite-amplitude IW beam off a flat horizontal free-slip surface, an idealization of the ocean's free surface. This canonical problem can essentially be viewed as the nonlinear interaction between the incident and reflected beams in the vicinity of the reflecting boundary. In the existing literature, both linear (Thomas and Stevenson, 1972) and finite-amplitude (Tabaei and Akylas, 2003) aspects of IW beams have been addressed theoretically. One key observation on the nonlinearity of IW beams (Tabaei and Akylas, 2003) indicates that nonlinear effects play a relatively insignificant role when a weakly-nonlinear beam propagates freely in a uniformly stratified Boussinesq fluid, the stratification profile in which most of the present study is performed. However, nonlinear effects do become important when multiple IW beams are present to interact, as evidenced in experiments (Teoh *et al.*, 1997), numerical simulations (Javam *et al.*, 2000) and perturbation analysis (Tabaei *et al.*, 2005). These nonlinear effects can produce a mean flow (Tabaei *et al.*, 2005) and higher harmonics (Teoh *et al.*, 1997; Javam *et al.*, 2000; Tabaei *et al.*, 2005). We thus seek to explore the nonlinear effects that are likely to occur due to wave-wave interaction in our specific flow setting, i.e., a nonlinear IW beam reflecting at a free-slip surface.

From an ocean engineering point of view, an improved understanding of nonlinear IW reflection off sea surface may provide insights that facilitate the remote sensing of underwater wave motion or wave-generating turbulence activities by tracking the surface signature of a nonlinear reflection event. Existing literature on tracking internal wave activities remotely are largely limited to internal solitary-like waves traveling through a pycnocline (Robinson, 2010; Klemas, 2012), whereas

a few isolated observational studies report the surface signature of IWs originating from submerged turbulence (Keeler *et al.*, 2005; Marmorino *et al.*, 2010). This dissertation aims to provide insights on finite-amplitude IW beam reflection, such as the parametric dependence of (sub)surface mean flow structure and magnitude and associated harmonics, that may be of use to the above-indicated objectives of remote sensing efforts. On one hand, a persistent mean flow in the (near)-surface reflection region may bias the spatial distribution of surface tracer fields in the reflection region. On the other, the generation of harmonics is a phenomenon of both oceanographic and fundamental physical interest (Jiang and Marcus, 2009).

The linear inviscid reflection of IW from a sea surface has been considered by LeBlond and Mysak (1978). By assuming that the surface displacement is small, they showed that upon the reflection off a horizontal surface at which the vertical velocity vanishes, an IW preserves its horizontal wavenumber, reverses the sign of the vertical wavenumber, and undergoes a phase shift of π. Analysis by Kistovich and Chashechkin (1995) on a reflecting linear beam suggested that the reflected beam can be described by nothing more than a beam produced by the mirror image of the original beam source on the reflecting surface, with the viscous and diffusive effects appropriately accounted for.

In this dissertation, we assume that the surface displacement is small, and that the top surface examined is of the free-slip type as a modeling effort to describe the sea surface. The literature on nonlinear reflection in such a set-up is very limited. Within a flow setting very similar to the present study, Lamb (2004) performed numerical simulations on the reflection of topographically generated nonlinear tidal IW beams from a sea surface (being modeled as a free-slip rigid lid). He reported mean-flow and harmonic generation, and suggested that the nonlinear wave-wave

interactions behind these phenomena are non-resonant in nature, and that they are second-order and local in significance. Questions remain on how these nonlinear effects observed by Lamb (2004) vary with the IW beam properties (in particular, its degree of nonlinearity), which calls for a more systematic study.

On the contrary, a number of studies (Thorpe, 1987; Slinn and Riley, 1998; Javam *et al.*, 1999; Zikanov and Slinn, 2001; Dauxois *et al.*, 2004; Peacock and Tabaei, 2005; Gostiaux *et al.*, 2006; Rodenborn *et al.*, 2011) have addressed the reflection of IW off a a sloping solid no-slip boundary, as a model of oceanic bottom topography. This problem is complicated by its geometry, i.e., the existence of critical reflection (Slinn and Riley, 1998; Dauxois *et al.*, 2004) and obliquely incident waves (Zikanov and Slinn, 2001), boundary layer development associated with the no-slip condition (Slinn and Riley, 1998; Dauxois *et al.*, 2004), the turbulent dynamics within the boundary layer (Slinn and Riley, 1998), and wave breaking (Javam *et al.*, 1999). In terms of nonlinear wave-wave interactions in the case of no-slip surface reflection, Peacock and Tabaei (2005), Gostiaux *et al.* (2006) and Rodenborn *et al.* (2011) all reported laboratory observations of harmonic generation during IW reflection, which verify the prediction by Tabaei *et al.* (2005). However, it remains unclear whether these observations can be extrapolated to the free-slip case. In other words, it is not clear how the wave-generated mean-flow structure, which eventually forms a boundary layer in the no-slip-surface-reflection problem, will develop at a free-slip surface in the absence of a boundary layer, an open question that further motivates the present study.

1.2.2 Lagrangian aspects

In this dissertation, we also aim to extend the study on internal wave beam reflection from the Eulerian to the Lagrangian perspective with the motivation explained below. First, net Lagrangian effects such as mean drifts and particle dispersion due to IW beam reflection have a direct impact on the transport of passive scalars and micro-organisms in the ocean upper layer. However, knowledge of the Eulerian mean of a wavy flow alone is often found to be insufficient for inferring material transport when wave-induced effects, such as Stokes drift, are significant, e.g., in the context of interpreting field data containing both surface waves and mean currents (Monismith and Fong, 2004). This gives rise to a need to further clarify the nonlinear reflection process from the Lagrangian perspective. Moreover, the understanding of reflecting-IW-induced Lagrangian motions of ocean surface tracers may facilitate the interpretation of remote sensing images containing possible signatures of IW beams and eventually the identification of submerged IW sources (Keeler *et al.*, 2005; Marmorino *et al.*, 2010).

Lagrangian studies of IWs have been reported in the literature targeting wave configurations other than reflecting IW beams: Stokes drift induced by vertically localized IW packets can be derived from the Stokes theorem (Sutherland, 2010). Shear-flow dispersion due to vertically unbounded IWs has been examined by numerical particle tracking (Steinbuck *et al.*, 2011). Lagrangian flows within vertical-mode IWs and internal solitary waves have been investigated by G. Gil and O. B. Fringer (pers. comm.). Particle dispersion due to dissipative effects in a random IW field has also been investigated (Bühler *et al.*, 2013).

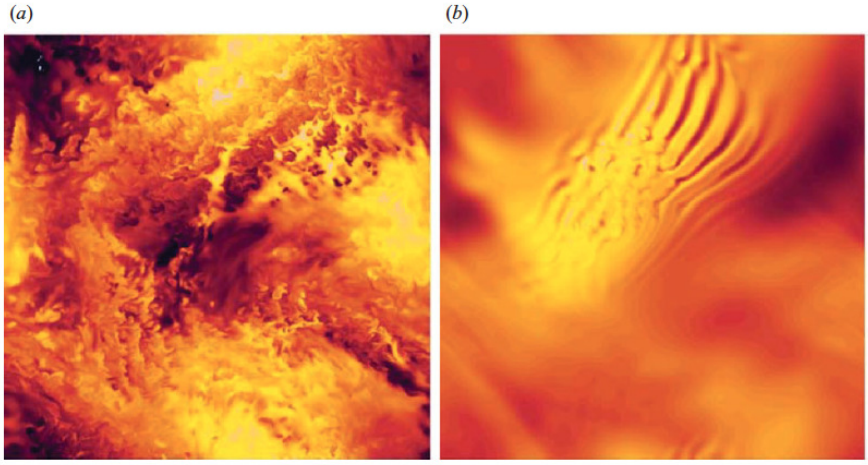

Figure 1.1: A horizontal cut of the density fluctuation field in homogeneous stratified turbulence (Fig. 7 of Brethouwer *et al.* (2007)): (a) $\mathcal{R} = 9.6$, (b) $\mathcal{R} = 0.40$. This figure is reproduced from *J. Fluid Mech.*, 585, pp. 343-368, Copyright 2013, Cambridge University Press.

1.3 Dynamics of stratified turbulence

1.3.1 Homogeneous stratified turbulence

Although the proposed study concerns an *inhomogeneous* turbulent flow in a stably stratified medium, i.e., the wake behind a towed sphere, we start by reviewing recent progress in the dynamics of *homogeneous* stratified turbulence, e.g., as recently reviewed by Riley and Lindborg (2012) (hereinafter referred to as R&L). These studies, often performed via direct numerical simulation (DNS) at considerably high Reynolds numbers, provide many insights to the present study.

Basic phenomenology

Based on DNS of homogeneous stratified turbulent flows spanning a considerable parameter range, Brethouwer *et al.* (2007) (hereinafter referred to as BBLC) classi-

fied these flows into two regimes: the strongly stratified turbulence regime ($\mathcal{R} > 1$) and the viscosity-affected stratified flow regime ($\mathcal{R} < 1$) based on the buoyancy Reynolds number

$$\mathcal{R} \equiv \frac{\varepsilon}{\nu N^2},$$

where ε is the turbulent kinetic energy dissipation rate, ν is the kinematic viscosity, and the buoyancy frequency

$$N \equiv \sqrt{-\frac{g}{\rho_0}\frac{d\bar{\rho}}{dz}}$$

characterizes the inverse time scale of buoyancy effects.

Regardless of the magnitudes of $\mathcal{R}$ and various designs of forcing in the simulations, BBLC and other authors (Riley and de Bruyn Kops, 2003; Waite and Bartello, 2004; Lindborg, 2006) share the notion that the flow *spontaneously* organizes into quasi-horizontal layers that induce strong vertical shear acting between them. On the other hand, as shown in Fig. 1.1, the flow structure is sensitive to $\mathcal{R}$: When $\mathcal{R} > 1$, the structure is abundant in small scales presumably produced by Kelvin-Helmoltz instabilities due to shear between the thin horizontal layers and is turbulent-like on a horizontal plane; when $\mathcal{R} < 1$, the disturbances are localized and wave-like. Billant and Chomaz (2000) proposed that zigzag instability is responsible for the layering. The subsequent pathway to the above-mentioned turbulence structure has been the subject of extensive studies (Augier and Billant, 2011; Augier *et al.*, 2012; Waite, 2013).

Energy spectra and cascade

Early studies of turbulence in stratification were motivated by the observed $k_h^{-5/3}$ power-law behavior of the mesoscale energy spectra in the often stably stratified atmosphere, where k_h is the horizontal wave number. Lilly (1983), who invented the

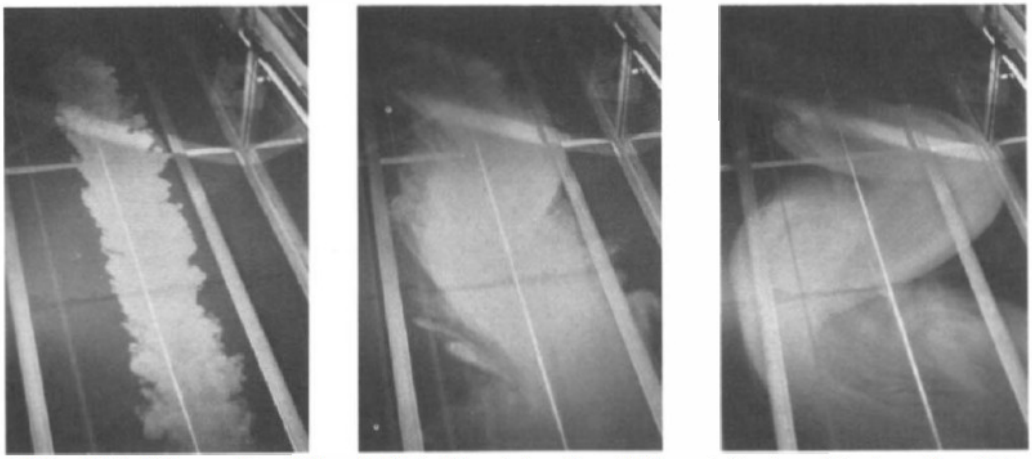

Figure 1.2: Dye visualization of the evolution of the stratified wake of a towed *slender* body by Lin and Pao (1979) (Fig. 9). Lilly (1983) included these pictures and commented in the caption: "the initially small-scale three-dimensional turbulence is transformed into a horizontally meandering flow", implying the existence of an inverse cascade. Note that the dimensionless time Nt in the figures are given in buoyancy periods (one period is 2π in radians) rather than in radians (as used elsewhere in this dissertation). This figure is reproduced from *Ann. Rev. Fluid Mech.*, 11, pp. 317-338, Copyright 1979, Annual Reviews.

term "stratified turbulence" and was inspired by the "wake collapse" phenomenon reported by Lin and Pao (1979) (see Fig. 1.2), conjectured that an *inverse* energy cascade is responsible for the $k_h^{-5/3}$ spectrum and developed scaling arguments supported by a two-dimensional theory of stratified turbulence. He so described the flow: "The long-lived residue of a three-dimensional turbulence event is a distributed flow which behaves like two-dimensional turbulence in conserving its energy and transporting it to *increasingly larger* scales, although it maintains its structure." While believing that the inverse cascade is predominant, Lilly did not exclude the seemingly opposite scenario that "part of the energy of the stratified turbulence is recycled into three-dimensional turbulence by shearing instabilities".

Riley and de Bruyn Kops (2003), however, observed the $k_h^{-5/3}$ spectrum along with a *forward* cascade in their DNS of evolution of Taylor-Green vortices under stable stratification at considerably high Reynolds numbers. They also reported shear instabilities between the flow layers, which had been correctly envisioned by Lilly (1983). Subsequent DNS studies (Waite and Bartello, 2004; Lindborg, 2006) also lent support to a forward cascade, suggesting the existence of inertia-range dynamics in stratified turbulence. The subtle effect of $\mathcal{R}$ on the horizontal spectra was recently treated by Bartello and Tobias (2013), suggesting sensitivity of the spectra to $\mathcal{R}$ when $\mathcal{R}$ is not greater than $O(10)$.

Scales

By considering the governing equations of stratified turbulence, i.e., the Navier-Stokes equations under the Boussinesq approximation, BBLC performed scaling analysis of such flows at both limits of $\mathcal{R}$, i.e., $\mathcal{R} \gg 1$ and $\mathcal{R} \ll 1$. The focal point of their analysis is the treatment of the vertical (integral) length scale ℓ_v, which is different in the two limits. In the viscously affected $\mathcal{R} \ll 1$ regime (Godoy-Diana *et al.*, 2004), ℓ_v is determined by the balance between viscosity and horizontal advection like a laminar boundary layer (see e.g., (Kundu and Cohen, 2008)), and hence

$$\ell_v \sim \ell_h R^{-1/2},$$

where ℓ_h is horizontal integral length scale and

$$R \equiv \ell_h U_h / \nu$$

is an integral-scale Reynolds number, where U_h is a characteristic velocity at scale ℓ_h. In the geophysically more relevant (see Fig. 1.3) strongly stratified turbulence

regime ($\mathcal{R} \gg 1$) Billant and Chomaz (2001), the flow aspect ratio $\alpha \equiv \ell_v/\ell_h$ scales with an integral-scale horizontal Froude number

$$F_h \equiv U_h/(\ell_h N),$$

so that

$$\ell_v \sim U_h/N.$$

Such a scaling of ℓ_v results in a dimensionless horizontal momentum equation at $\mathcal{R} \gg 1$ which resembles the unstratified turbulence counterpart (see BBLC, §2), but with the conventionally defined Reynolds number, i.e., R, replaced by the buoyancy Reynolds number

$$\mathcal{R} = \frac{\varepsilon}{\nu N^2} \approx \frac{U_h^3/\ell_h}{\nu N^2} = \frac{\ell_h U_h}{\nu}(\frac{U_h}{\ell_h N})^2 = RF_h^2. \tag{1.1}$$

BBLC then deduced from (1.1) Hebert and de Bruyn Kops (2006) that, for a given fluid medium with fixed ν and N, $\mathcal{R}$ depends solely on ε, a quantity not associated with a particular length scale or velocity scale, i.e., the Taylor estimate $\varepsilon \sim \mathcal{U}^3/\mathcal{L}$ holds for any length scale $\mathcal{L}$ and the velocity scale $\mathcal{U}$ associated with it. In other words, $\mathcal{R}$ acts as the characteristic Reynolds number for all scales of motion. This argument leads to BBLC's claim that "... *the influence of viscosity is equally important at all scales of stratified turbulence.* This is in contrast to Kolmogorov turbulence where the influence of viscosity decreased with increasing scale". The notion of a universal effect of $\mathcal{R}$ on a wide range of scales is important to note for scalings which are going to be developed in the proposed study.

One of the fundamental length scales in stratified turbulence is the Ozmidov scale

$$\ell_O = (\frac{\varepsilon}{N^3})^{1/2},$$

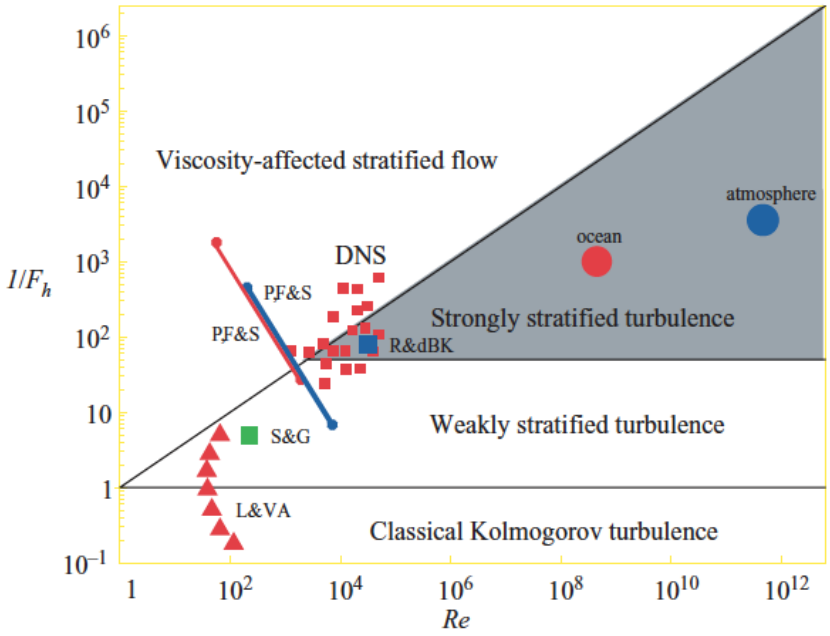

Figure 1.3: Regimes of stratified flow on parameter space $1/F_h$ vs. R (Brethouwer *et al.* (2007), Fig. 18). Red squares denote DNS of BBLC and blue square denotes Riley and de Bruyn Kops (2003). This figure is reproduced from *J. Fluid Mech.*, 585, pp. 343-368, Copyright 2013, Cambridge University Press.

which is used to characterize the largest horizontal scale which has enough kinetic energy to overturn and signifies a transitional scale between stratified turbulence (Riley and Lindborg, 2012) and classical Kolmogorov turbulence (Tennekes and Lumley, 1972; Pope, 2000). The range of length scales in stratified turbulence is determined by the Froude number F_h (Brethouwer *et al.*, 2007; Riley and Lindborg, 2012),

$$\frac{\ell_h}{\ell_O} \sim F_h^{-3/2}, \frac{\ell_v}{\ell_O} \sim F_h^{-1/2}.$$

Moreover, the separation between the buoyancy-affected ℓ_O and the Kolmogorov scale $\eta = (\nu^3/\varepsilon)^{1/4}$ scales with $\mathcal{R}$ (Brethouwer *et al.*, 2007; Riley and Lindborg, 2012):

$$\frac{\ell_O}{\eta} \sim \mathcal{R}^{4/3}.$$

1.3.2 Stratified turbulent wakes

3D-NEQ-Q2D phenomenology

The stratified turbulent wake is a canonical *inhomogeneous* stratified turbulent shear flow with important geophysical (oceanic wakes of islands and seamounts, atmospheric wakes of mountains) and ocean engineering applications. The wake of a towed sphere can be characterized by the body-based Reynolds number

$$Re \equiv \frac{UD}{\nu},$$

and Froude number

$$Fr \equiv \frac{2U}{ND},$$

where D is the diameter of the sphere and U is the horizontal towing speed.

Early studies of wakes of a self-propelled slender body were reviewed by (Lin and Pao, 1979), who reported the "wake collapse" phenomenon (Fig. 1.2). Spedding and coworkers, via a series of papers (Spedding *et al.*, 1996a,b; Spedding, 1997, 2001, 2002), examined towed-sphere wake in a salt-stratified water tank. Their experiments covered a wide range of Fr from 10 to 240, but a relatively limited Re range from 5×10^3 to 1.1×10^4.

Spedding (1997) identified a universal (under the Re range he examined) curve of the evolution of mean centerline axial velocity of the wake U_0 with time in buoyancy units Nt. He divided the wake evolution into three regimes (see Fig. 1.4):

1. An early-time three-dimensional turbulent regime (*3D*);

2. A subsequent non-equilibrium regime (*NEQ*) featuring a reduced decay rate of U_0, growing control of buoyancy as turbulence decays and strong internal wave emission from the wake; and

3. A final quasi-horizontal regime (*Q2D*) where buoyancy has fully taken control and the flow has organized into large quasi-two-dimensional vortices with only weak coupling in the vertical due to a complex network of vortex lines (Spedding *et al.*, 1996a).

At a given Nt, U_0/U is proportional to $Fr^{-2/3}$ and independent of Re.

Meunier *et al.* (2006) (hereinafter referred to as MDS) subsequently proposed a semi-empirical self-similar model for the evolution of mean axial velocities and length scales of stratified momentum wakes, in an attempt to match laboratory and numerical data available at that time (Gourlay *et al.*, 2001; Dommermuth *et al.*, 2002; Diamessis *et al.*, 2005). A key assumption of the MDS model is that the vertical turbulent momentum flux is completely suppressed by buoyancy after $Nt = 2$, i.e., at the 3D-NEQ transition and onwards; in this dissertation, we aim to refine this model by properly incorporating vertical transport of momentum in the subsequent NEQ regime.

Numerical studies

Gourlay *et al.* (2001) performed DNS of a stratified momentum wake at $Re = 10^4$ and $Fr = 10$. They examined both statistical quantities and vortex structures. One key result was that the formation of quasi-horizontal vortices in the far wake is unrelated to any coherent structures there might be in the near wake, such as vortices shedded from the wake-generating body. Dommermuth *et al.* (2002)

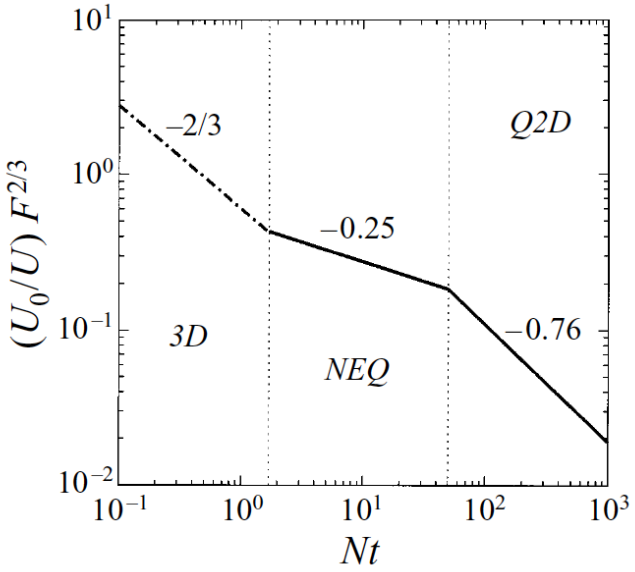

Figure 1.4: Spedding's $Fr^{-2/3}$-scaling of mean centerline axial velocity U_0 (normalized by towing speed U) of stratified towed-sphere wake in the 3D-NEQ-Q2D regimes (Spedding (1997), Fig. 7) valid for a maximum Re of 1.1×10^4 and any Fr. This figure is reproduced from *J. Fluid Mech.*, 337, pp. 283-301, Copyright 1997, Cambridge University Press.

performed large eddy simulation (LES) up to $Re = 10^5$ and presented a carefully designed wake initiation procedure. A recent DNS of momentum wake reached $Re = 5 \times 10^4$ (de Stadler and Sarkar, 2012). Self-propelled momentumless wakes were also studied and compared to towed momentum wakes (Brucker and Sarkar, 2010).

Diamessis *et al.* (2011) (hereinafter referred to as DSD) performed LES of towed-sphere wakes at $Re \in [5 \times 10^3, 10^5]$ and $Fr \in [4, 16, 64]$. The 3D-NEQ-Q2D regimes were recovered from these simulations. At the higher Re they examined, however, DSD observed a prolongation of NEQ regime to $Nt \approx 100$, questioning the universality of the NEQ-Q2D transition point in (Spedding, 1997) (Fig. 1.4) which was based on relatively low Re's. DSD also observed secondary Kelvin-

Helmholtz instabilities between the flow layers, providing the first evidence for the prediction (Lilly, 1983) for *localized* and *inhomogeneous* turbulence. Non-negligible vertical motions and turbulent transport were observed during NEQ, motivating a major reconsideration of the MDS self-similar model (Meunier *et al.*, 2006).

1.4 Internal waves emitted by stratified turbulence

Submerged localized stably stratified turbulent flows in the ocean emit internal waves (IWs) which carry momentum, energy and information away from the source for long distances. Possible turbulent sources of IWs may include the bottom boundary layer (Taylor and Sarkar, 2007), municipal outfalls (Keeler *et al.*, 2005) and submerged wakes (Pal *et al.*, 2010; de Stadler and Sarkar, 2012; Abdilghanie and Diamessis, 2013). A canonical flow for the study of internal-wave-emitting localized turbulence is the stratified wake of a towed sphere, which itself is a fundamental reference flow for geophysical and naval applications (Lin and Pao, 1979; Spedding, 2014). Pioneering and recent experimental studies (Gilreath and Brandt, 1985; Hopfinger *et al.*, 1991; Bonneton *et al.*, 1993; Meunier, 2012) at Re up to 3×10^4 and $0.5 \leq Fr \leq 12.7$ revealed two types of internal waves generated by stratified wakes, i.e., the lee waves behind the sphere (or cylinder) which dominates at $Fr < 4$ and the quasi-random waves emitted by the turbulence in the wake dominating at $Fr \geq 4$, the latter wave type being the focus of the present study. Spedding *et al.* (2000) towed spheres at Re up to 1.2×10^4 and $Fr \in \{4, 64\}$ and reported carefully sampled internal wave properties. They also made the first attempt to correlate the observed wave characteristics with the wake's governing parameter, e.g., a $Fr^{1/3}$ scaling for the observed wavelengths was reported.

Abdilghanie and Diamessis (2013) performed numerical simulations at $Re \in \{5 \times 10^3, 10^5\}$ and $Fr \in \{4, 16, 64\}$ (the case $(Re, Fr) = (10^5, 64)$ was missing due to limited computing resources), which provided insights on wake-emitted waves at higher Re than previously achieved in laboratory. At the higher Re examined, they reported that the wave emission is prolonged and persists up to $Nt \approx 100$ (as compared to $Nt \approx 50$ at the lower Re), which was attributed to the prolongation of the wave-emitting non-equilibrium (NEQ) (Spedding, 1997) regime of the wake that is driven by secondary Kelvin-Helmholtz instabilities (Riley and de Bruyn Kops, 2003; Diamessis *et al.*, 2011). The wave emission was found to be less affected by viscosity as Re increases, as evidenced by a noticeable shift in the dominant wave frequency from the one which minimizes viscous decay of wave amplitude (at lower Re) (Taylor and Sarkar, 2007) to the one which maximizes momentum extraction from the wake (at higher Re), as well as a significant increase in the momentum flux carried away by the waves (Sutherland and Linden, 1998). Continuous wavelet transforms (Dallard and Spedding, 1993; Spedding *et al.*, 1993; Abdilghanie, 2010) were employed to interrogate the waves' length scales and periods, on account of the localized and intermittent nature of the turbulence-emitted random waves. In agreement with Spedding *et al.* (2000), an empirical $Fr^{1/3}$ scaling, which was motivated by the same Fr-scaling of the horizontal eddy dimensions (Spedding *et al.*, 1996a), was able to collapse the time series of wavelengths sampled at different vertical offsets not far (up to $3.4D$ away) from the wake centreline. The wavelengths were observed to decay with time following a power law $(Nt)^{-C}$, where C is generally smaller than unity and varies with Fr and Re in the near-field of the wake. The very fact that the wave characteristics vary with Nt, which alternatively can be converted to the dimensionless downstream distance from the sphere

$$\frac{X}{D} = \frac{Fr}{2} Nt, \tag{1.2}$$

implies the possibility of inferring the stage of evolution (or "age") of the wave-emitting submerged localized stratified turbulence, or the distance X from the origin of the flow, based on far-field measurements of the turbulence-emitted internal waves. Such an inference would require a detailed knowledge of wave characteristics within the parameter space (Re, Fr, Nt), not only in the near-field of the wake, but also in the far-field. One also needs to take into account the various physical processes which the waves may have been subject to along their propagation path before their characteristics are revealed to interested observers, such as the dispersion of these waves and their interactions with background stratification and/or currents (Thorpe, 1975, 2005; Sutherland, 2010).

1.5 Sea-surface manifestation of submerged stratified flows

1.5.1 Submerged turbulent events in stratified waters

Submerged sources of momentum in the ocean located sufficiently close to the surface, e.g., a municipal outfall, can generate a visible surface signature (surface 'boils") due to vertical turbulent entrainment (Marmorino *et al.*, 2010). When stratification is strong and the vertical growth of the source-driven turbulence suppressed, the above mechanism is less likely to work. Alternatively, a more likely detection mechanism for submerged stratified turbulence (wakes in particular) is believed to rely on the large-scale quasi-horizontal vortex structures (also known as "pancake" vortices formed during the NEQ regime) within the flows which are highly coherent in space and are very persistent in time. This mechanism was recently discussed by Spedding (2014) who also offered a comprehensive review on the wide range of wake sources, geophysical and biological, in the environment, and

to whom their signatures are important. One way for information on these coherent structures submerged in the ocean to propagate vertically towards the surface is through molecular diffusion (Voropayev *et al.*, 2007, 2009). However, the vertical diffusion of these late-time pancake vortices operates at vertical length scales of $O(\sqrt{\nu t})$ (G. R. Spedding, pers. comm.), which means significant time will elapse before the vortices can noticeably affect the subsurface if the source is located at a considerable depth. On the other hand, internal waves (IWs) are expected to be effective carriers of energy and information through the water column in the oceanic environment (Thorpe, 2005; Sutherland, 2010). In the present study, the possibility of a submerged stratified turbulent flow establishing a distinct surface signature through the radiation of IWs is investigated for the first time.

1.5.2 Horizontally and vertically propagating internal waves

The manifestation of IWs at the ocean surface has been extensively studied in the context of packets of internal solitary waves (ISWs) (Robinson, 2010; Klemas, 2012). These high amplitude (40 to 50 m) and $O(1$ km) long waves propagate horizontally as interfacial depressions in a two-layer stratification and have a distinct vertical (modal) structure set by the finite depth of the water column. The near-surface ISW horizontal velocity field consists of zones of convergence and divergence, aft and fore, respectively, of the wave trough. The free surface is thus strained and the convergent/divergent pattern in the surface velocity field propagates in phase with the ISW (Moum and Smyth, 2006). Numerous field studies, relying on synthetic aperture radar (SAR) (Alpers, 1985) and, more recently, infrared imaging (Marmorino *et al.*, 2004) and lidar (Magalhaes *et al.*, 2013), have

identified such surface velocity patterns above trains of ISWs. Similar organized surface signatures are generated by the body-driven periodic long interfacial IWs behind sea mounts (Cresswell *et al.*, 1996) and ships (Watson *et al.*, 1992) in straights and fjords supporting a two-layer stratification.

These convergent/divergent patterns in the surface velocity field due to underlying IWs may manifest themselves through multiple surface modulation mechanisms (Klemas, 2012), such as 1) *hydrodynamic modulation* through the action of surface wind-generated capillary-gravity waves (Alpers, 1985; Hwung *et al.*, 2009), 2) *surface film modulation* by forming the "slicks" of oceanic surfactant consisting of organic rich materials (Ewing, 1950b; Ermakov *et al.*, 1992) under low-wind conditions, and 3) *thermal modulation* through the thickness change of the "cool-skin" temperature sublayer (Osborne, 1964, 1965; Zappa and Jessup, 2005). Key to these processes is the *horizontal divergence*

$$\Delta_z \equiv \frac{\partial u}{\partial x} + \frac{\partial v}{\partial y} \tag{1.3}$$

of sea surface flows. Δ_z is the sum of normal strain rates on a horizontal plane and is the hydrodynamic quantity ideal for visualization and analysis of wake-emitted IWs used by various authors (Spedding *et al.*, 2000; Abdilghanie and Diamessis, 2013; Spedding, 2014) and in the present study.

The surface signature of IW beams/packets of tidal origin or radiated by deeply submerged turbulent sources propagating obliquely in a continuously a stratification has not been investigated in the field as extensively as its interfacial wave counterpart, i.e., horizontally propagating ISWs. Pingree and New (1995) reported surface signatures of internal tides on images in the visible band from the Bay of Biscay. Alternative detection mechanism may involve the enrichment of near-surface chlorophyll on tidal wave crests (da Silva *et al.*, 2002). Recent observa-

tional efforts using either satellite images (Keeler *et al.*, 2005) or airborne-sampled infrared imaging (Zappa and Jessup, 2005; Farrar *et al.*, 2007) have identified a distinct IW-beam-induced modulation of small-scale capillary gravity waves and straining of the cool skin layer. The present study aims not only to provide a parametric study of the IW characteristics to be expected in the far-field, but also to investigate the mechanisms by which these IWs may self-manifest to remote observers, should the waves propagate upward through the water column and expose themselves at the ocean surface.

The fate of upward-propagating IWs generated in mid-water or from topography may be convoluted by the complex physical processes through variable stratifications (Akylas *et al.*, 2007; Mathur and Peacock, 2009; Grisouard *et al.*, 2011; Mercier *et al.*, 2012; Diamessis *et al.*, 2014; Wunsch *et al.*, 2014), critical layers (Thorpe, 1975; Winters and D'Asaro, 1989), instabilities and breaking in mid-water (Thorpe, 2005), and the ocean subsurface subject to external forcings (Soloviev and Lukas, 2006). Apart from these complications imposed by the background oceanic environment, which are expected to be highly site specific, the nonlinearity within the IWs may also become important as they reflect off the ocean surface. While a single finite-amplitude IW beam does not induce significant nonlinear effects (Tabaei and Akylas, 2003), the IW beam does transfer energy to mean flows and higher harmonics through nonlinear wave-wave interactions upon reflection at the sea surface (Lamb, 2004; Tabaei *et al.*, 2005; Zhou and Diamessis, 2013, 2015a), even when a uniform stratification is present. It remains to be determined whether the turbulence-radiated IWs, which can be considered as the superposition of multiple IW beams/packets (Bonneton *et al.*, 1993; Abdilghanie and Diamessis, 2013), will generate significant nonlinear effects due to reflection and/or wave-wave interference in the ocean subsurface and alter their detectable signatures at the surface.

CHAPTER 2

OBJECTIVES AND OUTLINE

2.1 Reflection of internal wave beams

The first major objective of the dissertation is to study, by means of fully-nonlinear numerical simulations, the nonlinear characteristics of the IW beam reflection off a free-slip flat horizontal surface, from both the Eulerian and Lagrangian perspectives. The former is presented in §4, the content of which is summarized below. The model formulation is presented in details in §4.1, where the basic scaling and parameter space are introduced and the numerical model is described. Our main focus of the study is on the mean flow generated due to nonlinear wave-wave interaction below a free-slip rigid surface, the subsurface structure of the mean flow, and the scaling of its strength with the wave beam characteristics (see §4.2). These results will be presented and compared quantitatively to the inviscid weakly nonlinear theory by Tabaei *et al.* (2005) in §4.3. Other nonlinear features, such as harmonic generation (see §4.3) and late-time instability of the reflecting wave (see §4.4), will also be discussed. A subsurface mixed layer (see §4.5) will be added to the basic problem set-up. Further discussions will follow in §4.6.

We also examine the Lagrangian aspects of reflecting IWs off a free-slip surface (§5) aiming at the following specific questions: Does a reflecting finite-amplitude IW beam induce net Lagrangian effects, i.e., mean drifts and dispersion? If so, how do these effects scale with IW beam parameters? Both small-amplitude analysis (§5.1) and fully-nonlinear numerical particle tracking (§5.2) in the DNS dataset obtained in §4 will be utilized to address these questions. In §5.3, further discussion of the results will be provided.

2.2 Characterization of turbulence-emitted internal waves

The present state of understanding of the internal waves emitted by stratified turbulent sources, specifically those prototyped by the wake of a towed sphere, are much limited to the wave characteristics near the generation site, i.e., in the *near-field* of the turbulent wave source (Bonneton *et al.*, 1993; Spedding *et al.*, 2000; Abdilghanie and Diamessis, 2013), where the dynamics is expected to be highly nonlinear. The primary objective of this study is to provide a quantitative description of the *far-field* evolution of the internal waves emitted by a submerged localized stratified turbulent source that complements the recent near-field characterization reported by Abdilghanie and Diamessis (2013) (hereinafter referred to as A&D), with an emphasis on characterizing the sea-surface manifestation of these waves. This study is to replicate the parameter range in terms of the wave-emitting wake's Reynolds number Re and Froude number Fr covered by A&D, as well as to extend it to the more computationally expensive case $(Re, Fr) = (10^5, 64)$. The computational domains are made larger than those of A&D's, in order to capture the wave characteristics in the wake's far-field.

Simulations of turbulent wakes and wave-generated internal waves are performed within a uniform stratification bounded from above by a model free-slip sea surface. We are interested in characterizing the internal wave signatures at the sea surface, in particular, a statistical description of the wave energy distribution over various wavelengths and wave periods, and how this distribution changes over space (with respect to the centreline of the wake flow) and over time (elapsed since the passage of the sphere), at a wide range of wake parameters (Re, Fr). We also aim to identify the key physical process behind the observations: Is linear theory sufficient to describe the kinematics of these waves in the far-field? Does the reflec-

tion of the waves at the surface induce significant nonlinear effects which distinctly impact the surface observation of these waves? With the remote sensing application in mind, we are also interested in correlating the surface observations to the dynamic state of turbulence, characterized by Nt, and how the wake turbulence chooses the preferred waves to emit into the ambient. Moreover, a first discussion of the mechanisms by which obliquely propagating IWs can create remote sensing signatures after reaching the sea surface will also be provided. In this dissertation, we focus on a simple set-up with a uniform stratification and zero background flow, and defer the effects of variation (of stratification and/or mean flow) in the background and external forcings on these waves, to future study.

Chapter 6 of this dissertation studies the internal wave signatures and is outlined here: In §6.1, the numerical model and problem set-up will be introduced; in §6.2, the basic flow phenomenology will be described; in §6.3, far-field wave statistics, including amplitude, wavelength, period and orientation, which are sampled at the sea surface, will be reported, and a linear dispersive propagation model, for the wavelength evolution in time at the surface, will be developed; in §6.4, two potential signature-generating mechanisms will be discussed, one relying on modulation of surface scalar field and the other concerning collective motions of Lagrangian tracers; further discussion on the results is presented in §6.5.

2.3 Localized stratified turbulence at high Re

For unstratified canonical self-similar free-shear flows (Tennekes and Lumley, 1972; Pope, 2000), the mean flows can often be characterized by a turbulent Reynolds number $Re_T \equiv U_0\delta/\nu_T$, where U_0 is a mean flow velocity scale, δ is the dimension

of the flow, and ν_T the turbulent viscosity. Re_T is the Reynolds number that is defined based on mean flow quantities and is often found to be independent of the flow's bulk Reynolds number Re in canonical unstratified free-shear flows (Tennekes and Lumley, 1972; Pope, 2000). In this dissertation, we aim to seek the *Reynolds number effects* on various flow quantities of a stratified wake. This is based on both the claim of universality of viscous effects on all length scales by Brethouwer *et al.* (2007) and the Re-dependence of mean wake quantities observed by Diamessis *et al.* (2011), where Re is the body-based wake Reynolds number. The ultimate goal is to be able to reliably extrapolate the results at Re's achievable in numerical studies to the geophysical relevant Re's (Fig. 1.3). The specific questions are:

- How does Re affect the vortical structures within the stratified wake, i.e., the pancake vortices in the horizontal and the buoyancy-driven shear layer in the vertical? How does Re affect the potential of buoyancy-driven Kelvin-Helmholtz instability that are present in the NEQ regime of the wake?
- How the mean flow quantities, such as U_0 and wake width/height at a given Nt, vary with Re?
- How do the turbulent momentum fluxes (Reynolds stresses) in both horizontal and vertical directions, possibly modelled by the corresponding turbulent viscosities, vary with Re?
- How does the buoyancy Reynolds number $\mathcal{R}$ scale with wake Re and Fr and evolve with Nt? How does it affect the scaling of the turbulent length scales within the flow?

A systematic characterization of the Reynolds number effects in stratified wakes, based on a series of numerical simulations at $Re \in \{5 \times 10^3, 10^5, 4 \times 10^5\}$ and $Fr \in \{4, 16, 64\}$, is presented in §7.

CHAPTER 3

NUMERICAL METHODS

3.1 Governing equations and boundary conditions

The governing equations for the various stratified flow problems considered in this dissertation are the incompressible Navier-Stokes equations and the density equation under the Boussinesq approximation:

$$\frac{\partial \mathbf{u}}{\partial t} + \mathbf{u} \cdot \nabla \mathbf{u} = -\frac{1}{\rho_0} \nabla p + \mathbf{F}_g + \nu \nabla^2 \mathbf{u} + \mathbf{F}_\mathbf{u} + \mathbf{S}_\mathbf{u}, \tag{3.1}$$

$$\frac{\partial \rho}{\partial t} + \mathbf{u} \cdot \nabla (\rho + \bar{\rho}(z)) = \kappa \nabla^2 \rho + F_\rho + S_\rho,$$

$$\nabla \cdot \mathbf{u} = 0,$$

where the gravity force acts only in the vertical:

$$\mathbf{F}_g = -g \frac{\rho}{\rho_0} \hat{\mathbf{k}},$$

where g is the gravitational acceleration and $\hat{\mathbf{k}}$ is the unit vector in the vertical direction. Note that ρ and p denote respectively the perturbation density and pressure from the hydrostatic state; $\mathbf{F}_\mathbf{u} = (F_u, F_w)$ and F_ρ are mechanical wave forcing terms that are only applicable for the internal wave beam problem considered in §4. The specific forms of the wave forcing terms $\mathbf{F}_\mathbf{u}$ and F_ρ are shown in §4.1. $\mathbf{S}_\mathbf{u}$ and S_ρ are Rayleigh-type wave sponge layer terms similar to those used by Abdilghanie (2010); the details of sponge layer implementation for the turbulent wake simulations can be found in Appendix C. The boundary conditions that are applied for each flow set-up are to be discussed in the respective chapters. Numerical simulations of these flows are performed using the spectral multidomain penalty scheme developed by Diamessis *et al.* (2005) (hereinafter referred to as "DDH"). The temporal and spatial discretization of this flow solver is reviewed here.

3.2 Temporal discretization scheme

A high-accuracy pressure projection scheme (Karniadakis *et al.*, 1991) is employed for the temporal discretization of time-dependent governing equations (3.1). Taking velocity $\mathbf{u}$ as an example, the time advancement from time step n to $n+1$ is achieved in three fractional steps:

$$\frac{\hat{\mathbf{u}} - \sum_{q=0}^{J_i-1} \alpha_q \mathbf{u}^{n-q}}{\Delta t} = \sum_{q=0}^{J_e-1} \beta_q \mathbf{N}(\mathbf{u}^{n-q}) \quad , \tag{3.2}$$

$$\frac{\hat{\hat{\mathbf{u}}} - \hat{\mathbf{u}}}{\Delta t} = -\nabla \phi^{n+1} \quad , \tag{3.3}$$

$$\frac{\gamma_0 \mathbf{u}^{n+1} - \hat{\hat{\mathbf{u}}}}{\Delta t} = \nu \mathbf{L}(\mathbf{u}^{n+1}) \quad , \tag{3.4}$$

where the nonlinear operator $\mathbf{N}$ includes the advective, gravity, body force and sponge layer terms, and linear operator $\mathbf{L}$ corresponds to the viscous term. The splitting procedure for ρ' consists of two steps analogous to (3.2) and (3.4). In (3.2)-(3.4), a 3rd order backward differentiation scheme (BDF3 with $J_i = 3$) is used to discretize the temporal derivative. The viscous operator $\mathbf{L}$ is treated fully implicitly. The nonlinear terms $\mathbf{N}$ are advanced in time via a third order stiffly stable scheme (SS3 with $J_e = 3$) allowing for a maximum value of a stable timestep. The values of the coefficients α_q, β_q and γ_0 for a BDF3-SS3 scheme may be found in Karniadakis *et al.* (1991). The quantity ϕ^{n+1}, which satisfies

$$\int_{t_n}^{t_{n+1}} \nabla p' dt = \Delta t \nabla \phi^{n+1} \quad , \tag{3.5}$$

is an intermediate scalar field that ensures that the final velocity $\mathbf{u}^{n+1}$ is incompressible. In (3.3), it is assumed $\nabla \cdot \hat{\hat{u}} = 0$, and the Poisson equation

$$\nabla^2 \phi^{n+1} = \nabla \cdot \left(\frac{\hat{\mathbf{u}}}{\Delta t} \right) \tag{3.6}$$

is solved for the pressure. The timestep size is adjusted dynamically subject to the constraints imposed by maximum CFL number (DDH) and by the proper functioning of the sponge layer (Abdilghanie, 2010). Further details on the order of accuracy associated with the above splitting scheme can be found in DDH.

3.3 Spatial discretization scheme

In both horizontal directions x and y, Fourier spectral discretization is used with N_x and N_y Fourier modes respectively, in accordance with the periodic boundary conditions. Horizontal derivatives are calculated in a straightforward fashion in Fourier spectral space. In the vertical direction, the computational domain is partitioned into M subdomains of variable height H_k ($k = 1,\ ...\ M$) and order of polynomial approximation $\hat{N}$. Within each subdomain, a Legendre spectral collocation scheme (Boyd, 2001) is used; the total number of vertical grid points is $N_z = M(\hat{N}+1)+1$. A patching condition (DDH) is applied to enable subdomains to communicate with their neighbors above and below. The choice of spatial resolution depends on the specific problem (internal wave vs. turbulence) and will be discussed further in the respective chapters of this dissertation.

3.4 Spectral filtering and penalty techniques

While the spectral discretization employed in the flow solver, to a great extent, overcomes numerical dissipation and dispersion that are common to lower-order schemes, the stability of the numerical scheme is confronted with significant challenges (DDH). When spectral schemes, which are inherently non-dissipative,

are used in under-resolved simulations, the resulting Gibbs oscillations are compounded by aliasing effects driven by the non-linear term, leading to catastrophic numerical instabilities (Gottlieb and Hesthaven, 2001). In order to contain these instabilities, DDH employed both spectral filtering and penalty techniques.

Spectral filtering consists of the explicit application of an order p low-pass filter function to the spectral (modal) expansion of the solution. Application of a pth order spectral filter is the non-stiff equivalent to the use of a pth order hyperviscous operator in the governing equations (Gottlieb and Hesthaven, 2001). Penalty methods consist of collocating a linear combination of the equation and boundary/patching conditions at the boundaries/subdomain interfaces, respectively, which ensures a smooth transition from the subdomain interface to its interior. The detailed implementation of spectral filtering and penalty schemes can be found in DDH and Diamessis *et al.* (2011).

In this dissertation, both internal waves and turbulent flows are simulated, and the nature of these simulations varies depending on whether all relevant scales of motion are resolved. For the internal wave reflection problem considered in §4, spectral filtering does not impact the smallest length scale of the waves, and thus the simulations are regarded as direct numerical simulations (DNS); on the other hand, in the turbulent flow simulations considered in §6 and §7, the cut-off wavenumber of the spectral filter is placed in the inertia subrange of the turbulence, the full spectrum of motion is not resolved, and the simulations are regarded as implicit large-eddy simulations (LES) (Diamessis *et al.*, 2011). In §7, we will further discuss the implementation of spectral filtering in the turbulent wake simulations at $Re = 4 \times 10^5$; the connection of spectral filtering to LES, and the comparison between the implicit LES approach used here and the conventional

approaches relying on an explicit sub-grid scale (SGS) model, can be found in §2.5 of Diamessis *et al.* (2011).

3.5 Particle tracking algorithm

In §5, we report fully nonlinear results of Lagrangian motions obtained by applying numerically particle tracking to the Zhou and Diamessis (2013) (hereinafter referred to as "Z&D") DNS dataset (see the simulation set-up in Fig. 4.1) of Eulerian flow field of reflecting internal waves. Since the net Lagrangian effects being investigated are expected to be nonlinear dynamics of high order (higher than or equal to $O(A^2)$), a reliable particle tracker is imperative for our study. A high-accuracy particle-tracking scheme, which is tailored to the specific Navier-Stokes solver (DDH) used by Z&D, has been developed and implemented in parallel. The time-marching scheme employs a locally fourth-order Adams-Bashforth-Moulton method (Press *et al.*, 2007). A global Fourier-Lagrange interpolation scheme in two dimensions has been developed in order to interpolate the Eulerian velocity field on the Z&D grid to the instantaneous positions of the particles, i.e., (B.2) and (B.3), with spectral accuracy in both spatial directions x and z: For x, a periodic direction in the flow solver, a Fourier interpolation technique (Yeung and Pope, 1988) is used. For z, which is discretized by spectral multi-domains, Lagrange interpolants on the Gauss-Legendre-Lobatto grid are deployed for each individual vertical subdomain. Auxiliary tests have demonstrated that, under this global Fourier-Lagrange interpolation scheme and compared to a third-order cubic spline local one, the interpolation error can be reduced by at least three orders of magnitude at the spatial resolution used by Z&D. This high accuracy strengthens the reliability of the particle tracking results to be presented in §5.

CHAPTER 4

INTERNAL WAVE REFLECTION: EULERIAN DYNAMICS

4.1 Model formulation

4.1.1 Problem geometry

The canonical flow examined in this study is the reflection of a two-dimensional (2-D) IW beam in a uniform stratification. A schematic of the problem is presented in Fig. 4.1. The 2-D computational domain of dimensions $L_x \times L_z$ is stratified in the vertical direction z with a buoyancy frequency N. We focus on the case where the fluid is uniformly stratified, i.e., N is a constant in z, to isolate the effects linked strictly to wave reflection from any additional possible complications introduced by a variable stratification profile (Mathur and Peacock, 2009). Nevertheless, we do provide some preliminary results on cases where we allow the stratification profile to vary (see §4.5).

An IW beam is generated by a virtual source in our numerical model, and the details on the generation will be covered in the next subsection. The beam forms an angle θ with respect to the vertical, which is achieved by prescribing the wavenumber vector $\mathbf{k}_i = (k, -m)$ according to the dispersion relation

$$\omega_0 = N \cos\theta = N \sqrt{\frac{k^2}{k^2 + m^2}},$$

where ω_0 is the forcing frequency. The angle θ is referred to as the *phase-tilt* angle as it describes the direction of the iso-phase lines with respect to the vertical. Wave energy is transported upwards along the direction of the iso-phase lines, which is also the direction of a fluid particle's oscillation, until the incident beam

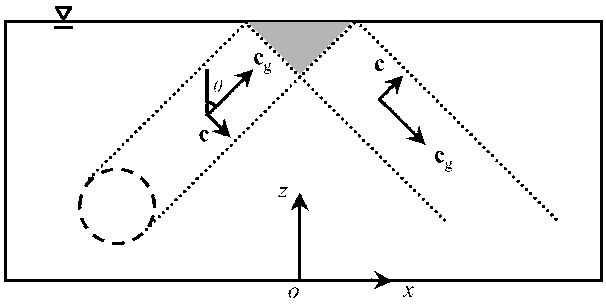

Figure 4.1: Schematic of IW beam reflection in a linear stratification: the dashed circle indicates the location of a virtual wave source, and the dotted lines indicate the spatial extent of the incident and reflected IW beams; wave energy propagates in the direction of group velocity $\mathbf{c}_g$, which has an angle θ with respect to the vertical direction z, and the iso-phase lines propagates in the direction of phase velocity $\mathbf{c}$. The shaded area indicates where the incident and reflected beams intersect and interact. The boundaries of this zone are shown here for illustration purpose only; a more accurate delineation of the reflection/interaction zone can be found in Fig. 4.3.

reaches the reflecting surface at $z = L_z$. A reflected beam with $\mathbf{k}_r = (k, m)$ forms upon reflection (LeBlond and Mysak, 1978), which continues to propagate with the same angle θ with respect to the vertical, but propagates downward instead. The major task of the study is to investigate the nonlinear dynamics in the subsurface reflection zone, where the incident and the reflected beam intersects, an area highlighted in Fig. 4.1. The planar beam in this from is a first-order approximation of the IW field which might originate from 2-D oceanic bottom topography.

The computational domain has periodic lateral boundaries, a no-slip bottom boundary, and a free-slip top boundary. The validity of such a top boundary condition as a representation of the ocean surface will be discussed in §8.1. A sponge layer, the thickness of which is summarized for each simulation in Table 4.2, operates on the bottom and lateral boundaries. The sponge layer prevents

any unwanted wave reflections from the bottom boundary and the re-entry of IWs from the lateral periodic boundary which would contaminate the field under examination.

4.1.2 Wave forcing and boundary conditions

The specific wave forcing terms in the governing equations (3.1) are formulated as follows:

$$F_u = \frac{U_f}{T_f}(-F\frac{m}{k}\cos\phi - \frac{\partial F}{\partial z}\frac{1}{k}\sin\phi + \frac{\partial F}{\partial x}\frac{m}{k^2}\sin\phi), \tag{4.1}$$

$$F_w = \frac{U_f}{T_f}F\cos\phi, \tag{4.2}$$

$$F_\rho = -|\frac{d\bar{\rho}}{dz}|\frac{U_f}{\omega_0 T_f}F\sin\phi,$$

$$\phi = kx + mz - \omega_0 t,$$

where U_f is the reference velocity scale, T_f is the reference time scale (taken as the wave period T), (k, m) is the wavenumber vector, and the two-dimensional localization function (Winters and D'Asaro, 1989; Slinn and Riley, 1998; Abdilghanie, 2010) is

$$F(x, y, z) = \exp[-\frac{(x - x_{cen})^2}{2\sigma_x^2} - \frac{(z - z_{cen})^2}{2\sigma_z^2}]. \tag{4.3}$$

Boundary conditions that correspond to those discussed earlier are applied in the numerical model. Homogeneous Dirichlet boundary conditions for ρ are applied at both top and bottom boundaries.

4.1.3 Scaling and dimensionless parameters

We now consider the non-dimensional form of the governing equations. The purpose is only to illustrate the basic scaling of the problem and introduce the dimensionless parameters to the discussion. We introduce the following scaling, similar to Javam *et al.* (2000), to the IW problem,

$$x \sim \lambda_x,\ z \sim \lambda_x,\ t \sim N^{-1},\ u \sim U_0,\ w \sim U_0,$$

$$\rho \sim |\frac{d\bar{\rho}}{dz}|U_0 N \sim \frac{\rho_0 N^3 U_0}{g},\ p \sim \rho_0 \lambda_x U_0 N,$$

where U_0 is the characteristic particle velocity. Non-dimensionalizing the vertical component of (3.1) yields

$$\frac{\partial w^+}{\partial t^+} + \frac{U_0}{N\lambda_x}\mathbf{u}^+ \cdot \nabla w^+ = -\frac{\partial p^+}{\partial z^+} - \rho^+ + \frac{1}{\lambda_x^2 N/\nu}\nabla^2 w^+,$$

where the superscript $^+$ indicates dimensionless quantities. Two dimensionless quantities appear in the above equation: $U_0/N\lambda_x$ which measures the nonlinearity of the system, and $1/\lambda_x^2 N/\nu$ which measures the strength of viscous effects. Note that both of these quantities are assumed to be zero in linear inviscid theory (LeBlond and Mysak, 1978). We further discuss the associated implications below.

The nonlinearity parameter

In the literature, various choices of a parameter quantifying the degree of nonlinearity in internal wave field have been proposed: e.g., Sutherland (2001) uses the wave steepness

$$A = A_\xi/\lambda_x, \tag{4.4}$$

which is the ratio between the maximum vertical isopycnal displacement A_ξ and the horizontal wavelength λ_x. A_ξ can be estimated based on small-amplitude theory

(Sutherland, 2010) as

$$A_\xi = \frac{kU_0}{m\omega} = \frac{U_0}{N\sin\theta},$$

where the definition of U_0 is refined here to be the maximum horizontal velocity of a fluid particle in a freely-propagating wave. Thus the steepness A can be expressed as

$$A = \frac{U_0}{N\lambda_x}\frac{1}{\sin\theta}. \tag{4.5}$$

One can observe from (4.5) that A combines the nonlinearity parameter, $U_0/N\lambda_x$, obtained from nondimensionalizing (3.1), and the degree of hydrostaticity as represented by the phase-tilt angle θ. A more relevant form of the wave amplitude parameter for scaling the nonlinear effects within the reflecting waves, is found to be $A\tan\theta$. From (4.5),

$$A\tan\theta = \frac{U_0}{N\lambda_x}\frac{1}{\cos\theta} = \frac{U_0}{\omega\lambda_x} = \frac{1}{2\pi}\frac{U_0}{c_x}, \tag{4.6}$$

i.e., when multiplied by 2π, $A\tan\theta$ measures the magnitude of the maximum horizontal particle velocity U_0 relative to the horizontal phase speed c_x, a direct interpretation of this useful parameter.

An alternative definition of the nonlinear parameter A, the excursion parameter A_k used by Mercier *et al.* (2012) compares the particle displacement in the beam direction to the wavelength; Javam *et al.* (2000) used the Keulegan number Ke which directly originates from non-dimensionalizing the governing equations but with a mechanical forcing/acceleration scale F (with a dimension of L/T^2) to normalize the wave amplitude, instead of using velocity scale U_0. Finally, the Dauxois-Young (Dauxois *et al.*, 1999) amplitude parameter A_{DY}, based on magnitude of streamfunction, relates to the wave steepness A, by

$$A_{DY} = \frac{2\pi}{\tan\theta}A.$$

In the present study we will base our discussion of the nonlinear effects on the wave steepness A, as a descriptor of degree of nonlinearity.

The Reynolds number

A wave-celerity-based Reynolds number Re_w emerges directly from the above scaling of (3.1),

$$Re_w \equiv \frac{\lambda_x^2 N}{\nu} = \frac{\lambda_x \frac{2\pi}{k} \frac{\omega_0}{\cos\theta}}{\nu} = \frac{c_x \lambda_x}{\nu} \frac{2\pi}{\cos\theta},$$

where $c_x = \omega_0/k$ is the horizontal celerity. Note that this wave amplitude-independent Re_w describes the significance of the viscous decay of the beam along its propagation path. Lighthill (1978) derived a exponential viscous damping factor for the amplitude of internal waves generated by an oscillatory source, which could be re-written in our nomenclature as

$$A/A_0 = \exp(-\frac{1}{Re_w} \frac{8\pi^3}{\sin\theta \cos^3\theta} \frac{\eta}{\lambda_x}), \tag{4.7}$$

where A is the wave steepness at a distance η away from the source along the beam path, and A_0 is the steepness at the source. It can be inferred from the damping factor that, among beams with the same geometric characteristics (θ and λ_x), an IW beam with smaller Re_w tends to be damped faster, an observation that is valuable for our subsequent discussions.

On the other hand, a particle-velocity-based Reynolds number Re_p can also be defined, in a more conceptually straightforward way, by taking the ratio of the nonlinear and viscous parameters,

$$Re_p \equiv \frac{U_0}{N\lambda_x} \frac{\lambda_x^2 N}{\nu} = \frac{U_0 \lambda_x}{\nu},$$

which describes the relative significance of viscous effects as compared to the nonlinear inertial force. It is to be shown later that, the nonlinear effects observed due

Table 4.1: Parameter values of numerical simulations of internal wave beam reflections. T01-05 are the baseline runs; T06-10 examine the effect of σ_x/λ_x; T11-15, 16-18 examine the effect of θ; and T19 examines the effect of the Reynolds number. The actual envelope half-widths σ_{sfc} measured at the surface are $[0.861, 1.608, 0.936, 0.776, 0.860]\lambda_x$ for T01-05, T06-10, T11-15, T16-18 and T19 respectively.

Run No.	θ	σ_x/λ_x	Re_w	Re_p	A (%)	Run No.	θ	σ_x/λ_x	Re_w	Re_p	A (%)
01	45°	0.538	29,900	681	3.23	11	63°	0.538	299,000	13,700	5.14
02	45°	0.538	29,900	528	2.50	12	63°	0.538	299,000	7,080	2.65
03	45°	0.538	29,900	120	0.569	13	63°	0.538	299,000	3,400	1.27
04	45°	0.538	29,900	29	0.139	14	63°	0.538	299,000	750	0.281
05	45°	0.538	29,900	7	0.0344	15	63°	0.538	299,000	182	0.0681
06	45°	1.076	74,700	3,370	6.38	16	27°	0.538	29,900	322	2.41
07	45°	1.076	74,700	2,550	4.83	17	27°	0.538	29,900	74	0.554
08	45°	1.076	74,700	544	1.03	18	27°	0.538	29,900	18	0.136
09	45°	1.076	74,700	130	0.246	19	45°	0.538	299,000	1,610	0.763
10	45°	1.076	74,700	32	0.0609						

to IW reflection (at least in terms of mean-flow generation), are independent of Re_p. A general discussion on the role that viscosity plays in the IW beam reflection problem will then follow.

4.1.4 Summary of numerical simulations

The numerical simulations examined in this study are summarized in Table 4.1. Each simulation is referred to as Tp hereinafter, where p is the Run No. in Table 4.1. Through a total of 19 simulations, we aim to cover the full parameter space as presented below:

Phase-tilt angle θ: θ measures the direction of wave propagation, as well as its hydrostaticity (Sutherland, 2010).

Spatial compactness σ_x/λ_x: σ_x and σ_z dictates the half-width (or height) of the wave source in x and z (see (4.3)). Therefore, σ_x/λ_x and σ_z/λ_z describe the spatial compactness of the IW beam. For all simulation, $\sigma_x/\lambda_x = \sigma_z/\lambda_z$.

The actual compactness of the beam in the reflection zone, however, may differ from the one specified as σ_x/λ_x for the forcing envelope. By applying a least-squares fit of a Gaussian to the amplitude envelope function measured at the reflecting surface (see Fig. 4.4 for an illustrated example), we can determine the actual surface compactness of a reflecting beam, characterized by the envelope half-width σ_{sfc}, the values of which are included in the caption of Table 4.2.

Note that θ and σ_x/λ_x together describe the *geometry* of the problem. In this regard, the simulations can be grouped into four *geometric configurations*, each corresponding to runs with the same combination of θ and σ_x/λ_x:

1. T01-05 and T19: $\theta = 45°$ and $\sigma_x/\lambda_x \simeq 0.538$, the *baseline* geometry;
2. T06-10: $\theta = 45°$ but $\sigma_x/\lambda_x \simeq 1.076$ (doubled from baseline by halving λ_x and keeping σ_x the same);
3. T11-15: $\theta = 63°$ and $\sigma_x/\lambda_x \simeq 0.538$;
4. T16-18: $\theta = 27°$ and $\sigma_x/\lambda_x \simeq 0.538$.

Further detail of each of these geometric configurations, i.e., domain dimensions, location of wave source, and thickness of sponge layer, is shown in Table 4.2.

Table 4.2: Domain dimensions $L_x \times L_z$, number of grid points $N_x \times N_z$, center position of wave source (x_{cen}, z_{cen}), and thickness of sponge layer δ_t, for the internal wave beam reflection simulations. All lengths are normalized by the horizontal wavelength λ_x in each simulation respectively. See Fig. 4.1 for a sketch of the coordinate system, i.e., $x = 0$ at the intersection of the centerline of the beam and the reflecting surface, $z = 0$ at the bottom of the domain, and $z = L_z$ at the top reflecting surface. See Abdilghanie (2010) for details on sponge layer.

Run No.	$L_x \times L_z$	$N_x \times N_z$	(x_{cen}, z_{cen})	δ_t
01-05,19	16×7	512×300	$(-5, 2)$	1
06-10	32×14	768×372	$(-10, 4)$	2
11-15	16×4.5	512×275	$(-5, 2)$	1
16-18	11×7	384×300	$(-2.5, 2)$	1

Reynolds number Re_w: As discussed above, Re_w describes the relative strength of viscous effects. Re_w has been carefully adjusted (by reducing the viscosity ν) as such, so that for certain geometric configurations more prone to viscous decay (based on the exponential damping factor proposed by Lighthill (1978)), i.e., T06-10 and T11-15, the beam still sustain a high enough amplitude to generate significant nonlinear effects in the subsurface reflection region.

Wave steepness A: This is a key parameter that describes the degree of nonlinearity of the IW. For each of the geometric configurations, we ran a series simulations with a number of A values. The details on how A is determined for each simulation are to be discussed in §4.2.2.

A number of additional simulations have also been run where a subsurface mixed layer is introduced into the stratification profile. These simulations are not

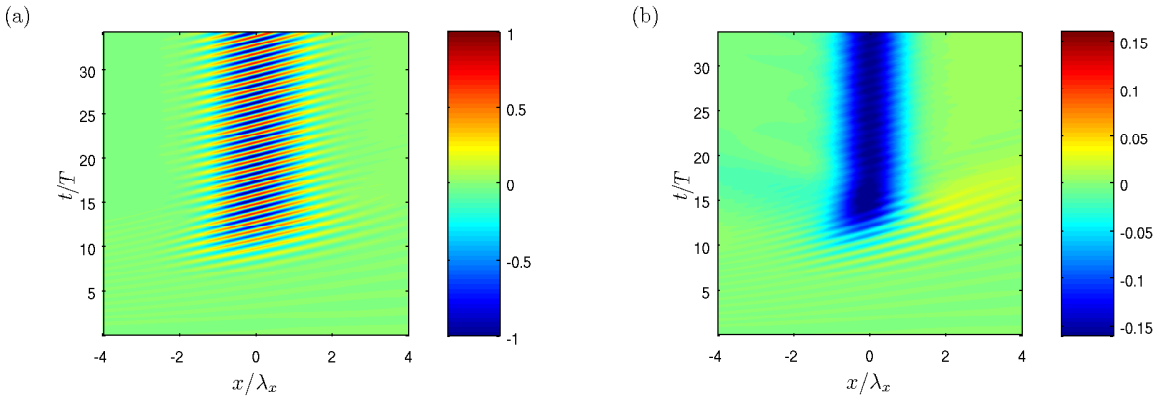

Figure 4.2: xt-contours of (a) instantaneous surface velocity u and (b) mean surface velocity $\langle u \rangle$, both normalized by the observed maximum surface velocity magnitude U_{max}. Data shown are for T01.

included in Table 4.1, but will be discussed later separately. The Prandtl number $Pr = \nu/\kappa$ is fixed at unity throughout the study.

The typical resolution in horizontal direction is 32 points per λ_x. The vertical subdomains are more clustered towards the top boundary, where the flow of interest occurs, and around the wave source. Vertical subdomain thickness ranges from $0.4\lambda_z$ for the top subdomain to $0.8\lambda_z$ in the free-propagating portion of the wave beam. The number of Gauss-Legendre-Lobatto points in each subdomain is between 25 or 31. The total number of grid points used in each simulation configuration is tabulated in Table 4.2.

4.2 Reflection-induced mean flow

4.2.1 Surface response

The evolution of the u velocity at the free-slip surface is presented as an xt-plot in Fig. 4.2 for a baseline case T1. Similar patterns are observed for all simulations

in Table 4.1. Mean quantities of interest, denoted by $\langle\ .\ \rangle$, are computed through a temporal average over one wave period $T = 2\pi/\omega_0$. For example, the mean of a variable f, is computed as

$$\langle f \rangle(\mathbf{x}, t) = \frac{1}{T} \int_{t-T/2}^{t+T/2} f(\mathbf{x}, t')dt'.$$

Note that the analysis approach based on spatially averaging over a moving window of width λ_x in the x-direction, aimed towards identifying a volume-averaged wave-induced mean flow (Abdilghanie and Diamessis, 2012), turns out to be inappropriate for the present study. Such an analysis is ineffective in representing the inherent spatial variability of the mean-flow generation under the current configuration. This spatial variability, as evidenced by the example in Fig. 4.2(b), is the topic of extensive discussion in subsequent sections of this dissertation. Finally, also note that the temporal moving average technique is used solely for the purpose of examining the spatial structure of mean currents; temporal spectral analysis similar to Mercier *et al.* (2008) will be used here to quantify the mean-flow magnitudes.

In the instantaneous u plot shown in Fig. 4.2(a), one can observe that a spatially localized wave pattern occurs after the beam front reaches the surface at around $t/T \simeq 10$. Though not immediately evident in Fig. 4.2(a), in a average sense, the negative velocities in a wave cycle are stronger than the positive ones, as visible in the $\langle u \rangle$ plot in Fig. 4.2(b). A mean flow, with a maximum strength of about 16% of the maximum velocity magnitude U_{max} at the surface, forms at the region where the beam impacts the surface with its magnitude becoming stationary in time after an initial transient and its direction opposite to the horizontal group velocity. The surface response in other simulations appears qualitatively similar to the case shown in Fig. 4.2. However, the strength of the mean flow does vary with wave characteristics such as amplitude A and phase-tilt angle θ, a topic of

primary focus which will be discussed in detail later.

4.2.2 Subsurface vertical mean shear

Mean flow forms not only at the surface but also over the full extent of the reflection zone in the subsurface, where the incident and reflected beams intersect. As with the surface velocity contour plots of Fig. 4.2, the mean flow structure on the xz-planes of Fig. 4.3 represents a steady state that is reached by $Nt \approx 15$. The spatial structure of the temporally moving-averaged $\langle u \rangle$ field is presented in Fig. 4.3 at a time when a steady-state in the reflection region has been attained. The sign of the mean velocity alternates a few times as it extends from the surface down to the bottom of the reflection zone. A layered structure forms in the vertical direction, with a wavelength of approximately half of the vertical wavelength of the incoming IW, an observation that applies for all simulations. It should also be noted that although we present snapshots of the mean structure in Fig. 4.3, the structure shown does stay stationary in time.

For the purpose of delineating the region where the incident and reflected beams intersect and interact, we have drawn a white-dash line in each of the sub-plots in Fig. 4.3. This line corresponds to the contour of temporally averaged local intensity of wave kinetic energy (K.E.) $\rho_0(\langle u^2 \rangle + \langle w^2 \rangle)/2$ at 120% of the corresponding value on the centerline of the incident (reflected) beam outside the reflection zone. This line, along with the surface, approximately encompass the area where the incident and reflected beams intersect, interact and produce mean currents. A hypothetically single, isolated, incident (or reflected) beam has a maximum value of K.E. that occurs at the beam centerline, corresponding to the 100% contour level. When actually both incident and reflected beams are present, as is the case

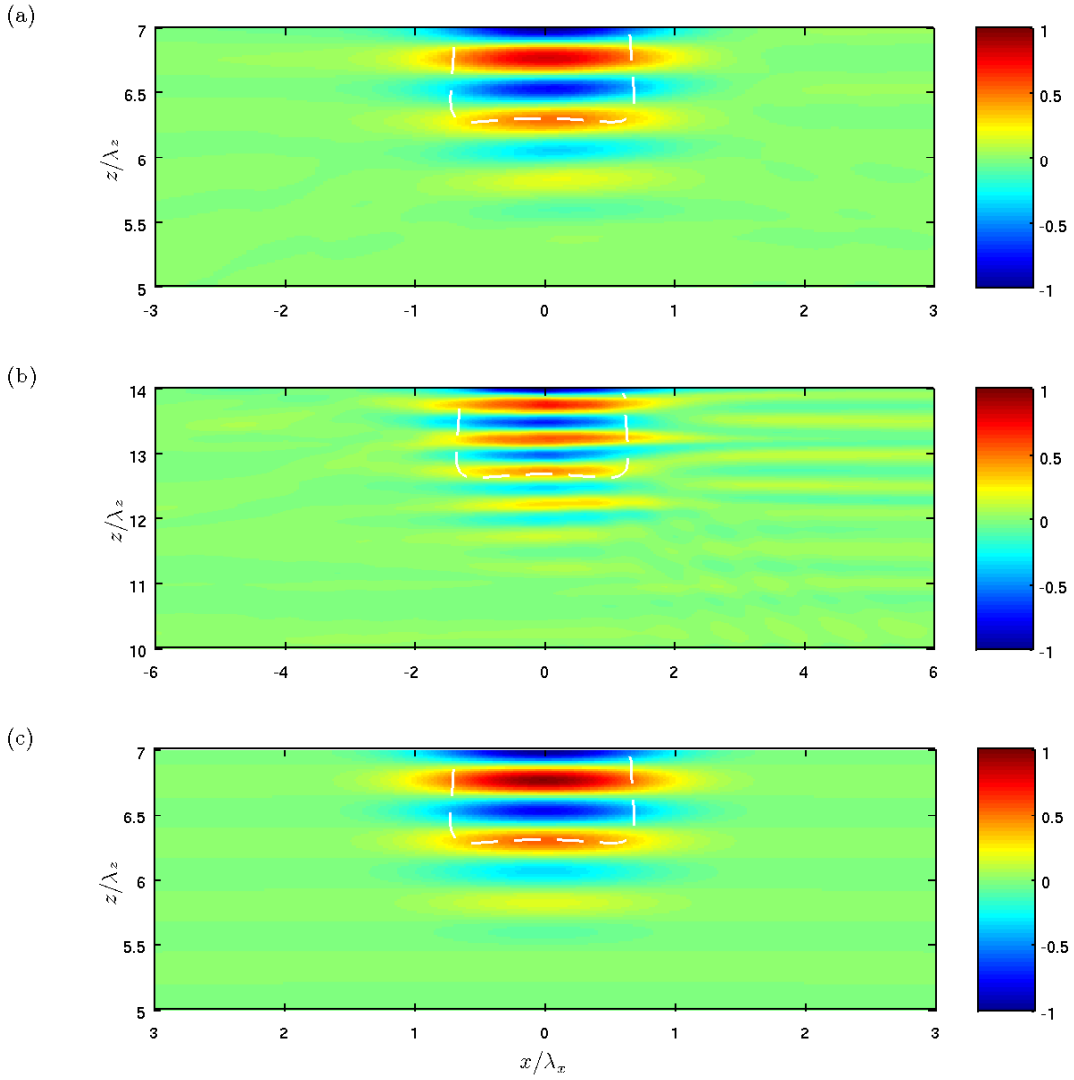

Figure 4.3: xz-contours of mean horizontal velocity $\langle u \rangle$, normalized by its maximum observed magnitude in space, (a) at $t/T = 30$ for T01, and (b) at $t/T = 45$ for T07, in the wave reflection zone. The prediction by inviscid weakly nonlinear theory (Tabaei *et al.*, 2005) for a same wave geometry as T01, is shown in (c) and is to be discussed in §4.3. The reflecting surface is at the top boundary of each contour plot and the centerline of the wave beam intersect with the surface at $x = 0$. The superimposed white dashed line is the contour of temporally averaged local intensity of wave kinetic energy $\rho_0(\langle u^2 \rangle + \langle w^2 \rangle)/2$ at 120% of the corresponding value on the centerline of the incident (reflected) beam outside the reflection zone.

here, any point with a K.E. value below the 100% contour level is clearly outside the intersection/interaction zone; any point with a K.E. value above this limit value resides in the interior of this zone.

As we compare the mean-flow structures of T01 and T07 in Fig. 4.3, the less-compact beam (T07) produces more layers in the subsurface than the more-compact case (T01), which suggests that the formation of these layered structures has to do with the structural details of the incoming IW beam, which will be discussed later in §4.3 when we compare our results to the weakly-nonlinear theory (Tabaei *et al.*, 2005).

The local gradient Richardson number, i.e.,

$$Ri_{loc} \equiv \frac{N^2}{(\partial\langle u\rangle/\partial z)^2},$$

has been computed based on the local mean shear rate $\partial\langle u\rangle/\partial z$, for the baseline cases. The minimum Ri_{loc} is found to be on the order of 150, which suggests that this wave-induced mean shear may not be strong enough to account for any shear instability to the reflecting wave itself.

In case T07, a very weak mean flow structure is visible outside the wave reflection zone, on its downstream side (Fig. 4.3(b)). A number of additional simulations (not examined here) we have performed strongly indicate that these weak mean flows are neither an effect of confinement, i.e., on account of the finite domain length in x, nor a numerical artifact. Examination of the mean streamline structure of the $\langle u, w\rangle$ field (not shown) suggests that these secondary flows may be driven by the stronger circulation in the wave reflection zone, presumably for the purpose of maintaining continuity. We are inconclusive as to why this secondary mean flow is more pronounced in Fig. 4.3(b) than in Fig. 4.3(a) (case T01) and why it occurs only on the downstream side. We defer these questions to future

research efforts. Since the secondary mean flow magnitude is one order of magnitude smaller than that of the primary currents in the wave reflection zone, we do not expect these secondary flows to be of critical importance to the particular dynamics our subsequent analysis focuses on.

Sampling the wave steepness

The major objective of the present study is to explore nonlinear effects, e.g., mean flows, and to quantify their relation to the degree of nonlinearity, as described by the wave steepness A. Note that the amplitude of the beam does undergo viscous damping along the wave path, a process that depends strongly on the geometric configuration, i.e., the *in-situ*[1] amplitude of the reflecting wave is a function of not only its amplitude at the source A_0, but also of η/λ_x, θ and Re_w (see (4.7)). Therefore, to obtain a more representative description of the wave nonlinearity, which is directly responsible for the nonlinear dynamics developing in the reflection zone, we choose to report A at the reflecting surface, as a *local* measure of nonlinearity.

Based on the linear inviscid reflection solution (LeBlond and Mysak, 1978), the horizontal velocity at the surface is double that of either the incident or reflected beam by virtue of the superposition of the two. Moreover, the vertical velocity has to vanish at the surface, since it is a rigid lid, inhibiting any isopycnal displacement and rendering the steepness A, as defined by (4.4), equal to zero at $z = L_z$. Instead, the steepness A we ultimately report at the surface corresponds to the steepness of a freely propagating wave sampled at the location $z = L_z$ which is produced by the same wave forcing and having undergone the same viscous damping though in the

[1]Here and elsewhere "in-situ" is defined as "locally within the reflection region".

absence of the reflecting surface. The values of A used in the following discussions are effectively estimated by (4.5), for which

$$U_0 = U_{max}/2 \tag{4.8}$$

is taken as a half of the maximum horizontal velocity magnitude U_{max} recorded at the surface; the 1/2 factor splits the contributions of the incident and reflected beams into two equal halves, as prescribed by the corresponding linear inviscid solution (LeBlond and Mysak, 1978).

Here we refer to A as the steepness of the reflecting wave only in a *nominal* sense. In the nonlinear wave field under analysis, various modes, such as wave-induced mean currents and harmonics, co-exist along with the primary wave. Therefore, the velocity scale U_0 contains the contribution of primarily the leading-order (Tabaei *et al.*, 2005) reflecting wave but also the above-mentioned nonlinear dynamics. This approximate, nominal steepness A based on surface observation, is referred to through out this study, as an estimate of the degree of nonlinearity *locally* in the reflection zone, based on an *overall* characteristic velocity U_0 of the wave-induced motions observable at the surface. Moreover, we are motivated by engineering practicality to parameterize the mean surface current magnitude using $\{A, U_0\}$ rather than the strictly defined steepness or velocity scale associated with the primary wave only, since the former information may be easier to acquire via remote sensing with a shorter observation record, whereas the latter may require a highly resolved time series to isolate the wave component with adequate accuracy.

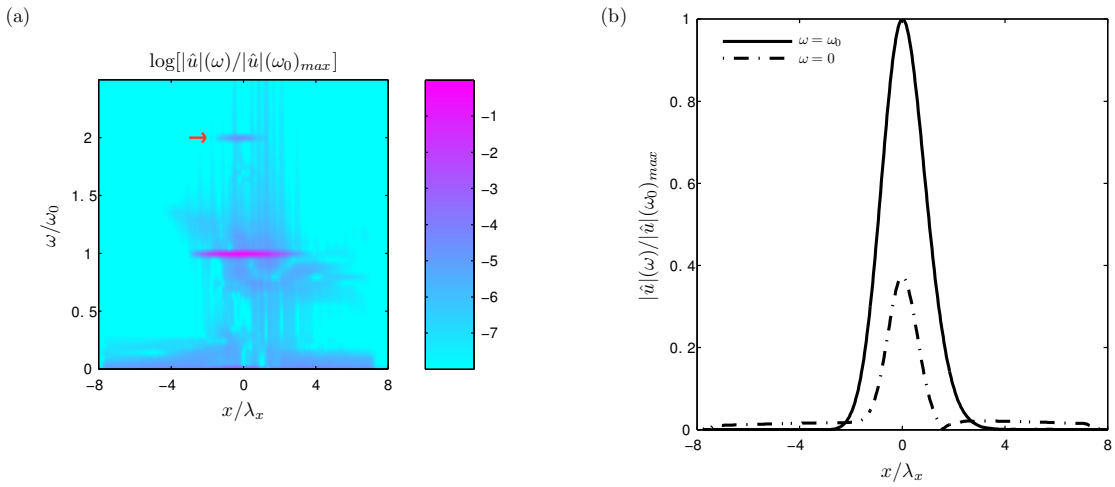

Figure 4.4: Surface profile of the frequency spectrum of u for T01: (a) colormap of $\log[|\hat{u}(x,\omega)|/|\hat{u}(x,\omega_0)|_{max}]$, and (b) 1-D profiles for $|\hat{u}(x,\omega_0)|$ and $|\hat{u}(x,0)|$, both normalized by $|\hat{u}(x,\omega_0)|_{max}$. $x=0$ at the intersection of the centerline of the beam and the surface. A weak signature of the second harmonic $\omega=2\omega_0$ is visible where a red arrow points at, and more details follow in §4.4. Solid line in (b) delineates the amplitude envelope of the reflecting wave at the surface; the envelope function remains a Gaussian with an estimated standard deviation $\sigma_{sfc}\simeq 0.861\lambda_x$, which corresponds to a half-width greater than that of the forcing envelope, i.e., $\sigma_x=0.538\lambda_x$.

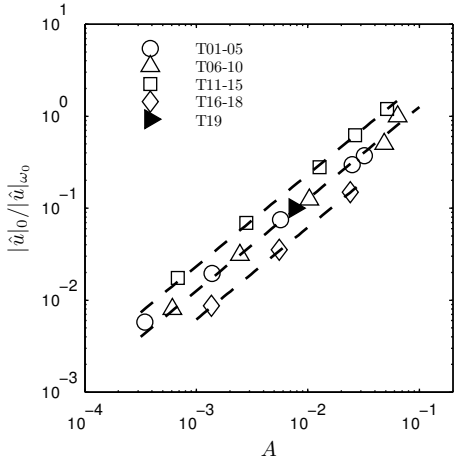

Figure 4.5: Variation of mean flow strength $|\hat{u}|_0/|\hat{u}|_{\omega_0}$ with wave steepness A; dash lines indicate least-squares fittings based on (4.14).

4.2.3 Scaling of mean surface flow

Here we aim to quantify the strength of the mean flow in an alternative way, i.e., by spectral analysis of temporal data of u, and to systematically correlate mean-flow strength with the wave characteristics. Although we limit our analysis to the velocity at the surface, our results can be easily extrapolated to any depth in the subsurface zone by appealing to the vertical mean-flow profile to be discussed in §4.3.

We seek a Fourier series expansion of u at the surface, i.e.,

$$u(x,t) = \sum_{\omega=-\infty}^{\infty} \hat{u}(x,\omega) e^{-i\omega t}, \tag{4.9}$$

where $\hat{u}(x,\omega)$ are the Fourier coefficients. Note that we have only considered the statistically stationary portion of the signal for this analysis, i.e., for each simulation case, we have excluded the initial transient before the reflected beam is fully developed.

The modulus of the Fourier coefficients $|\hat{u}(x,\omega)|$ (shown for $\omega \geqslant 0$) is presented for baseline case T01 in Fig. 4.4. Energy in u resides dominantly in two frequencies, i.e., $\omega = \omega_0$ (the forced-wave component), and $\omega = 0$ (the mean-flow component). The energy distribution is also localized in space, i.e., confined in the wave reflection/interaction region with their spatial peaks occurring at $x = 0$. By virtue of this observation, (4.9) can be approximated as

$$u(x,t) \simeq \hat{u}(x,0) + [\hat{u}(x,\omega_0) e^{-i\omega_0 t} + c.c.]. \tag{4.10}$$

To quantify the strength of mean flow and enable an across-case comparison, we will report the quantity $|\hat{u}(0,0)|/|\hat{u}(0,\omega_0)|$ (hereinafter referred to as $|\hat{u}|_0/|\hat{u}|_{\omega_0}$ for simplicity) for each simulation. This ratio compares the characteristic velocity

of the mean flow to a characteristic wave velocity. Applying (4.10) at $x = 0$ and recalling (4.8) we have that

$$\begin{aligned} u(0,t) &\simeq \hat{u}(0,0) + [\hat{u}(0,\omega_0)e^{-i\omega_0 t} + c.c.] \\ &\simeq \langle u \rangle_{x=0} + \mathcal{R}(U_{max}e^{-i(\omega_0 t+\phi)}) \\ &= \langle u \rangle_{x=0} + (U_0 e^{-i(\omega_0 t+\phi)} + c.c.) \ , \end{aligned} \tag{4.11}$$

where U_{max} and U_0 are real and ϕ is the spatial phase lag corresponding to $x = 0$. It can thus be seen that

$$|\langle u \rangle|_{x=0}/U_0 \simeq |\hat{u}(0,0)|/|\hat{u}(0,\omega_0)| = |\hat{u}|_0/|\hat{u}|_{\omega_0} \equiv \mathcal{M}. \tag{4.12}$$

The above ratio, denoted as $\mathcal{M}$ for compactness, describes the relative strength of the wave-generated mean flow to the wave.

In Fig. 4.5, $|\hat{u}|_0/|\hat{u}|_{\omega_0}$ is plotted against wave steepness A for all simulations in Table 4.1. Three families of points can be identified in Fig. 4.5, each corresponding to a single phase-tilt angle θ. Within each family, the points are aligned approximately on a single straight line on a log-log scale, suggesting a power-law dependence. We now discuss in detail Fig. 4.5 in the context of the parameter space identified in §4.1:

Beam compactness. When comparing between the baseline cases (T01-05) and the less-compact-beam cases (T06-10), data points for each case lie on a single straight line on Fig. 4.5. Therefore, the compactness of the beam does not have an appreciable role in determining the strength of the mean flow. However, as shown earlier by Fig. 4.3, it does impact the resulting vertical structure of the mean flow in the subsurface zone.

Reynolds number. An additional simulation T19 has been performed to clarify the effect of Re_p, the particle-velocity-based Reynolds number, which compares nonlinear acceleration to viscosity. T19 was modified from T03 by decreasing ν by an order of magnitude under the same geometric configuration and wave forcing. Despite the $O(10)$ or more difference in Re_p across T03 and T19, responsible for reduced viscous damping of the propagating wave in the latter case, the incident wave at the surface has a comparable steepnesses A in both simulations. Nonetheless, the data point from T19 lies within in the same family of data points with those contributed by the baseline geometry, i.e., T01-05, in Fig. 4.5.

The above observation indicates that for the range of Re_p values we have considered, this parameter does not seem to have an appreciable impact on the observed nonlinear effects in the reflection region. This behavior can be interpreted from two perspectives: First, for a general nonlinear IW problem, we expect that buoyancy effects (as a restoring force) are the primary counter-balance of the nonlinear inertial forces. Therefore, viscous effects are usually secondary, as compared to buoyancy, in terms of stabilizing the flow, and thus Re_p is irrelevant in describing the significance of nonlinear effects in the reflection zone. Second, for the specific setting of the current problem, i.e., reflection from a free-slip surface, no boundary layer can form, and the viscous effects linked to such a boundary layer are now absent. Finally, note, however, that Re_w, the wave-celerity-based Reynolds number, has an important role in determining the in-situ steepness of IW by effectively governing the pre-reflection viscous damping, as has been discussed earlier.

Nonlinearity. As indicated earlier, based on our observation of Fig. 4.5, we assume that the mean flow strength $|\hat{u}|_0/|\hat{u}|_{\omega_0}$, and the wave steepness A, a descriptor

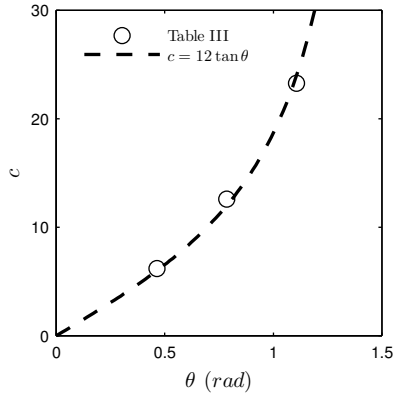

Figure 4.6: Variation of coefficient c in (4.14) with phase-tilt angle θ; dash line indicates fitted curve based on (4.16).

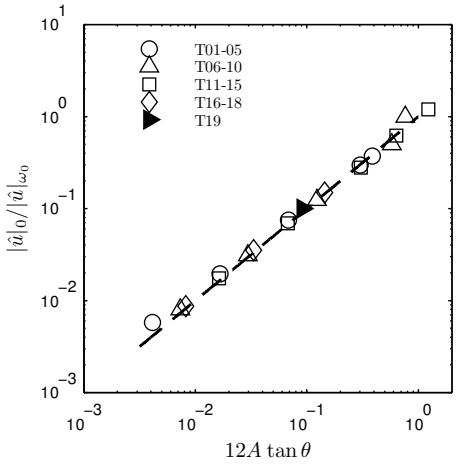

Figure 4.7: Variation of mean flow strength $|\hat{u}|_0/|\hat{u}|_{\omega_0}$ with $12\tan\theta A$, the proposed scaling parameter in (4.17); dash line indicates perfect agreement based on (4.17).

of degree of nonlinearity, are correlated by a power law, i.e.,

$$|\hat{u}|_0/|\hat{u}|_{\omega_0} = aA^b. \tag{4.13}$$

With the three distinct families of points in Fig. 4.5 in mind, we have performed least-squares fits to each of the three groups of points, each corresponding to a single phase-tilt angle θ. We have found that the power-law exponent b in (4.13) are reasonably constant among all θ's and considerably close to unity. Therefore,

Table 4.3: Least-squares-fitted coefficients c and coefficients of determination R^2 for $|\hat{u}|_0/|\hat{u}|_{\omega_0} = cA$.

θ	Run No.	c	R^2
27°	16-18	6.18 ± 0.16	0.9999
45°	01-10,19	12.61 ± 1.23	0.9481
63°	11-15	23.26 ± 0.46	0.9996

we are motivated to fix $b = 1.0$ and adopt a linear fit

$$|\hat{u}|_0/|\hat{u}|_{\omega_0} = cA, \tag{4.14}$$

where the least-squares-fit constant c depends only on θ. The scaling shown in (4.14) also agrees with the weakly-nonlinear theory (Tabaei *et al.*, 2005), the connection with which we will consider shortly.

Recalling (4.5) and (4.12) and re-writing (4.14), we have

$$|\langle u \rangle|_{x=0} \simeq cAU_0 = cN\lambda_x \sin\theta A^2, \tag{4.15}$$

which means that the nonlinear reflection-induced mean flow $\langle u \rangle$ (in its dimensional form) increases quadratically with wave steepness A, i.e., the degree of nonlinearity. This result agrees with Sutherland's corresponding findings for the scaling of the nonlinear-IW-induced mean flow when a wave packet propagates into a very weak stratification (Sutherland, 1996).

Angle dependence and a universal scaling law. Now we focus on our discussion of c in (4.14), a coefficient where the angle θ enters implicitly. The least-square-fitted c values are tabulated in Table 4.3 and also plotted in Fig. 4.6 against θ. Also plotted is Fig. 4.6 is a curve

$$c = 12 \tan\theta, \tag{4.16}$$

which we have found to fit the data points reasonably well.

A simple physical argument accounting for the role of the beam angle θ in determining the strength of the mean flow may be formulated by considering the two extreme values of θ, i.e., 0 and $\pi/2$. When $\theta = 0$, the beam propagates vertically. Based on observations for $\theta \neq 0$, the mean flow at the surface has a directional preference which is opposite to the corresponding component of the group velocity. For a vertically incident beam, since $c_{g,x} = 0$, there is no directional preference of the mean flow is present at the surface where the centerlines of incident and reflected beams meet, and thus there would be no mean flow. At the other limit, as $\theta \to \pi/2$, $\omega \to 0$, which means that the period is infinitely long and no wave component of the flow is likely to sustain itself, as a fluid parcel moves near-horizontally and the gravitational force is not oriented in such a way to serve as the restoring force. Any particle motion in this situation is likely to become a stationary flow. Therefore in the limit $\theta \to \pi/2$, the wave component is almost zero and the ratio $|\hat{u}|_0/|\hat{u}|_{\omega_0}$ approaches infinity. The function $\tan\theta$ happens to be a simple trigonometric function that satisfies these two limits simultaneously and matches well with the observations.

Combining (4.14) and (4.16), we obtain an empirical scaling law

$$\mathcal{M} = |\hat{u}|_0/|\hat{u}|_{\omega_0} = 12\tan\theta A, \tag{4.17}$$

which can be converted to dimensional form as

$$|\langle u\rangle|_{x=0} \simeq 12N\lambda_x \tan\theta \sin\theta A^2. \tag{4.18}$$

It can be seen in Fig. 4.7 that the scaling as described by (4.17) collapses data points contributed by all simulation cases considerably well.

4.3 Comparison to weakly nonlinear theory

4.3.1 Mean-flow structure

By relying on small-amplitude expansions, Tabaei *et al.* (2005) (hereinafter referred to as TAL) proposed an inviscid and weakly nonlinear solution for the reflection of an IW beam. Here we present a comparison between our viscous and fully nonlinear simulations and TAL; first, qualitatively, in terms of the structure of subsurface mean flow, and then quantitatively in terms of its strength relative to the wave velocity field. Note that TAL express their solution in terms of a dimensionless streamfunction which can not be compared directly to our results. The reader is referred to Appendix A for details on the derivations of expressions for the dimensional flow quantities of interest in the context of TAL.

A comparison on the mean flow structure can be made between Fig. 4.3(a), where the normalized mean velocity $\langle u \rangle$ is shown for a baseline case T01, and Fig. 4.3(c), where we apply TAL's solution to a beam that shares similar characteristics, i.e., phase-tilt angle and spatial compactness, to T01. To construct the theoretically computed profile in Fig. 4.3(c), we have set up the corresponding streamfunctions for the incident and reflected beams respectively, i.e., $Q^{inc\prime}$ and $Q^{refl\prime}$ (superscript $\prime$ denotes dimensionless quantities under TAL's scaling, which is shown in detail in Appendix A.) in (A.7) to match T01, so that the theoretical beam has $\theta = \pi/4$ and the same amplitude envelope function $A(\tilde{k}')$ (see (A.7)) as its numerically simulated counterpart for T01 at the surface, which shown in Fig. 4.4(b). The envelope function of the theoretically calculated beam is prescribed using the the actual compactness σ_{sfc}/λ_x of the numerical beam, rather than its nominal value σ_x/λ_x at the source. We then construct the mean structure

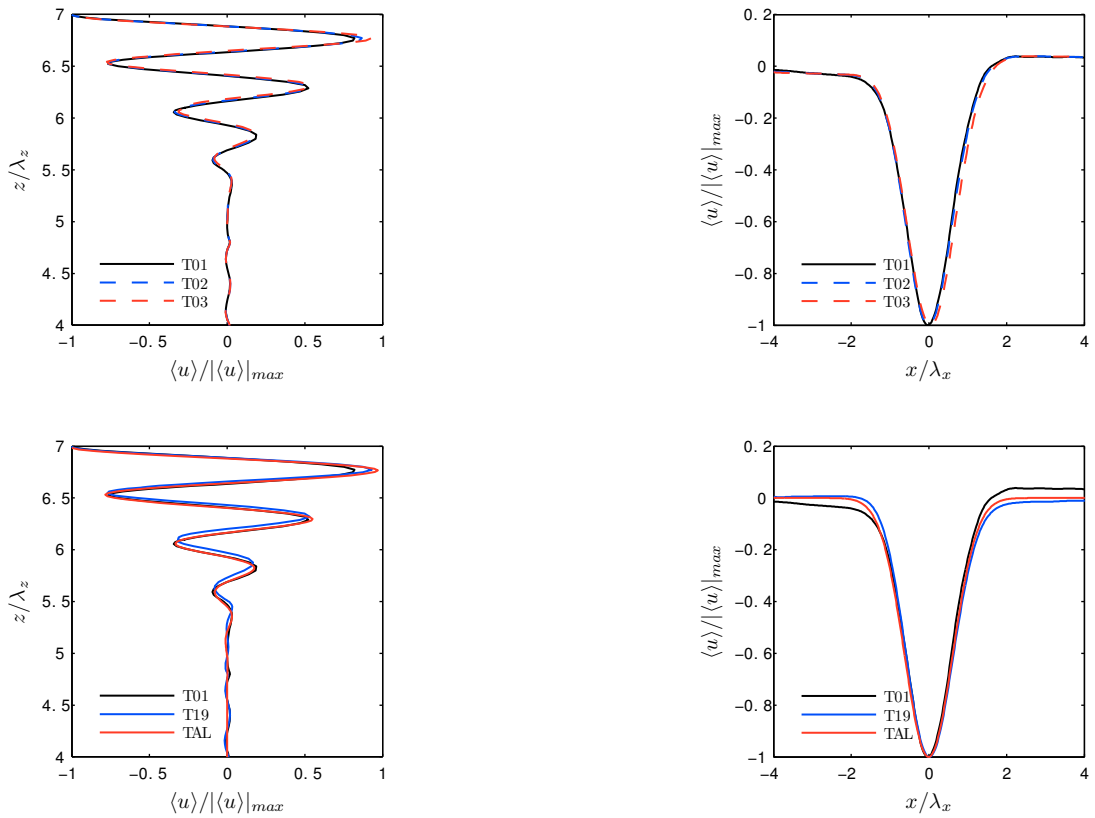

Figure 4.8: One-dimensional profiles of mean velocity $\langle u\rangle$ normalized by its maximum magnitude $|\langle u\rangle|_{max}$ which occurs at $(x, z) = (0, L_z)$ for each simulation. Vertical profiles on the left panel are taken at $x = 0$, and horizontal profiles on the right are taken at $z = L_z$. Data from simulations are taken at $t/T = 30$. The wave steepness $A_{T01} \simeq A_{T19} \gg A_{T02} \gg A_{T03}$; and the wave Reynolds number $Re_{w,TAL} = \infty \gg Re_{w,T19} \gg Re_{w,T01-03}$.

function U_0' in the asymptotic expansion, i.e., (A.4).

The mean flow structure reproduced by the simulations is in good agreement with that predicted by TAL's theory: a vertically layered structure is observed in both. Fig. 4.8 shows one-dimensional profiles of the normalized mean velocity $\langle u\rangle/|\langle u\rangle|_{max}$ for our baseline geometry. The left panel shows the profiles in the cross-stream direction, i.e., in z, and the right panel shows the streamwise profiles, i.e., in x. The horizontal axis is normalized by λ_x. Two sets of comparisons can

be made here. On one hand, in the upper two plots, we show simulation results for different values of wave steepness A, or particle-based Reynolds number Re_p, but with the same wave-based Re_w (see Table 4.1). Both horizontal and vertical profiles collapse very well on the upper plots, indicating that, under the scaling at hand, the structure of the mean flow is self-similar with respect to λ_x and $|\langle u \rangle|_{max}$. Therefore, the appropriately normalized profile is independent of the degree of nonlinearity of waves, as long as the wave kinematic properties, e.g. θ, σ_{sfc}/λ_x and Re_w, are the same. On the other hand, in the lower pair of plots, we compare across cases with varying Re_w: T01, with $Re_w = 29,900$; T19, with Re_w ten times that of T01; and the inviscid theory result of TAL, i.e., $Re_w \to \infty$. The profiles shown in the lower two subplots of Fig. 4.8 indicate good agreement between simulation results and theoretical prediction. For the range of Re_w that we have investigated, this agreement suggests viscosity has a minimal influence on the structure of the mean flow formation.

4.3.2 Mean-flow strength

Here we offer a comparison between the mean flow scaling, i.e., (4.17), and TAL. For TAL, we have obtained an analytical expression for the relative mean flow strength $\mathcal{M}$ as given by (A.16) for the case of *plane wave* reflection; however for the *wave beam* scenario, one has to apply TAL to a specific beam configuration as prescribed by (A.7), with prior knowledge of the wave magnitude envelope in wavenumber space, i.e., $A(\tilde{k}')$. This information can be obtained by an inverse Fourier transform of the spatial envelope of the wave beam at a representative location. For example, to apply TAL to our numerically generated beam, we sample the magnitude envelope at the free-slip surface, fit the profile to a Gaussian

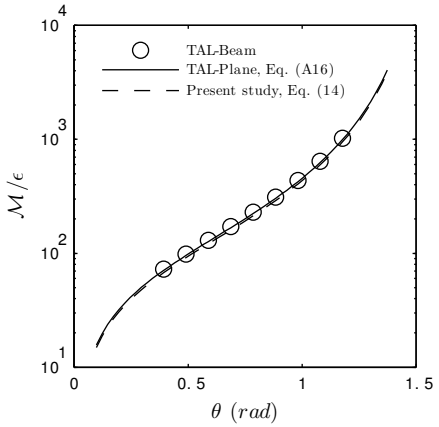

Figure 4.9: Comparison between the present study and TAL (Tabaei *et al.*, 2005) in terms of the relative mean flow strength $\mathcal{M}$ for a given wave amplitude ϵ as the phase-tilt angle θ varies.

function, and perform the analysis following TAL with this theoretical magnitude envelope representative of our numerically generated beam.

We are interested in how the mean flow strength $\mathcal{M}$ varies with wave nonlinearity, propagation direction and structural details of the beam, such as its compactness. Wave nonlinearity can be described either by the steepness A in the present study or by the amplitude parameter ϵ in TAL, where A and ϵ can be readily linked via (A.15). Our results, fitted reliably by (4.17), suggest that $\mathcal{M}$, as a measure of the relative strength of the mean flow to the wave, is linear in A or ϵ. Such a dependence agrees exactly with TAL, who, by virtue of the form of the expansion of (A.4), dictate that the wave component sets the leading-order term and that the mean flow term is one order higher in ϵ. Noting this agreement, one can focus the comparison on the role of phase-tilt angle on the mean flow, which is manifested by the coefficients in the linear relation between M and A (or ϵ), e.g., (4.17). Such a comparison is offered Fig. 4.9, where $\mathcal{M}/\epsilon$ are plotted against θ for three scenarios: first, our empirically derived scaling law for *beams*, i.e., (4.17); second, TAL applied to a *plane wave*, i.e., (A.16); and the last one where we apply

TAL to a *beam* with the same compactness (amplitude envelope function $A(\tilde{k}')$) as our baseline case but at various phase-tilt angles. All three functions agree considerably well. We interpret this agreement as follows: First, the plane wave and wave beam results computed via TAL differ only slightly, indicating that the mean-flow strength for theoretically computed waves is insensitive to the spatial compactness of the reflecting wave, be it a localized beam or a space-filling plane wave. Such a finding agrees with our observation (see Fig. 4.5). Second, our viscous simulations suggest a mean-flow scaling fairly close to the inviscid theory. The reader is to be reminded that this observation is only valid given that the degree of nonlinearity is sampled *locally* (see §4.2) at the reflecting surface, which indirectly has accounted for the viscous damping of the wave amplitude as the wave propagates from its source to the surface (see (4.7)). This implies that although we do have finite viscosity in our simulations, the flows are sufficiently inviscid within the reflection zone, i.e., Re_w is high enough, so that gravity remains the major counter-balance to nonlinearity and the mean-flow generating dynamics are close to the inviscid limit.

4.4 Harmonic generation

We now present some results on the generation of higher harmonics during the nonlinear reflection of an IW at a free-slip surface. As indicated ealier, the main focus of this dissertation is the numerical investigation of wave-induced (sub)surface currents and the comparison of our results to those of weakly nonlinear theory. We restrict our study of harmonics to a first assessment of their magnitude dependence on wave steepness at a free-slip surface and the change in this magnitude in the presence of a surface mixed layer. A more in-depth investigation of harmonic

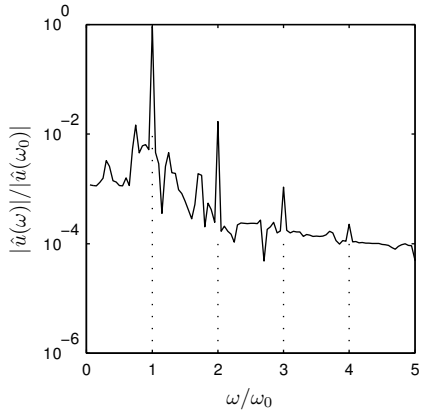

Figure 4.10: A typical temporal power spectrum for a fixed position in the reflection zone $(x, z) = (0.6\lambda_x, L_z)$ (T07). Distinct peaks occur at $\omega = n\omega_0$, where $n = 1, 2, 3, 4$.

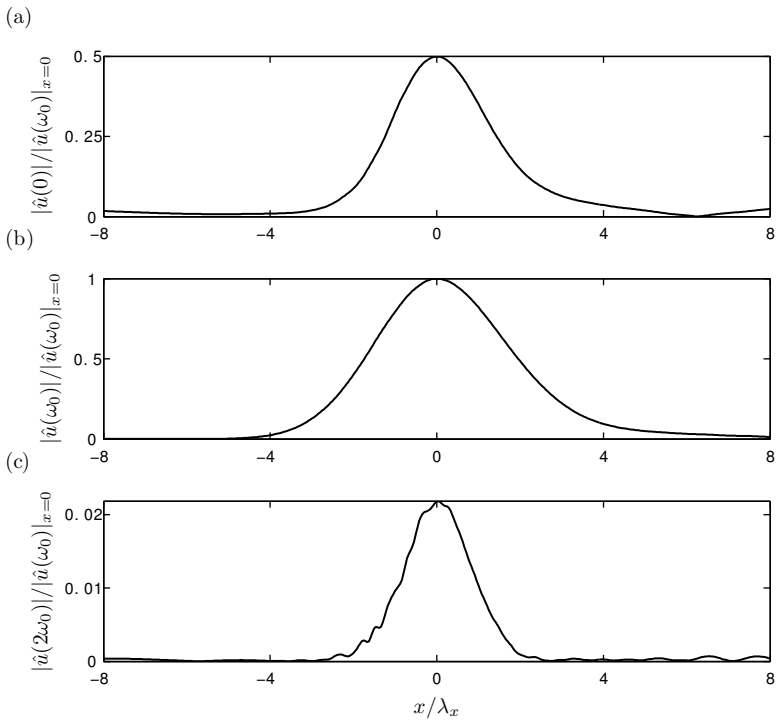

Figure 4.11: Spatial distribution of energy in various modes (T07) observed at the surface, i.e., $z = L_z$: (a) mean flow, (b) ω_0 and (c) $2\omega_0$. All values are normalized by the value for the forced frequency at $x = 0$, i.e., $|\hat{u}(\omega_0)|_{x=0}$.

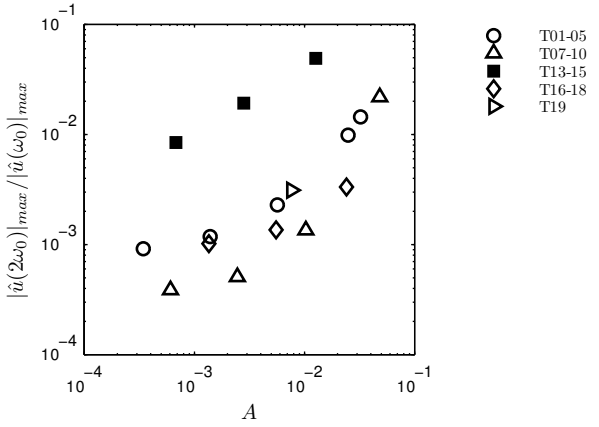

Figure 4.12: Variation of the strength of the second harmonic $|\hat{u}(2\omega_0)|_{max}$ normalized by the forced harmonic $|\hat{u}(\omega_0)|_{max}$ with the wave steepness A observed at the surface, i.e., $z = L_z$. T06, 11-12 are not shown as their temporal spectra drop fairly continuously and no distinct second harmonic can be observed. Filled squares denote a propagating mode, whereas hollow symbols denote evanescent modes.

generation is outside the scope of this dissertation and is deferred to future studies.

In Fig. 4.10, a sample plot of frequency spectrum of velocity u for a fixed location in the reflection zone is presented. Several distinct peaks can be observed at $\omega = n\omega_0$, where $n = 2, 3, 4$, indicating the generation of higher harmonics due to nonlinear wave-wave interactions (Teoh *et al.*, 1997; Javam *et al.*, 2000; Lamb, 2004; Tabaei *et al.*, 2005). Similar patterns in the frequency spectrum are observed for all simulations with the exception of T06, T11-12. In these three cases, the spectrum drops rather smoothly for $\omega > \omega_0$ and no distinct second harmonic is observed. Note that cases T06, T11-12 are some of the most strongly nonlinear simulations we have performed (see Table 4.1). In Fig. 4.11, we present the 1-D spatial distribution profiles of energy contained in the first three possible modes for T07, obtained at the free-slip reflecting surface. The energy contained in the mean flow ($\omega = 0$) and the second harmonic ($\omega = 2\omega_0$), both due to nonlinear

interactions, is distributed in well-defined spatial envelopes that approximately overlap with the forced wave mode, but of smaller sizes. Whereas the mean flow is comparable in magnitude to the primary wave, the second harmonic is only about 2% as energetic as the forced primary mode.

To obtain an appreciation for the variation of the amplitude of higher harmonics with respect to the wave nonlinearity, the relative strength of the second harmonic $2\omega_0$, as compared to the strength of the forced wave ω_0, is plotted in Fig. 4.12 against the wave steepness A. Within each wave geometric configuration, i.e., data points with the same symbol, the energy contained in the second mode, normalized by the forced wave mode, increases with steepness A. Additionally, the higher harmonics corresponding to propagating mode ($\omega \leq N$) in Fig. 4.12, contributed by T13-15, seem to have a significantly higher relative strength, as compared to those evanescent modes ($\omega > N$), which are denoted by filled symbols in Fig. 4.12. It is unclear whether there exists a universal scaling for the strength of this particular harmonic across different cases, which calls for further study.

4.5 Effect of a subsurface mixed layer

We now include a brief discussion on how a mixed layer beneath the surface could modify the reflection dynamics and surface response, as the top layer of the ocean usually is well-mixed (Thorpe, 2005). IW beams are expected to be reflected at the base of the mixed layer, known as a pycnocline. Recent research efforts have been made, both theoretically (Akylas *et al.*, 2007), numerically (Grisouard *et al.*, 2011), and experimentally (Mercier *et al.*, 2012), on the reflection of tidal IW beam off a pycnocline, as a candidate mechanism for generation of internal solitary waves. The

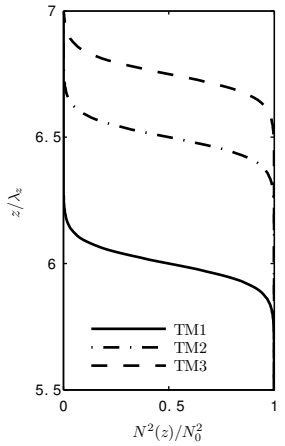

Figure 4.13: Buoyancy frequency profiles for TM1-3. The depth of the mixed layer is varied among the cases, the characteristic thickness of the transition zone 2δ is fixed at $\lambda_z/6$, and the free surface is located at $z = 7\lambda_z$.

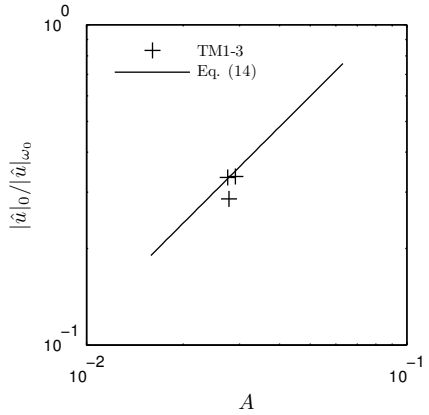

Figure 4.14: Characteristic mean flow strength $|\hat{u}|_0/|\hat{u}|_{\omega_0}$ at the center of the transition zone $z = z_0$, as compared to scaling given by (4.17) for mean flow due to reflection off a free-slip surface.

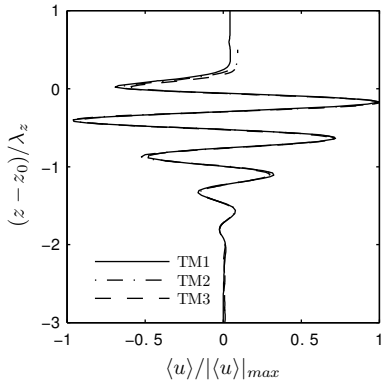

Figure 4.15: Vertical profiles of $\langle u\rangle/|\langle u\rangle|_{max}$ in the presence of a subsurface mixed layer. A shifted vertical coordinate relative to the center of the transition zone is adopted and normalized by λ_z. Profiles are sampled at x locations where the IW beam ray intersects with the mid-vertical-level of the transition zone.

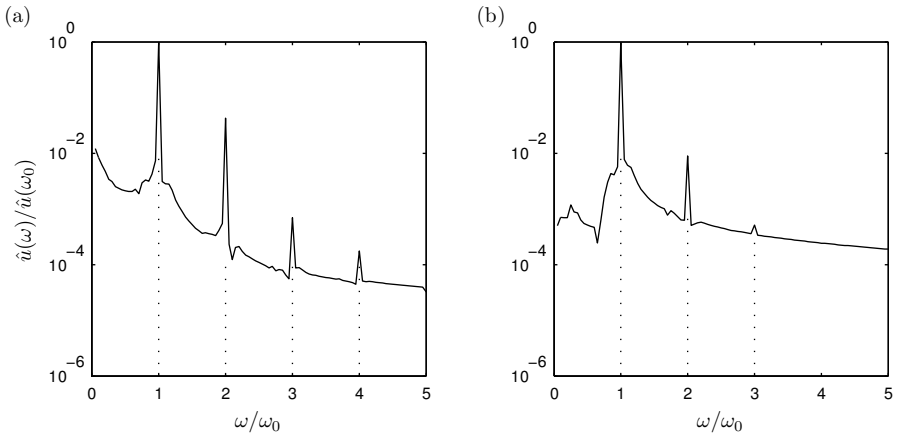

Figure 4.16: Sample temporal spectra for (a) TM3 at the transition zone and (b) T02 at the surface. Both spectra are sampled at the location where the centerline of the beam intersects with (a) the center of the transition zone ($z = z_0$) or (b) the surface ($z = L_z$).

purpose of the discussion here, however, is not to focus on the interaction of an IW beam with variable stratification, which alone could form a topic of detailed study, e.g., as done by others (Mathur and Peacock, 2009; Grisouard *et al.*, 2011; Mercier *et al.*, 2012). Instead we seek to obtain a qualitative appreciation of the nonlinear features, i.e., mean-flow and harmonic generation, due to the wave reflection off the base of a mixed layer, and how these might differ from the corresponding effects encountered during the reflection of an IW at a free-slip surface in a purely linear stratification.

Vertical profiles of buoyancy frequency $N(z)$ in the form of

$$N^2(z) = \frac{1 - \tanh(\frac{z-z_0}{\delta})}{2} N_0^2$$

are assumed in our simulations, where N_0 is the buoyancy frequency of the uniformly stratified fluid below the mixed layer, z_0 is the vertical location of the center of the transition zone of the buoyancy frequency, and 2δ is the characteristic thickness of the transition zone, which is fixed in the present study at $\lambda_z/6$. The $N^2(z)/N_0^2$ profiles are plotted in Fig. 4.13 for the three simulations labeled TM1, TM2 and TM3 respectively. These simulations use the same geometry as the baseline cases T01-05, but with variable stratification introduced. The parameter to vary among the three TM cases is the subsurface position of z_0, which is one vertical wavelength below the surface for TM1, one half for TM2, and one quarter for TM3. The phase-tilt angle θ is 45° for these simulation cases. These simulations so designed allow us to study the role of the mixed layer thickness in determining the surface observable flow characteristics, such as wave-induced mean flow.

Mean flow formation at the base of the mixed layer, where the incident IW beam is reflected, is indeed observed. The strength of the mean flow at a typical location in the pycnocline, i.e., $z = z_0$, quantified using the same approach

previously discussed, i.e., in terms of $|\hat{u}|_0/|\hat{u}|_{\omega_0}$, is plotted in Fig. 4.14 against the wave steepness A. A is again evaluated locally at the reflection region as done for the free-slip surface case. The mean-flow scaling we have derived for the free-slip reflection in a uniformly stratified fluid, which is given by (4.17), is also shown in Fig. 4.14 for the purpose of comparison. Given the same wave characteristics, the mean flow strengths due to reflection off a mixed layer and that off a free-slip surface are actually quite comparable. A similar mean shear profile to those uniformly stratified cases shown in Fig. 4.8, is shown in Fig. 4.15 for the TM cases. An oscillatory mean flow pattern forms over a vertical extent of length approximately $2\lambda_z$ below the center of the pycnocline ($z = z_0$) and extends for roughly $\lambda_z/4$ above it. For $z - z_0 \leq 0$, the mean flow profiles in the vertical are similar to those previously shown for the free-slip cases. Laboratory work by Mercier *et al.* (2012) reports observations in terms of mean-flow generation under a pycnocline due to IW beam reflection, but the mean flow they observe is usually unidirectional, i.e., towards the direction in which the wave energy propagates. In some of their cases though, an oscillatory pattern in mean horizontal velocity is observed, which is partially in agreement with our results.

In Fig. 4.8, as one extends upward from $z = z_0$ to the very surface, the wave-induced mean flow first decays in magnitude, then reverses its sign from negative to positive (presumably to maintain continuity within the mixed layer), and soon becomes almost constant. The mean flow at the free-slip surface now points in the same direction as the wave group velocity, and the magnitude of the wave-induced surface mean flow ranges from 4.4 to 9.3% of the maximum mean flow strength which occurs within the wave reflection zone. Therefore, as compared to the uniformly stratified case, the presence of a mixed layer enables a significant reduction in the surface value of the mean flow associated with the reflection of

the IW off the pycnocline.

Harmonic generation is also observed within the pycnocline when an IW beam is being reflected, as shown in Fig. 4.16(a) for TM3 (TM1-2 show very similar results). T02, a case with a comparable wave steepness ($A = 2.50\%$ at $z = L_z$) to TM3 ($A = 2.78\%$ at $z = z_0$), but simulated for reflection off a free-slip surface, is shown in Fig. 4.16(b) for comparison. More higher harmonics can be observed in TM3 than its uniformly stratified counterpart T02. Additionally, more energy is contained in these super-harmonics in TM3. It can thus be inferred that reflection off a pycnocline is a flow setting more favorable for higher harmonic generation, as compared to reflection off a surface in a uniformly stratified fluid. To this end, presumably, the refracting wave inside the pycnocline provides for an additional, more efficient nonlinear interaction, with the incident wave. The details of this interaction are a topic of separate study.

4.6 Instabilities during late-time reflection

Here we discuss some qualitative observations of wave instabilities in the reflection zone at late times of reflection which are observed for cases T06 and T07. These two simulations have $\theta = 45^\circ$ and high values of steepness, A=6.4% and 4.8%, respectively. Examples of such instabilities are shown in Fig. 4.17 for T06. In the xt-plot shown in Fig. 4.17(a), disturbances start to occur at $t/T \simeq 30$ and continue to grow until the end of the simulation, when the well-defined wave structure that is seen in earlier stages of the reflection process, i.e., $20 < t/T < 30$, can no longer be distinguished. In T07, for which A is comparable but smaller than T06, similar disturbances occur as well, but at an even later time, i.e., $t/T \simeq 50$. In

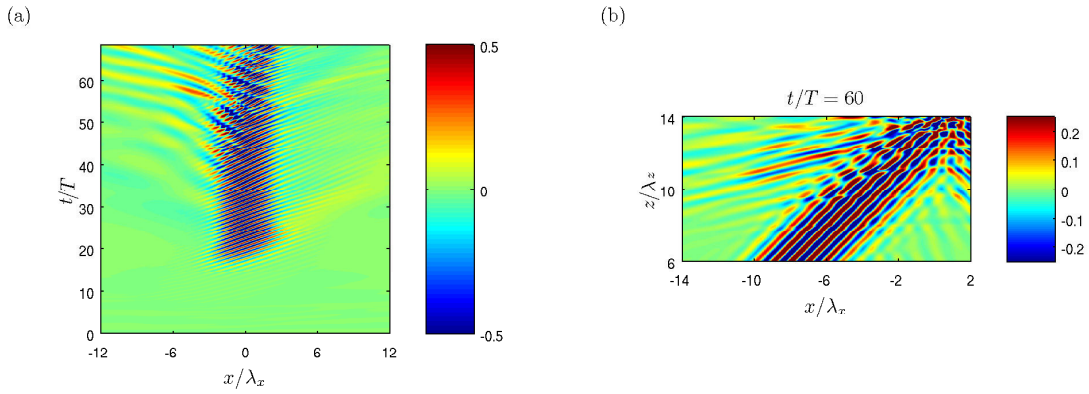

Figure 4.17: Instabilities at late time of IW reflection (T06): (a) xt-contours of u at the surface and (b) xz-contours of u, a snapshot $t = 60T$. Values of u are normalized by the maximum velocity magnitude U_{max} at the surface before wave instability occurs.

Fig. 4.17(b), where a snapshot of the unstable wave field in the xz-plane is shown, one can observe a secondary wave being radiated out from the lee side of the reflection region of the primary wave. This secondary wave has a phase-tilt angle that is more inclined to the horizontal as compared to the incident primary wave. By virtue of the dispersion relation, this behavior indicates a lower frequency than that of the primary wave. Energy carried by the primary wave is lost to the secondary waves, which transport the energy away from the reflection region.

These secondary waves may be regarded as a manifestation of subharmonic instability. One possibility is that the reflection-induced mean shear may trigger Kelvin-Helmholtz instabilities (Thorpe, 2005). However the local Richardson number computed for this case (see §4.2), well above the critical value, seems to discard this possibility. Another type of instability that has been reported for colliding IW beams is overturning instability due to energy accumulated in higher harmonics (Teoh *et al.*, 1997; Javam *et al.*, 2000). No overturning, however, has been observed in our simulations. One highly possible nonlinear mechanism for

the observed instability could be the parametric subharmonic instability (PSI) (Staquet and Sommeria, 2002; Sutherland, 2010; Joubaud *et al.*, 2012), which we discuss below in greater detail.

PSI consists of resonant triad interactions which satisfy specific temporal and spatial resonance conditions, e.g., as recently reported by Joubaud *et al.* (2012) in their laboratory experiments. To determine whether the instability waves we observe satisfy the particular resonance conditions, we here perform a case study on the above-mentioned simulation T06 (Fig. 4.17) by applying the Hilbert transform approach outlined by Mercier *et al.* (2008). To this end, we analyze the u velocity data for the last 10 (incident) wave periods of T06, a time interval during which the instabilities have fully developed. A sample xt-diagram from this data set is shown for the surface ($z = L_z$) in Fig. 4.18(a).

First, Fourier analysis in the temporal domain suggests three dominant frequencies (besides the mean currents at $\omega = 0$): the primary (incident) wave frequency ω_0 and two subharmonic frequencies $[\omega_1, \omega_2] \approx [0.68, 0.32]\omega_0$, which altogether satisfy the temporal resonance condition:

$$\omega_0 = \omega_1 + \omega_2.$$

When considering the surface as a typical location, the maximum spectral amplitudes of ω_1 and ω_2, computed during the time interval analyzed, are approximately 50% and 70%, respectively, of that corresponding to ω_0.

Second, we *demodulate* (Joubaud *et al.*, 2012) the time series by band-pass filtering around ω_0, ω_1 and ω_2 respectively and obtain the demodulated signal $\tilde{u}$ for each of the frequencies, as shown for the surface in Fig. 4.18(b)-(d). xz snapshots for each frequency at $t/T = 60$ are in Fig. 4.19(a)-(c), whereas the original instantaneous flow field has been shown in Fig. 4.17(b) .

Finally, applying the two-dimensional spatial fourier transform (in xz) to the demodulated signal $\tilde{u}$ of each of the above frequencies, we identify the dominant wavenumber pairs $\vec{k}_0$, $\vec{k}_1$ and $\vec{k}_2$. We can now test against the spatial resonance condition:

$$\vec{k}_0 = \vec{k}_1 + \vec{k}_2.$$

As can be seen in Fig. 4.20, this condition is satisfied reasonably well. To conclude, the above results suggest that these instabilities observed are indeed originated from PSI-like mechanisms. Nevertheless, we emphasize that the sole purpose of the above analysis is to identify the nature of the observed instability via some first analyses. Further, more detailed, probing into the underlying mechanism of PSI is a highly intriguing avenue of investigation in its own, which certainly deserves more systematic studies in the future.

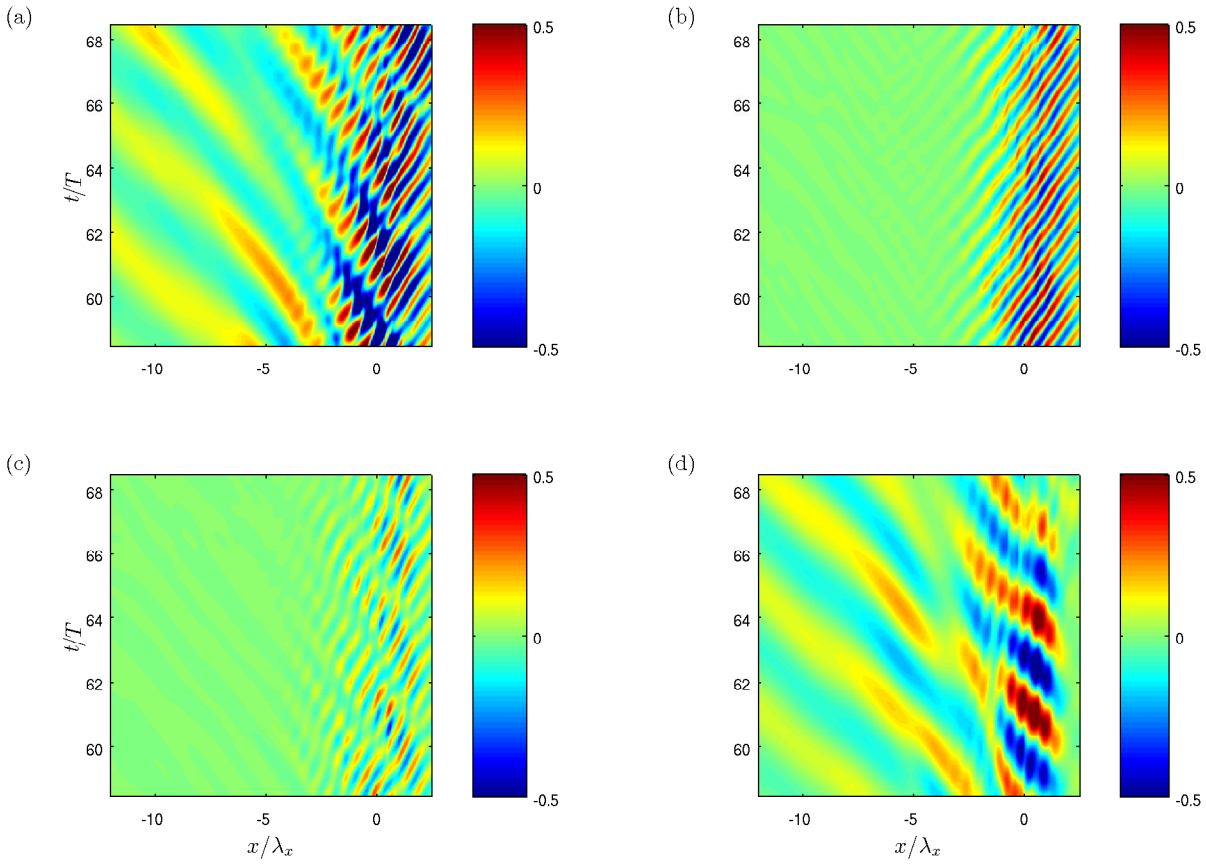

Figure 4.18: xt-contours of surface u velocities during wave instabilities (T06): (a) directly observed u, (b)-(d) demodulated $\tilde{u}(x, z = L_z, t, \omega) + c.c.$ for $\omega = [\omega_0, \omega_1, \omega_2]$ respectively. Same velocity normalization as Fig. 4.17 is used.

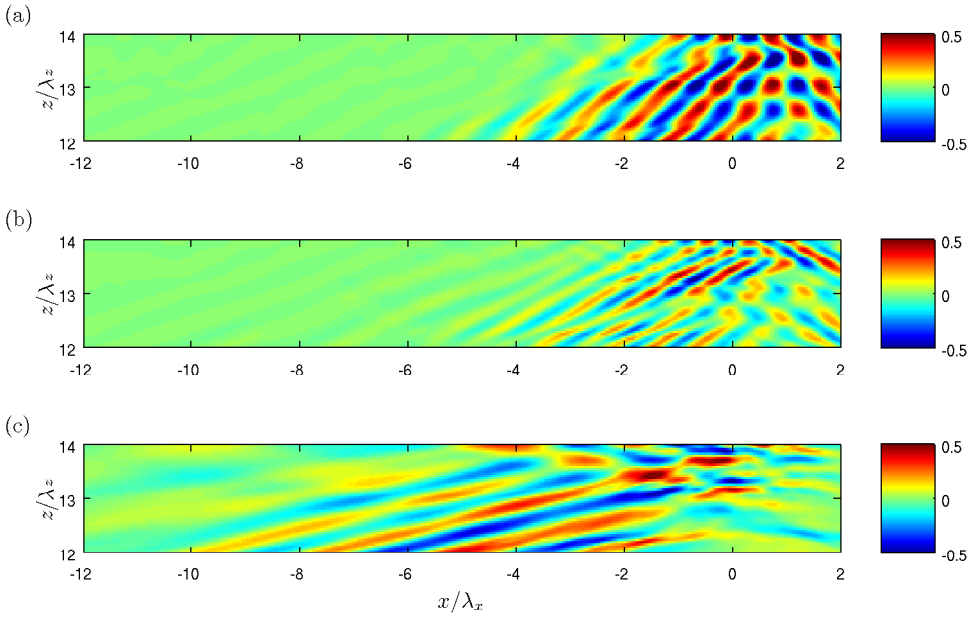

Figure 4.19: xz-contours of demodulated u velocities, $\tilde{u}(x,z,t,\omega) + c.c.$, at $t/T = 60$ in the subsurface instability zone (T06): (a) $\omega = \omega_0$, (b) $\omega = \omega_1$ and (c) $\omega = \omega_2$. Same velocity normalization as Fig. 4.17 is used.

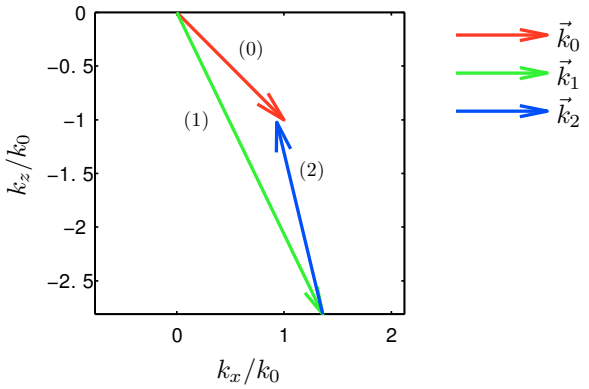

Figure 4.20: Spatial resonance condition in the instability zone (T06). $\vec{k}_0$ corresponds to the primary wave, and $\vec{k}_1$ and $\vec{k}_2$ are two subharmonics. Wavenumber vectors are normalized by $k_0 = 2\pi/(\text{unit length})$. Number in the parenthesis near the vector is the corresponding subscript of $\vec{k}$.

CHAPTER 5

INTERNAL WAVE REFLECTION: LAGRANGIAN DYNAMICS

5.1 Small-amplitude analysis

In this section, results on two-dimensional small-amplitude analysis of Lagrangian flow within reflecting IWs are discussed. Readers who are interested in the details of the derivation are referred to Appendix B. Of particular interest is the wave-mean Lagrangian motion of fluid particles, which can be decomposed into the Eulerian mean flow $\langle u \rangle$ and the Stokes drift u_S, as shown in (B.8). At the second-order in the wave steepness A, i.e., $O(A^2)$, the mean Lagrangian drift $\langle u_{L,II} \rangle$ consists of the Eulerian mean flow $\langle u \rangle$, and the $O(A^2)$ Stokes drift $u_{S,II}$,[1] the latter exclusively driven by the $O(A)$ reflecting waves (see the scaling arguments in Appendix B.1). The analyses shown in Appendix B.2 suggest that, for an inviscid reflecting plane IW off a rigid horizontal surface, $\langle u \rangle$ and $u_{S,II}$ cancel each other out completely everywhere in the flow, driving no net Lagrangian transport up to the second order.

This is, to the best of our knowledge, the first time that an explicit derivation has shown that, for an inviscid plane IW reflection at a horizontal surface, the Eulerian mean flow and Stokes drift cancel each other out up to $O(A^2)$. Thorpe (1987, 1997), in his studies of plane IW reflection off a slope bottom boundary, anticipated that the mass transport within the inviscid waves is zero, without showing an explicit derivation. According to Thorpe (1987) (pg. 283), no Lagrangian mean flow is expected within plane IW reflecting upon a solid slope, "as it must to preserve the density field" in a non-diffusive set-up. This argument is appropriate for the case of a sloping boundary, as any net mass transport in the

[1] Here and elsewhere, Roman numerals in subscripts denote orders of dynamics, e.g., "II" in the subscript of $u_{S,II}$ denotes an $O(A^2)$ effect.

along-slope direction would involve permanent perturbation to the density field and is therefore expected to vanish. However, the same reasoning might not be directly applicable to our case with a horizontal reflecting surface, as the mean Lagrangian motion in the horizontal direction (parallel to the reflecting surface) does not induce diapycnal mass transport, and thus cannot be ruled out simply by Thorpe's argument based on the preservation of the density field.

The $O(A^2)$ analysis for a plane IW can be readily extended to an IW beam. A sample calculation is shown here for an IW beam of the same geometry as the ones studied in simulations T01–05 of Z&D, i.e., IW beams of $\theta = 45^\circ$ and surface-observed compactness $\lambda_x/\sigma_{sfc} = 1/0.861$, where σ_{sfc} is the half-width of the wave envelope at the surface along the x axis (see the DNS set-up in Fig. 4.1). Specifically, the wave kinematics, including the primary wave $(u, w)_I$ and the mean flow $\langle u \rangle$, can be obtained by applying the TAL theory (Tabaei *et al.*, 2005). (B.16) to (B.21) can be computed numerically for any IW beam with known characteristics to obtain the second-order Stokes drift.

The results of such second-order analyses on Eulerian mean flow and Stokes drift due to a reflecting beam are shown in Fig. 5.1. In contrast to the plane IW reflection case where the waves fill out the entire domain and produce nonlinear effects (either Eulerian mean or Stokes) everywhere, as suggested by (B.14) and (B.22), the incident and reflected IW beams produce $O(A^2)$ effects only where the two beams overlap beneath the reflecting surface. Other than the spatial confinement of any nonlinear effect, there is no substantial difference between the plane IW and IW beam cases in terms of Lagrangian mean flows of $O(A^2)$: The Eulerian mean flow $\langle u \rangle$ in Fig. 5.1a and second-order Stokes drift $u_{S,II}$ in Fig. 5.1b have exactly the same structure but opposite signs everywhere in the

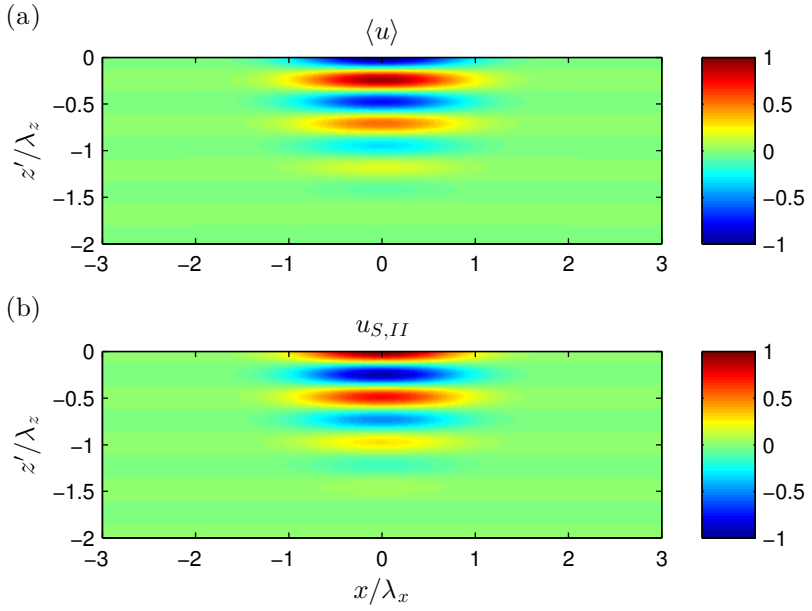

Figure 5.1: (a) Eulerian mean flow, $\langle u \rangle$, as predicted by the TAL (Tabaei *et al.*, 2005) solution, and (b) second-order Stokes drift, $u_{S,II}$, due to a reflecting IW beam of $\theta = 45°$ and compactness $\lambda_x/\sigma_{sfc} = 1/0.861$. Both velocities are normalized by $2U_0^2/c_x$. $(x, z') = (0, 0)$ is the point where the centerline of the incident beam hits the reflecting surface, and the incident and reflected beams overlap approximately within $-\lambda_x < x < \lambda_x$ and $-\lambda_z < z' < 0$. The two velocity fields, $\langle u \rangle$ and $u_{S,II}$, which are computed independently, have the same magnitude but opposite signs everywhere in the flow, and thus they cancel out each other *completely*.

flow. Therefore, due to the complete cancellation of Eulerian mean and Stokes drift, one would expect no net $O(A^2)$ Lagrangian effects within an inviscid weakly nonlinear reflecting IW beam. However, when the fluid does become viscous, the cancellation is not expected to hold; in the next section, results from viscous fully-nonlinear computations, showing net Lagrangian effects that are presumably of viscous origin, are presented.

5.2 Numerical particle tracking

5.2.1 Parameter space

The parameter space associated with numerical particle tracking (see §3.5 for details on the implementation), covering various wave configurations (see Table 5.1) examined by Z&D and particle characteristics considered in the present study, is described below:

Wave configurations. The first dimension of our parameter space results from the specific wave configurations examined by Z&D which sought to cover a range of wave amplitudes A, beam angles θ (also a measure of the wave's hydrostaticity (Sutherland, 2010)), beam compactnesses λ_x/σ_{sfc} and Reynolds numbers Re_w. For the purpose of the Lagrangian study in this paper, waves of very small amplitudes ($A < 0.25\%$), which were examined by Z&D in the Eulerian reference frame, will not be considered. These very-small-amplitude waves may drive very weak nonlinear Lagrangian effects, the magnitudes of which are expected to be comparable to those of the small interpolation errors of the high-accuracy numerical particle tracking.

Particle characteristics. A particle to be considered is defined by its initial position (x_0^+, z_0^+) and initial time t_0 at which it assumes the designated initial position. To obtain a full coverage of the three-dimensional parameter space (x_0^+, z_0^+, t_0) associated with particles, the following strategy is used. A batch of particles are inserted at the same set of positions at q (typically 18) evenly-spaced phases of the wave cycle respectively to cover various t_0's. After the insertion, a particle is typically tracked for five wave periods. A two-dimensional array of p^2 particles

Table 5.1: Summary of wave configurations that are considered for the Lagrangian study. θ is the angle between the group velocity vector of the IW beam and the vertical direction; σ_{sfc} is the observed wave envelope half-width at the surface; $Re_w \equiv \lambda_x^2 N/\nu$ is the wave-based Reynolds number; $A = U_0/(N\lambda_x \sin\theta)$ is the dimensionless wave amplitude (steepness).

Run no.	θ (deg)	σ_{sfc}/λ_x	Re_w	A (%)	Run no.	θ (deg)	σ_{sfc}/λ_x	Re_w	A (%)
01	45	0.861	29,900	3.23	**11**	63	0.936	299,000	5.14
02	45	0.861	29,900	2.50	**12**	63	0.936	299,000	2.65
03	45	0.861	29,900	0.569	**13**	63	0.936	299,000	1.27
					14	63	0.936	299,000	0.281
06	45	1.608	74,700	6.38	**16**	27	0.776	29,900	2.41
07	45	1.608	74,700	4.83	**17**	27	0.776	29,900	0.554
08	45	1.608	74,700	1.03	**19**	45	0.860	299,000	0.763

(typically $p = 16$) are inserted at each designated insertion time uniformly in space to cover one wavelength in both x and z' within the core of the IW beam reflection zone, i.e., on $-\lambda_x/2 < x \leq \lambda_x/2$ and $-\lambda_z < z' \leq 0$, where $(x, z') = (0, 0)$ is the position at which the centerline of the incident beam intersects with the top surface. As a result, to calculate the desired Lagrangian statistics, a population of $p^2 q = 16^2 \times 18 = 4,608$ particles are tracked for each wave configuration to cover a complete range of (x_0^+, z_0^+, t_0) combinations within a reflecting IW beam. The particles are tracked when the nonlinear reflection region has fully developed in the simulations, i.e., there is no transient effect due to the initial impingement of the beam onto the surface. For cases where the beam will later undergo parametric subharmonic instabilities (PSI), i.e., T06, T07 and T11, particle tracking is performed at earlier stage of the reflection before any effect of subharmonic waves has established.

5.2.2 Particle orbits

This section presents qualitative yet highly insightful results on the orbits followed by Lagrangian particles within a reflecting IW beam. A first understanding of particle kinematics may be obtained by inspecting the particle trajectories with respect to t_0, the time at which the particles are initiated at the designated locations. One salient point of these animations is that the exact positions of the particles during the wave cycles depend strongly on the initial time of tracking, although the particles are initiated at the same set of locations, which confirms the necessity of including t_0 in our parameter space.

One can qualitatively observe differing degrees of wave-mean drifts in the particle orbits from one wave cycle to the next, for various wave configurations under consideration (see Table 5.1):

When the wave steepness A is considerably small (i.e., T01–03, T16–17, T14), particle trajectories for multiple wave periods (not shown) virtually overlap into one visible orbit for each (x_0^+, z_0^+) location, which means that the drift of the mean orbital position during these wave cycles is very small.

When the steepness A increases sufficiently beyond the value of the most linear cases considered above, the amount of drift does become significant. An example from T13 is shown in Fig. 5.2. The particle motions maintain their periodicity while the mean orbital position drifts weakly but noticeably during the wave cycles, a feature that can be observed in T06–07 and T13.

When A increases further, the drifts become even more significant (i.e., T11–12). An example from T12, with amplitude almost doubled from T13 (Fig. 5.2), is shown in Fig. 5.3. Due to the larger amount of drift in the particles' mean orbital positions, the shape of the orbits of some particles undergoes noticeable changes from the previous wave cycle to the next (see the differences in the blue and red orbits in Fig. 5.3). Interestingly, although the particle Lagrangian motion has partially lost its periodicity in time, suggesting that the waves are of rather high amplitudes and thus highly nonlinear, these waves are fairly stable when viewed in the Eulerian reference frame.

It is also interesting to note that a beam angle θ that is more inclined to the horizontal seems to drive more significant Lagrangian drifts; among the three beam examined, the most dramatic drifts are observed for the the "shallowest" beam (greatest inclination to the horizontal and thus the most hydrostatic (Sutherland, 2010)), i.e., with $\theta = 63°$. Parameterization of Lagrangian drifts as a function of both A and θ will be discussed in the following subsection.

5.2.3 Mean Lagrangian drifts

Drift direction and particle dispersion

Here the wave-mean Lagrangian drift or mass transport velocity $\langle u^+ \rangle$ is considered. Of interest is the direction of $\langle u^+ \rangle$ as one scans vertically through the water column. This can be observed visually by comparing the particles' horizontal positions before and after the wave effects, and a typical plot is shown in Fig. 5.4 for T13. Driven by the reflecting IW beam, particles disperse horizontally around the x position at which they are inserted; the depth-averaged mean position of

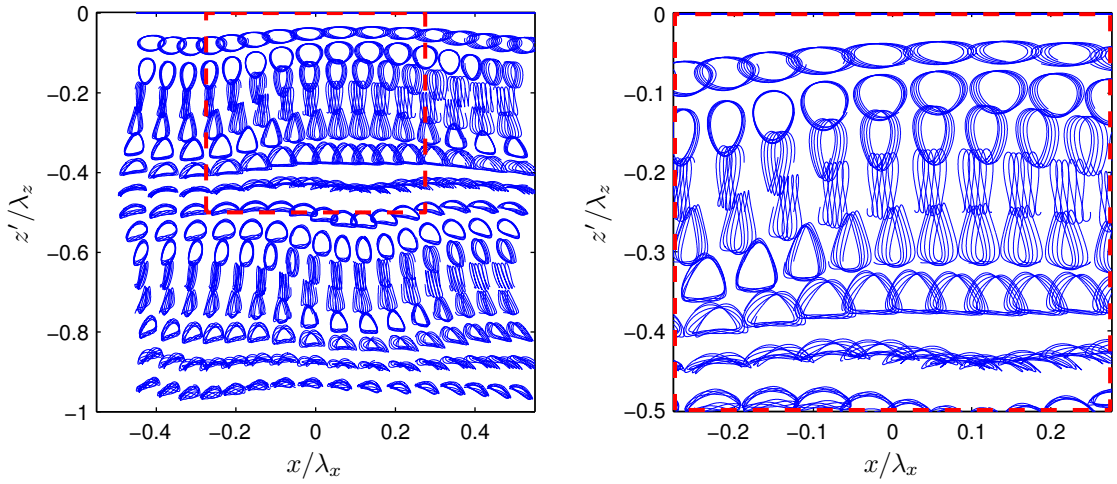

Figure 5.2: Typical particle orbits from T13 ($A = 1.27\%$ and $\theta = 63°$). Left panel shows the full field of view; right panel shows a zoomed-in view within the dashed-line box drawn in the left panel. Trajectories of a two-dimensional array of $16 \times 16 = 256$ particles are plotted over five wave periods. A net drift can now be observed for each initial position, while the orbital shape remains repeatable from one wave cycle to the next.

the particles do not seem to be shifted significantly. The degree of the horizontal dispersion seems to grow with x, suggesting some spatial inhomogeneity of the particle drift statistics in the horizontal direction.

Horizontal profiles

Here the statistics of wave-mean drift $\langle u^+ \rangle$ is considered. The results reported here are obtained by averaging over five wave periods to minimize the statistical uncertainty of averaging over one period only as in the standard definition of the operator $\langle . \rangle$ in (B.6). Our specific goal here is to examine how the depth-averaged drifts vary in x. The particles tracked have covered the three-dimensional parameter space (x_0^+, z_0^+, t_0); for each x_0^+, averages are taken over all p z_0^+ locations, covering one wavelength λ_z, and all q insertion time t_0's, covering one wave period.

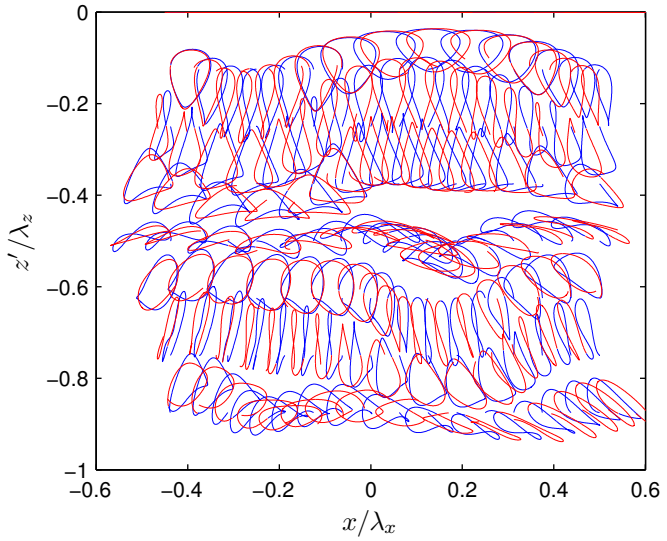

Figure 5.3: Typical particle orbits from from T12 ($A = 2.65\%$ and $\theta = 63°$). Particle orbits are shown for two wave cycles only: Trajectories during the first cycle are drawn in blue, and the immediate following cycle in red. Particles are downsampled in the vertical for clarity. The orbital shape of some particles varies from the previous wave cycle to the next, and a great amount of net drift in the mean orbital position can be observed.

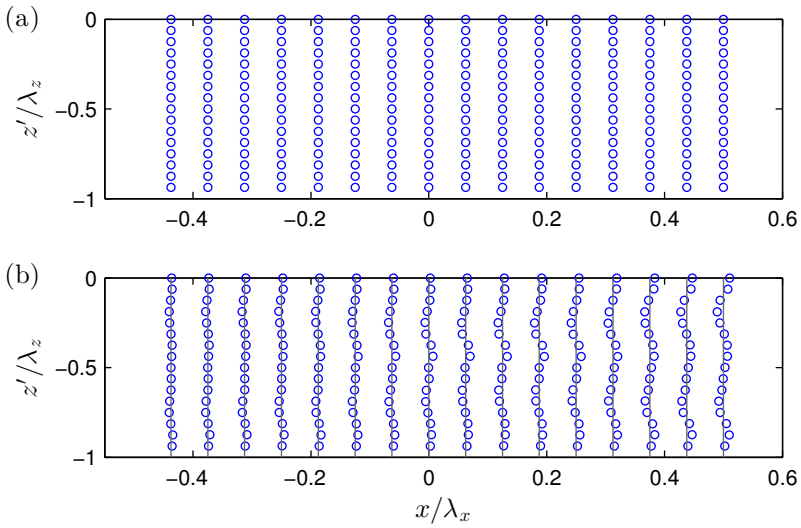

Figure 5.4: Particle positions (x_0^+, z_0^+) at (a) the beginning and (b) the end of five wave periods (T13). Marked grey in (b) is the initial x positions at which the particles are inserted. Particles shown are inserted at the same phase of the wave.

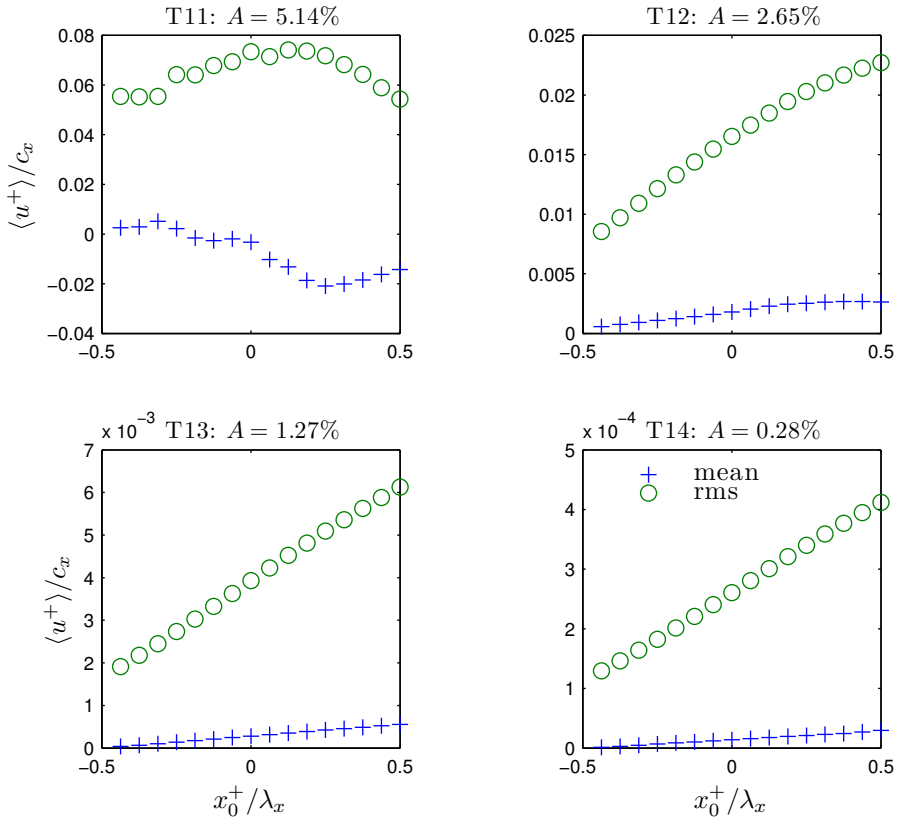

Figure 5.5: Horizontal profiles of depth-averaged mean (plus) and rms (circle) wave-mean Lagrangian drifts $\langle u^+ \rangle$ from T11–14. Velocities are scaled by the horizontal wave phase speed c_x, and the coordinates are scaled with horizontal wavelength λ_x.

Both the arithmetic mean and the quadratic mean (rms) based on $pq = 16 \times 18 = 288$ particles at each x_0^+ are considered.

Typical horizontal profiles of these mean drifts can be found in Fig. 5.5 for T11–14. These runs are chosen to be shown as they cover various degrees of particle drifts at the same beam angle $\theta = 63°$ (Table 5.1). First, for all cases, the rms mean is one order of magnitude bigger than the arithmetic mean, which means that the variations in $\langle u^+ \rangle$ at each horizontal location in the water column are much greater than the depth average of them. This implies that the reflecting IW beam is much more effective in dispersing the particles in opposite directions

horizontally throughout the water column, than in drifting the particles towards a preferred direction.

Second, for T12–14, the drifts increase monotonically with x in $-0.5\lambda_x < x < 0.5\lambda_x$, which suggests that the maximum drift magnitude may occur at $x > 0$, i.e., where the beam centerline has already deflected. The exception to this observation is T11, the most nonlinear case among all, where the drift is almost constant in x. It is somewhat unexpected to see such dependence of Lagrangian statistics in x over one wavelength λ_x; however, note that x is not a statistically homogeneous direction in the IW beam reflection set-up — the wave does vary in x due to the structural modulations imposed by the wave envelope, as well as due to the viscous decay of wave amplitude along the path of the wave's (energy) propagation.

Finally, the magnitude of the drift clearly increases with wave steepness A, e.g., for T11, the rms drift exceeds 5% of phase speed c_x, which implies a considerable amount of wave-induced mass transport; the scaling of the drifts with wave parameters for all cases is discussed next.

Scaling

Fig. 5.6 shows the Lagrangian mean drift velocity scale U_L, taken as the maximum rms $\langle u^+ \rangle$ at all x_0^+'s for each wave configuration, plotted against $A \tan\theta$, a parameter which has successful scaled the Eulerian mean flow in Z&D and is consistent with the TAL (Tabaei *et al.*, 2005) theory. Firstly, the plot clearly suggests a quadratic dependence of U_L on A, although small-amplitude analysis in §5.1 shows that the net Lagrangian effect is zero to $O(A^2)$. The same dependence on A also applies to all cases, despite the differences in their qualitative features. Moreover, given the fact that the quadratic scaling shown in Fig. 5.6,

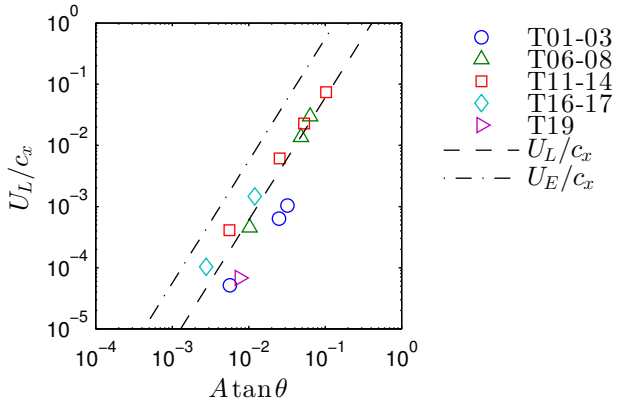

Figure 5.6: Quadratic scaling $U_L/c_x \propto (A\tan\theta)^2$ of Lagrangian mean drift velocity scale U_L. Dash line is the quadratic fit for all data points of U_L/c_x against $A\tan\theta$; dash-dot line is for the theoretical scaling of the vertical rms Eulerian mean flow $U_E = 4\sqrt{2}\pi^2(A\tan\theta)^2$ (for a plane wave, see more in Appendix A).

i.e., $U_L/c_x \propto (A\tan\theta)^2$, collapses the data points from different θ's quite well, it is very likely the same $A\tan\theta$ parameter (which has scaled the Eulerian mean successfully) can also be applicable to scale the mean Lagrangian flows, in addition to scaling the Eulerian mean. It can be shown (in §4.1) that $A\tan\theta$, up to a factor of 2π, is the ratio between the horizontal particle velocity scale U_0 and the horizontal phase speed c_x in a freely-propagating wave, offering an alternative perspective to describe the wave's nonlinearity. However, as evidenced by the vertical offset of almost one decade between the two different scalings in Fig. 5.6, the magnitude of rms Lagrangian drift U_L is significantly smaller than its counterpart U_E, the vertical rms velocity of the Eulerian mean flows, at a given $A\tan\theta$.

5.2.4 Dispersion

As mentioned earlier, the net Lagrangian effect due to reflecting IW (at a given x position) is mainly horizontally dispersion rather than driving a unidirectional

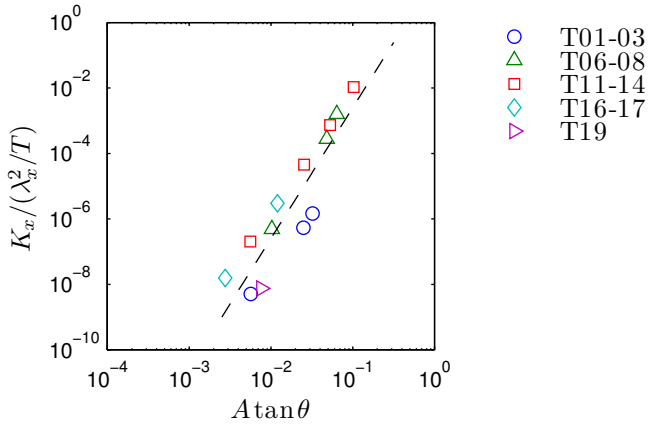

Figure 5.7: Quartic scaling $K_x/(\lambda_x^2/T) \propto (A\tan\theta)^4$ of dispersion coefficient K_x within a reflecting IW beam. Dash line represents power law $\propto (A\tan\theta)^4$.

drift. Here one can further quantify the wave-induced particle dispersion by scaling the horizontal dispersion coefficient, K_x, as in

$$\sigma^2 = 2K_x\Delta t, \tag{5.1}$$

where σ^2 is the variance of particle displacements after time Δt, which, in the context of a wave, can be taken as one or multiple of the wave period(s). Based on previous results on the scaling of the drift velocity scale $U_L \sim O(A^2)$, one would expect that

$$K_x = \frac{\sigma^2}{2\Delta t} \sim \frac{(U_L T)^2}{T} \sim U_L^2 T \propto A^4. \tag{5.2}$$

Here the expectation that K_x is of $O(A^4)$ is verified by examining the particle tracking results. First, the variance of the net displacements of q particles initiated at a given (x_0^+, z_0^+) position after five periods can be calculated; then, an ensemble average of the point-wise σ^2's based on p^2 initial locations can be computed for each wave configuration; and finally K_x can be estimated by (5.1) with $\Delta t = 5T$. The dispersion coefficients so computed are shown in Fig. 5.7. A clear quartic scaling of K_x against A can be observed, which is expected from (5.2); the same $A\tan\theta$

parameter collapses all wave cases reasonably well. Again, the quartic scaling of dispersion is a direct implication of the wave-mean Lagrangian mean flow U_L being $O(A^2)$, leading the dispersivity K_x, which is quadratic in U_L (see (5.2)), to take effect on $O(A^4)$.

5.3 Discussion

The discussion here concerns the seemingly inconsistent results from small-amplitude analysis and numerical particle tracking: The analysis in §5.1 shows that the Eulerian mean flow due to wave-wave interaction and wave-induced Stokes drift cancel each other out to $O(A^2)$; however, particle tracking does reveal the existence of $O(A^2)$ net drifts. In fact, the two sets of results are complementary to each other; as pointed out in §5.2, the analytical result of Euler-Stokes cancellation is partially supported by its numerical counterpart, given that the net drift $\langle u^+ \rangle \sim U_L$ observed in the latter is approximately one order of magnitude smaller than it would have been if the Eulerian mean flow $\langle u \rangle$ were acting alone. Interestingly, a similar observation of local Euler-Stokes cancellation has also been reported for traveling surface waves in the laboratory (Monismith *et al.*, 2007). The implication here is along the same lines as Monismith and Fong (2004): To predict mass transport in a wavy flow strictly based on a Eulerian mean is often unreliable when other wave-induced effects, such as Stokes drift, can act in conjunction. A more accurate prediction for IW-driven transport would require the understanding of the combined action of Eulerian mean and Stokes drift — in our case, the (near) cancellation of each other.

On the other hand, as numerical particle tracking suggests, the cancellation of

the two competing nonlinear effects to $O(A^2)$ is not complete, as the residual drifts are evidently still of second order. In the analysis, small-amplitude approximations have been used and inviscid solutions (Tabaei *et al.*, 2005; Thorpe, 1987; LeBlond and Mysak, 1978) have been adopted to approximate the Stokes drift, whereas the simulation results are fully nonlinear and viscous. Therefore, the discrepancy may either be a large-amplitude or viscous effect. On one hand, it is not very likely that the small-amplitude approximation is causing the discrepancy between analysis and numerical, as the $O(A^2)$-scaling of the residual drift holds consistently well even for the relatively smaller amplitudes studied (see Fig. 5.6). On the other, a more plausible explanation seems to be that the flow structure (either primary wave or Eulerian mean) in a DNS is also subject to viscous/diffusive effects, the role of which has been discussed for a freely-propagating IW beam (Thomas and Stevenson, 1972) and linear reflection of IWs (Kistovich and Chashechkin, 1995). These effects, e.g., possible viscous modifications to the inviscid velocity field (B.15), can cause subtle changes to the nonlinear dynamics which are not accounted for in the inviscid analysis. A more complete theory for the Lagrangian flow would require considerations of these viscous/diffusive effects; however, the existing theories for nonlinear reflections, either for plane IW (Thorpe, 1987) or IW beam (Tabaei *et al.*, 2005), are limited to inviscid formulations. As a result, it remains an open question as to how the observed residual $O(A^2)$ mean Lagrangian flow comes about. A theoretical analysis for nonlinear reflection augmented to account for viscous effects may provide further insights on this matter.

Another interesting fact is that at a higher value of θ, the higher harmonics generated upon beam reflection may become a propagating mode which can be considerably energetic (Tabaei *et al.*, 2005). For example, in cases 11–14, the second harmonic is indeed present and appears on $O(A^2)$ (Zhou and Diamessis,

2013). A natural speculation might be that the higher harmonics may cause the stronger drifts that are observed for these cases. However, this mechanism is not supported by the scaling arguments. Recall that Stokes drift due to $O(A^n)$ dynamics can take place at best at $O(A^{n+1})$ (see in Appendix B.2); specifically, the $O(A^2)$ harmonic with frequency 2ω is expected to generate net Lagrangian effects at $O(A^3)$ or higher. Since the drifts are observed to be on $O(A^2)$ for all cases including 11–14, it cannot be exclusively a harmonic effect.

Bühler *et al.* (2013) convected particles in a three-dimensional near-inertial wave field and reported stronger dispersion at second order in wave amplitude, contrary to the fourth-order dispersion reported in this study. This stronger dispersion observed was attributed to weak damping of the waves. The discrepancy in the observed diffusivity (or dispersion coefficient) might be due to the inherent difference in the wave set-ups, i.e., Bühler *et al.* (2013) studied random waves at near-inertial scales forced by white noise, whereas the present study concerns a deterministic quasi-monochromatic internal wave beam free of rotation. It is worth noting that, despite these differences in the set-ups, the driving mechanism of the observed particle dispersion among the two studies, does seem to be a common one, i.e., the viscous damping undergone by these waves.

CHAPTER 6

TURBULENCE-EMITTED INTERNAL WAVES AT THE SEA SURFACE

6.1 Model formulation

6.1.1 Numerical set-up

The data sets of stratified turbulent wakes and the far-field evolution of the wake-emitted internal waves are generated numerically by a highly scalable parallel spectral multidomain penalty incompressible Navier-Stokes solver developed by Diamessis *et al.* (2005). This flow solver has been used to investigate stratified wake by Diamessis *et al.* (2011) (hereinafter referred to as DSD) and the wake-emitted IWs in the near-field by A&D. Critical to the suitability of this solver to the present study is its spatial discretization: Fourier in the horizontal and Legendre multidomain penalty-based subdomains in the vertical, which allows one to attain high resolution in particular vertically localized flow regions of interest. Such vertical discretization also enables flexibility in choosing boundary conditions in the top and bottom boundaries. Spectral filtering and a penalty scheme provide the numerical stability needed for simulating the larger scales of high Re flow without having to resolve the full spectrum of turbulent motions.

6.1.2 Problem geometry

The flow configuration (see Fig. 6.1) and the implementation of numerical methods are almost identical to those of DSD to which readers interested in the details are

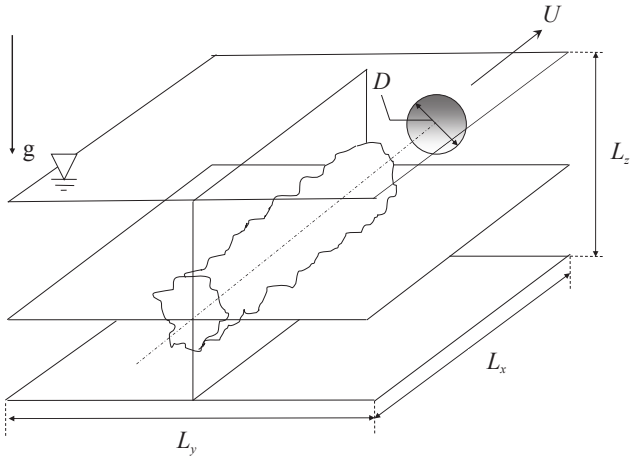

Figure 6.1: Computational domain for implicit large-eddy simulation of a temporally evolving, stratified towed-sphere wake (Diamessis *et al.*, 2005, 2011; Abdilghanie and Diamessis, 2013). The wake centreline is at $(y, z) = (0, 0)$. Sphere is towed in x, which is the only statistically homogeneous direction in the set-up. The effect of the towed sphere is not computed explicitly but rather introduced as a complex two-stage turbulent wake initialization procedure (Diamessis *et al.*, 2011). The wave sponge layer (Abdilghanie, 2010) operates on the bottom and lateral boundaries, and the top boundary is a free-slip rigid lid.

referred. Here the necessary modifications applied to the DSD set-up for the purpose of pursuing the objectives of the present study are summarized:

1. *Domain dimensions.* The computational domain of dimensions $L_x \times L_y \times L_z$ is made taller and wider (see dimensions in Table 6.1) than DSD's, to provide more space in the wake ambient for the radiated IWs to evolve and reflect off the top boundary, i.e., the model sea surface, over a sufficiently wide spanwise extent. The wake centreline, corresponding to $(y, z) = (0, 0)$, is always located at a distance of $9D$ below the top boundary. As a result, *the model sea surface is at a fixed vertical distance above the wake centreline in all simulations.*

2. *Wave sponge layers.* A&D set up sponge layers (Abdilghanie, 2010) to wrap up completely the top/bottom (xy) and lateral (xz) boundaries to prevent the IWs from re-entering the domain by reflecting or through the periodic boundaries. In the present study, however, the sponge layer on the top boundary is removed to allow the IWs to reflect from the model sea surface (see in Fig. 6.2).

3. *Boundary conditions.* Similar to DSD, periodic boundary conditions are employed in the horizontal directions. The top surface is free-slip to model the sea surface under low wind and has zero vertical gradient of density perturbation. The model sea surface is flat and non-deformable in the vertical, following scaling arguments (Moum and Smyth, 2006; Zhou and Diamessis, 2013) which predict that the surface deflections due to IWs are much smaller than horizontal length scales of the waves, and hence the surface slope is negligible.

4. *Vertical resolution.* Utilizing the spatial adaptivity of the spatial discretization in the vertical, the subdomain deployment focuses on both the turbulent wake core and the IW-reflecting subsurface zone in order for them to be resolved adequately.

6.1.3 Summary of numerical simulations

The six simulations performed for the present study have the same wake parameter space investigated in DSD, i.e., $Re \in \{5 \times 10^3, 10^5\}$ and $Fr \in \{4, 16, 64\}$. A summary of these simulations is in Table 6.1. Hereinafter, each simulation will be labeled as RaFb, where $a = Re/10^3$ and $b = Fr$. The computational cost increases dramatically with both Re and Fr. A regridding strategy similar to that of DSD is

Re	Fr	$L_x \times L_y \times L_z$	$N_x \times N_y \times N_z$	N_p	Wall-clock time (hrs)
5×10^3	4	$(80/3)D \times 40D \times 15D$	$256 \times 384 \times 341$	64	12
5×10^3	16	$(80/3)D \times 40D \times 15D$	$256 \times 384 \times 341$	64	17
5×10^3	64	$(80/3)D \times (160/3)D \times 17D$	$256 \times 512 \times 361$	64	36
10^5	4	$(80/3)D \times 40D \times 15D$	$512 \times 768 \times 851$	256	311
10^5	16	$(80/3)D \times 40D \times 15D$	$512 \times 768 \times 851$	256	614
10^5	64	$(80/3)D \times (160/3)D \times 17D$	$512 \times 1024 \times 919$	256	1755

Table 6.1: Summary of numerical simulations of stratified wakes at $Re \in \{5 \times 10^3, 10^5\}$ and $Fr \in \{4, 16, 64\}$. $N_x \times N_y \times N_z$ is the number of grid points; N_p is the number of MPI processors used.

applied to R100F64 in the lateral direction y whenever the half-width of the wake L_H exceeds 10% of the width of the domain.

6.2 Basic phenomenology

The basic physical process involving turbulence-emitted internal waves and their surface reflection is described in this section, aided by flow snapshots extracted from the simulations shown in Figs. 6.2 and 6.3. Fig. 6.2 shows typical span-vertical (yz) transects of the flow field sampled at the centerplane of the computational domain at $x = 0$. The horizontal divergence Δ_z field is used to visualize the internal wave motions (Abdilghanie and Diamessis, 2013; Spedding, 2014) in the ambient of the turbulent wake core which is centerd at $(y, z) = (0, 0)$. Three snapshots are shown in Fig. 6.2 to illustrate the process of internal wave radiation from the wake core and wave propagation in the far-field. At early times, e.g., at $Nt = 10$, and in the ambient of the wake core, one can observe an internal phase configuration that is comparable to the classical St Andrews cross pattern observed around an oscillatory wave source (Mowbray and Rarity, 1967). As expected, when

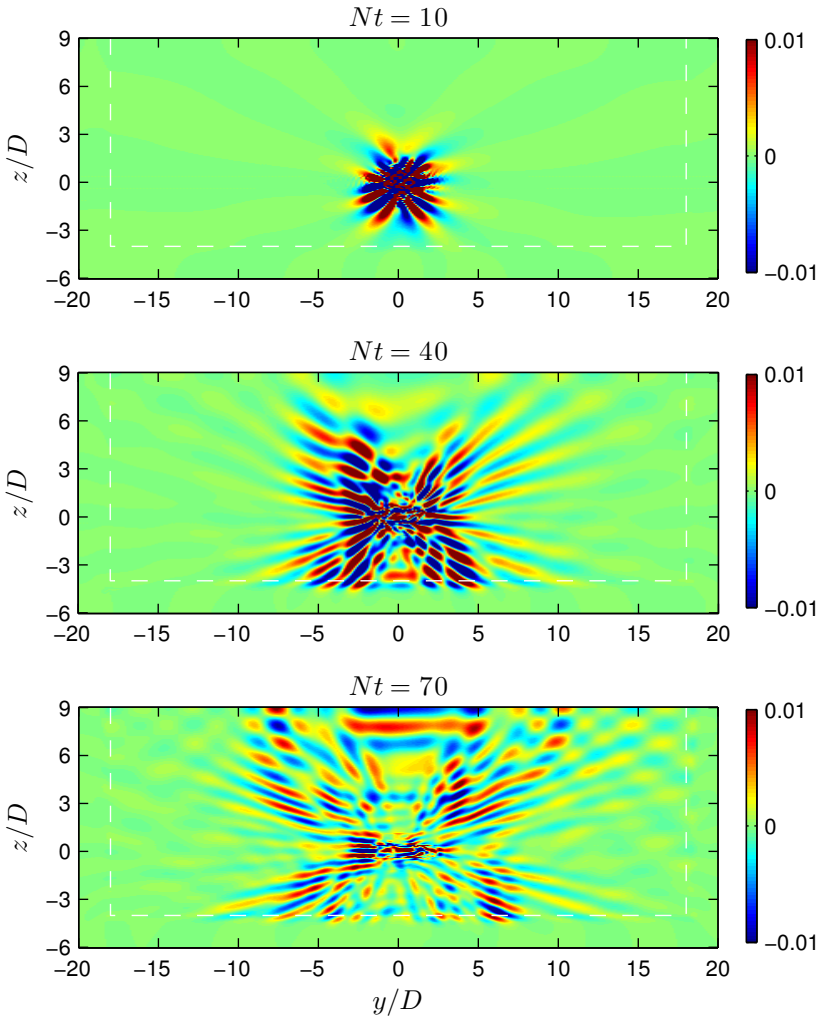

Figure 6.2: Horizontal divergence Δ_z (normalized by buoyancy frequency N) fields sampled at Oyz centerplane at various times (marked on top of the color maps) at $Re = 5 \times 10^3$ and $Fr = 4$ (R5F4). The interface between the fluid and wave-absorbing virtual sponge layer is marked by white dash lines.

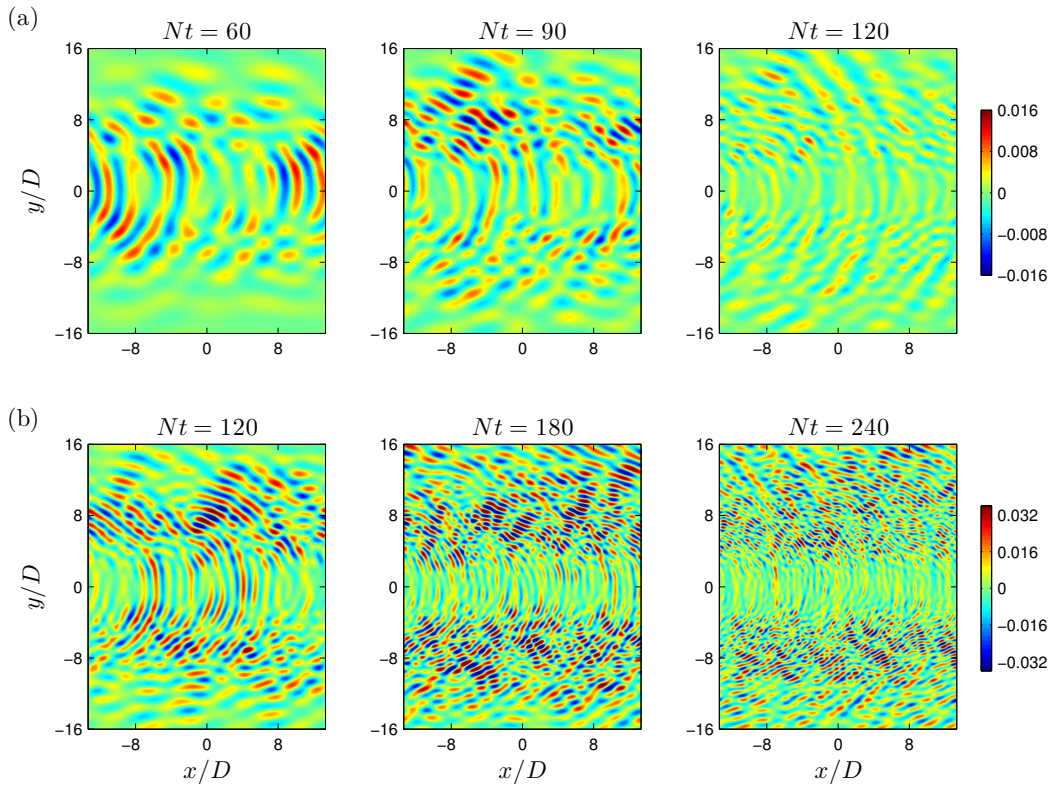

Figure 6.3: Horizontal divergence Δ_z (normalized by buoyancy frequency N) field at the model sea surface at (a) R5F4 and (b) R100F4 respectively. Time is from left to right with Nt value marked on top of the color maps.

the waves propagate further into the far-field, the iso-phase lines grow their extent in directions of the outwardly oriented group velocities, which can be seen in the snapshot at $Nt = 40$. As the waves propagate even further (shown in the snapshot at $Nt = 70$), they visibly reach the model sea surface at $z = 9D$ off which they reflect.

Of interest to a remote observer are the waves' spatial and temporal characteristics on the sea surface. Fig. 6.3 shows the spatial patterns which these turbulence-emitted internal waves form as they reflect at the model sea surface, i.e., the topmost xy plane of the computational domain. Snapshots of the Δ_z field

are shown at both Re's at $Fr = 4$. First, these waves spread broadly in the span of the flow (i.e., in y) on the sea surface and exhibit coherent spatial patterns. These spatial patterns are also persistent in time, i.e., they last for $O(10)$ to $O(100)$ units of buoyancy time scale $1/N$. Second, the length scale of the waves varies strongly in time, i.e., the waves are observed to be finer in scale at later Nt's, which holds at both Re's. Third, distinct directionality associated with the wave patterns can be observed on the horizontal plane, i.e., the direction of the iso-phase lines with respect to the x-axis (the streamwise direction) varies with the spanwise offset in y. These key features of the surface-observed internal-wave signatures will be characterized in greater detail in §6.3. Specifically, the time evolution of surface-observed wave strain amplitude is discussed in §6.3.1. The length scales of the waves will be measured and parametrized with wake parameters (Re, Fr) and dimensionless time Nt in §6.3.2, and the wave periods are reported in §6.3.3. The directionality of the wave signatures on the sea surface, i.e., the azimuthal angle formed by these wave patterns with the streamwise direction x, is discussed in §6.3.4.

6.3 Wave characteristics at the sea surface

6.3.1 Arrival time of peak wave impact

It is of interest to first identify the dimensionless time, Nt, elapsed since the passage of the generating body, at which the most energetic waves arrive at the surface. Moreover, one seeks to determine how this arrival time of peak wave impact changes over the wake parameter space (Re, Fr). To this end, a model will be developed based on linear internal wave theory and verified by numerical simulations.

One can apply linear internal wave theory (Sutherland, 2010) to estimate the time for an internal wave to propagate from z_0 to z, which can be written as:

$$t - t_0 = \frac{z - z_0}{c_{g,z}} = \frac{z - z_0}{\frac{N}{2\pi/\lambda_H} \sin\theta \cos^2\theta}, \tag{6.1}$$

where (z_0, t_0) can be considered as the vertical location and time from and at which the waves are emitted, i.e., the *virtual origin* of the waves. Additionally, λ_H is the horizontal wavelength, and θ is the angle between the wave's group velocity and the vertical direction.

The critical time $\hat{t}$ at which the surface undergoes the peak wave impact can be considered as the time at which waves of wavelength $\hat{\lambda}_H$, the most energetic wavelength, arrive at the surface. Noting that the surface is located at $z = 9D$ in all simulations and assuming that in the far-field of the wake, $\hat{t} \gg t_0$, i.e., the waves are emitted at a considerably early t_0 and it takes a considerable amount of time for a wave to propagate in space to reach the observation plane, one can apply (6.1) for waves of wavelength $\hat{\lambda}_H$ arriving at the surface at $\hat{t}$ and obtain

$$N\hat{t} \approx \frac{2\pi}{\sin\theta \cos^2\theta} (\frac{9D - z_0}{D})(\frac{\hat{\lambda}_H}{D})^{-1}. \tag{6.2}$$

It is found in §6.3.2 that

$$\hat{\lambda}_H / D \propto Fr^{1/3}, \tag{6.3}$$

i.e., the most energetic wavelength scales as $Fr^{1/3}$, and in §6.3.2 that the virtual origin z_0 can be considered as a constant across all simulations. Moreover, the dependence of θ in Fr is found to be rather weak (see §6.3.3 for more details). As a result, one can deduce from (6.2) that

$$N\hat{t} \propto Fr^{-1/3}, \tag{6.4}$$

which predicts that the peak arrival time in Nt scales as $Fr^{-1/3}$.

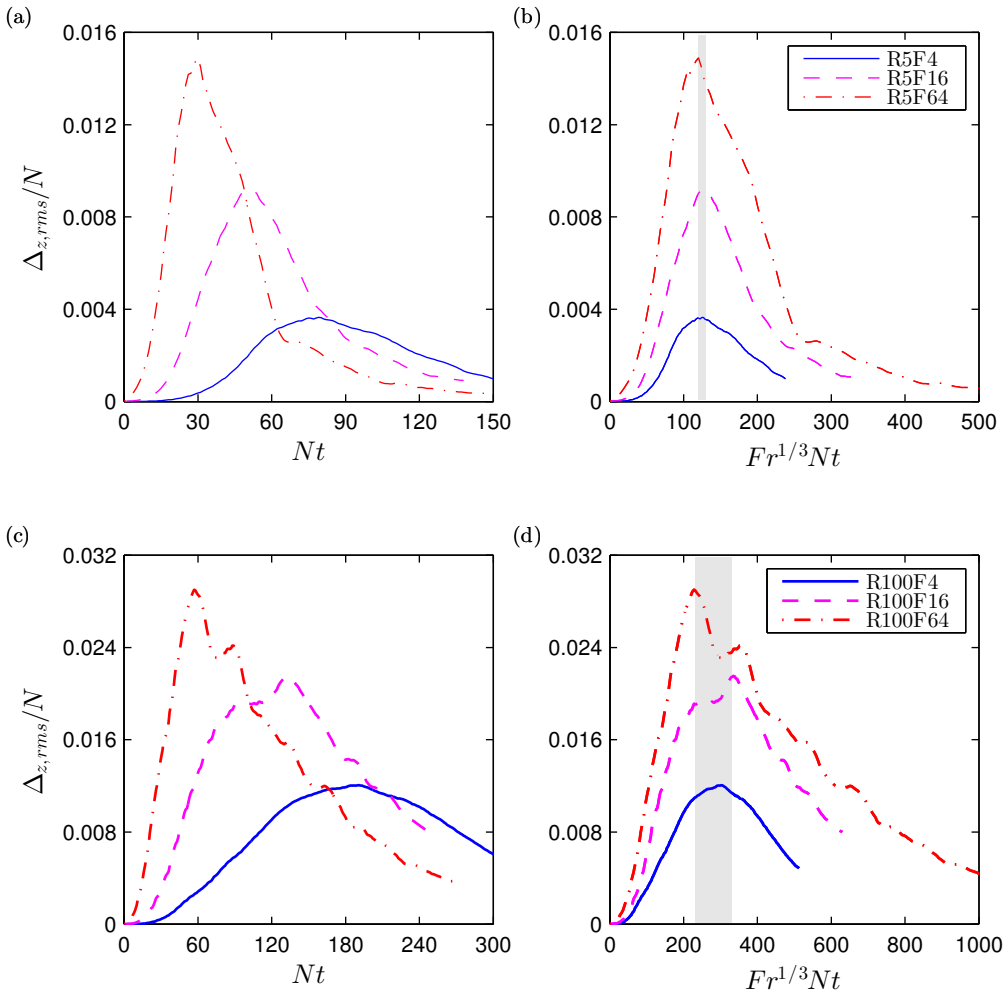

Figure 6.4: Time series of surface rms horizontal divergence $\Delta_{z,rms}$ normalized by the buoyancy frequency N: (a)(b) at $Re = 5 \times 10^3$ and (c)(d) at $Re = 10^5$. The peak wave amplitude occurs at a narrow range of $Fr^{1/3}Nt$ for each Re, as marked by the shaded area in (b)(d).

To verify (6.4), time series of the spatial rms amplitudes of horizontal divergence Δ_z over the entire surface (a quantity denoted by $\Delta_{z,rms}$) are computed for all simulations as a measure of wave-induced strain. The $\Delta_{z,rms}$ amplitude is normalized by N, which forms a dimensionless measure of the waves' steepness (A&D) and bears implications for the visibility of these waves (see §6.4.2). The results are shown in Fig. 6.4, depicting the time evolution of the surface-observed

wave strain amplitude. A delay of peak arrival time in Nt with decreasing Fr can be observed at both Re's. When the horizontal axis Nt is rescaled by a factor of $Fr^{1/3}$, the peak arrival times collapse into a considerably narrow range of $Fr^{1/3}Nt$ values, i.e., $[120, 130]$ at $Re = 5 \times 10^3$ and $[230, 330]$ at $Re = 10^5$, as highlighted by the shaded areas in Fig. 6.4(b)(d). This collapse implies that the arrival time of peak wave impact at the surface in terms of Nt scales approximately as $Fr^{-1/3}$ at a given Re, which is consistent with (6.4), a prediction due to linear wave theory.

One would be equally interested in the downstream distance from the towed sphere $\hat{X}/D$ at which the strongest waves arrive at the surface. Noting that the conversion from Nt to X/D involves a linear factor of $Fr/2$ as in (1.2), one can obtain from (6.4) that

$$\frac{\hat{X}}{D} = \frac{Fr}{2} N\hat{t} \propto Fr^{2/3}, \tag{6.5}$$

which implies that the peak wave strains arrive at a shorter downstream distance normalized by the sphere diameter X/D (which however corresponds to a later dimensionless time in buoyancy units, i.e., Nt) at a lower Fr.

On the other hand, while the time (or distance) to peak wave impact at the surface can be modelled using simple kinematic arguments of internal waves, it is inconclusive as to how the peak wave magnitude itself scales with Fr, although an increase of Δ_z/N with Fr can clearly be observed. The waves emitted by the higher-Re wakes are also recorded to have higher amplitude when arriving at the surface. Similar observations for the amplitudes have also been reported in the wake's near-field (Abdilghanie, 2010). The detailed mechanism by which the waves extract momentum and energy from the turbulence, would shed light on how the energy content of the outgoing waves vary with (Re, Fr). This mechanism has not been known completely and is deferred to further study focusing on turbulence-

wave interaction in the wake's near-field.

In this subsection, the time evolution of the surface-observed wave amplitude has been examined. A key ingredient of the model for the time (or distance) to peak wave impact is *the scaling of the most energetic wavelength*, i.e., (6.3); in the following subsection, the analyses on the length scales of these waves are presented.

6.3.2 Wavelength

Analysis procedure

The two-dimensional wavelet transform is applied to the surface $\Delta_z(x, y)$ field to interrogate the length scales of the wave signatures. This wavelet approach has been proven useful in analyzing the quasi-random and spatially localized internal wave field emitted by a turbulent source (Abdilghanie, 2010; Abdilghanie and Diamessis, 2013). Specifically, a complex two-dimensional localized basis function (or mother wavelet) "Arc" (Dallard and Spedding, 1993) is used to extract wave patterns of a specific length scale regardless of their spatial orientations (the latter is discussed separately in §6.3.4). The analysis procedure is outlined below:

1. *Wavelet transform.* At a given Nt, the two-dimensional mother wavelet corresponding to a wavelength λ_H is applied to the surface strain field characterized by $\Delta_z(x, y)$. As the mother wavelet translates in space, the transform modulus is recorded as a function of (x, y); by varying the length scale λ_H, the modulus forms a three-dimensional cube in the $(x/D, y/D, \lambda_H/D)$ space. The same exercise is repeated for all Nt's, and the modulus is stored as a function of $(x/D, y/D, \lambda_H/D, Nt)$ to describe the entire internal-wave man-

ifestation process on the sea surface.

2. *Extraction of wave events.* A higher value of transform modulus at a given point in space is indicative of local resonance of the wave strain field with the mother wavelet and thus the existence of a wave packet of the specific spatial scale. By applying a threshold (here 45% of global maximum transform modulus across all Nt's is used) to the modulus data, a large number of resonance events can be isolated in the $(x/D, y/D, \lambda_H/D, Nt)$ sample space. Note that x is a homogeneous direction in the numerical set-up; no wave statistics are expected to vary in x and thus any x-dependence is ignored. After "collapsing" the four-dimensional data set in x, a large number of wave events are now extracted in the three-dimensional sample space formed by $(y/D, \lambda_H/D, Nt)$. These wave events carry information about the statistical characteristics of the internal wave packets that appear on the sea surface. In the following, we show these statistics, such as the joint probability density functions (PDFs) of the wave packets. Note that in order to extract these wave events from the sample space, a threshold value is to be specified on the quantity which serves as an indicator of the wave amplitude. When specifying the threshold, one is to exclude the less energetic events by specifying a relatively high threshold, and on the other hand, to maintain a large enough sample population to construct the PDFs by using a relatively low threshold – a balance between the two factors, where only considerably energetic events are extracted in a large enough population, is desirable. This general guideline is followed to produce the results presented in §6.3.2, §6.3.3 and §6.3.4 respectively, when the threshold for wave event extraction is selected.

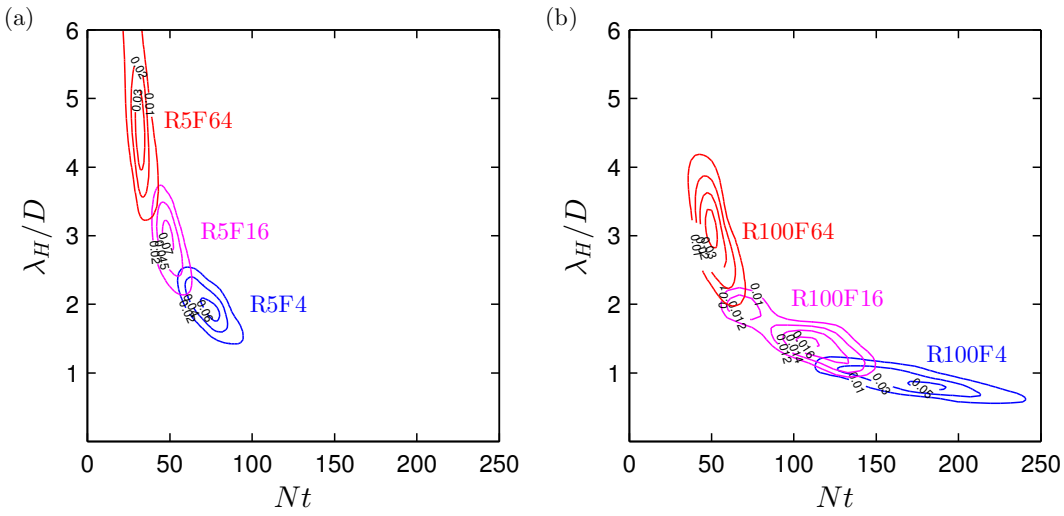

Figure 6.5: Joint probability density contours of most energetic wave packets in the $(\lambda_H/D, Nt)$ sample space at (a) $Re = 5 \times 10^3$ and (b) $Re = 10^5$ respectively for $Fr \in \{4, 16, 64\}$.

Joint distribution of wave events in wavelength-time space

Since the variation of the wavelengths λ_H corresponding to the most energetic wave packets is found to be much weaker in the spanwise direction y (not shown) than the variation in Nt, one can proceed by also collapsing the data in y/D as well and focus on the evolution of length scale λ_H in time. The joint PDF of these wave events constructed in the $(\lambda_H/D, Nt)$ space is shown in Fig. 6.5. In agreement with Fig. 6.4, at a given Re, energetic packets with the most frequently occurring wavelength reach the surface at a later Nt as Fr is reduced. At the higher Re, the arrival time of the most frequently occurring wavelength is shifted in time towards a later Nt. The joint PDFs appear to lie along a universal line, with the centers of the PDF contours varying as a function of (Re, Fr). In §6.3.2, the universal trend in which the prevalent wavelength λ_H evolves with Nt, characterized by the evolution of the conditionally averaged wavelength $\overline{\lambda}_H$ at each time, will be further discussed; in §6.3.2, the most energetic wavelength $\hat{\lambda}_H$, i.e., the wavelength

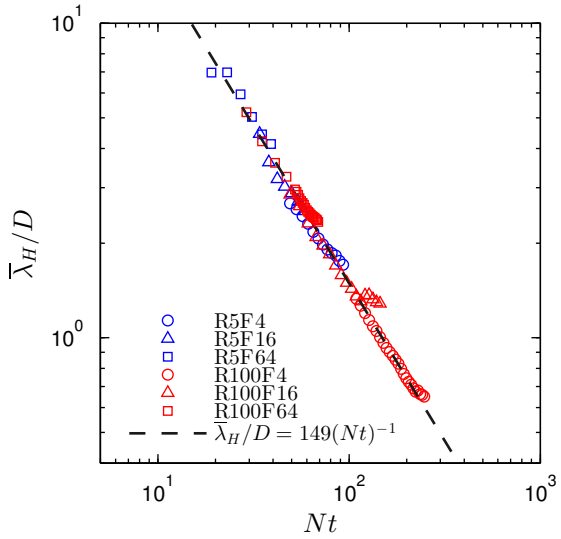

Figure 6.6: Time series of conditionally averaged wavelengths $\overline{\lambda}_H/D$ observed at the sea surface. Best fit to the linear propagation model (6.7) is shown as dash line.

λ_H corresponding to the peaks of the joint PDFs, will be parametrized by the wake's Re and Fr.

Evolution of mean observable wavelengths

Fig. 6.6 shows the conditional mean IW horizontal wavelength, $\overline{\lambda}_H$, as a function of Nt for all simulations. $\overline{\lambda}_H$ is the mean λ_H computed based on the wave events extracted in the $(\lambda_H/D, y/D)$ sample space at a given Nt [see §6.3.2(b)]. For the range of Nt values at which a significant probability density is present (Fig. 6.5), the time evolution of $\overline{\lambda}_H$ in Nt seems to follow a universal line across all simulations covering the wake parameter (Re, Fr). The decay of $\overline{\lambda}_H$ in Nt follows a power law of $(Nt)^{-1}$ which is consistent with the laboratory experiments and analysis by Bonneton *et al.* (1993) and Spedding *et al.* (2000). This observation motivates the linear wave model that is to be constructed and calibrated below.

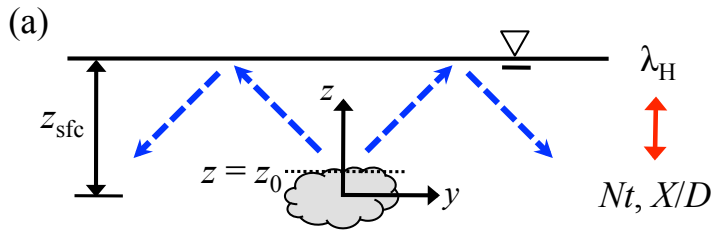

Figure 6.7: Schematic of key concepts associated with linear wave model (6.7) evaluated at the sea surface ($z = z_{\text{sfc}}$). Internal waves (dash arrows) of various wavelengths λ_H are observed at the surface as if they had been emitted from the virtual origin z_0 at $t_0 \ll t$. (6.7) relates the surface observed λ_H to the submerged turbulence characterized by the dimensionless time Nt and the corresponding dimensionless distance X/D to the wake-generating body as in (1.2).

One may consider the linear propagation of internal waves and rewrite (6.1) as

$$\frac{\lambda_H}{D} = \frac{z - z_0}{D} \frac{2\pi}{\sin\theta \cos^2\theta} \frac{1}{N(t - t_0)}. \tag{6.6}$$

Again, consider the wake's far-field and invoke the far-field condition $t \gg t_0$:

$$\frac{\lambda_H}{D} \approx \frac{z - z_0}{D} \frac{2\pi}{\sin\theta \cos^2\theta} \frac{1}{Nt}. \tag{6.7}$$

Hence the power-law $(Nt)^{-1}$ is recovered in (6.7), in agreement with the observations shown in Fig. 6.6 and experiments (Bonneton *et al.*, 1993; Spedding *et al.*, 2000). The effectiveness of linear theory here indicates that *these internal waves emitted by turbulence act in the far-field as linear waves*, at least within the parameter range and uniform stratification examined here. The key physical process driving the time evolution of wavelength at the surface is the waves' *dispersion*, i.e., waves of greater wavelength propagate faster and thus arrive at the observation plane at an early Nt, and vice versa.

The linear propagation model in (6.7) can be applied specifically at the sea surface located at $z = z_{\text{sfc}}$, where z_{sfc} is the depth of the wake centreline below the

surface (Fig. 6.7). It is desirable to first complete the linear propagation model in (6.7) by calibrating the *virtual origin* z_0 of the waves based on the observations at $z_{\text{sfc}}/D = 9$ in our simulations. Note that the intended applicability of the model and the calibration parameter z_0 is restricted to the wake's far-field for which $(z,t) \gg (z_0,t_0)$, and to when the waves are indeed linear and given enough room to disperse when they arrive at the vertical location z. In the wake's near-field, however, the waves' interaction with turbulence is possibly nonlinear (Sutherland and Linden, 1998), and the waves are not fully dispersed in space, being close to the turbulent source. Therefore, the model (6.7) and any fitting parameter are not expected to give a reliable description of the waves in the near-field; in fact, A&D reported a power-law decay of $\overline{\lambda}_H$ in Nt with exponents different from -1 based on near-field sampling of these waves.

In order to calibrate z_0 for the the model (6.7), a least squares fit can be applied to the data points in Fig. 6.6 contributed by all simulations. The best fit to the data following (6.7) is found to be (with 95% confidence level):

$$\frac{\lambda_H}{D} = \frac{149 \pm 2}{Nt}, \tag{6.8}$$

based on observations at a sea surface located at $z/D = 9$. By substituting $\theta = 45°$, a characteristic prevalent wave emission angle reported by A&D, into (6.7), and utilizing the fit in (6.8), the *virtual* origin (based on observations in the *far-field*) is found to be

$$\frac{z_0}{D} = 0.62 \pm 0.11. \tag{6.9}$$

z_0, a calibration parameter for the far-field linear wave model (6.7), is not to bear implications for the local dynamics at $z = z_0$ in the wake's near-field, but completes the model (6.7) which enables the prediction of wavelength in the far-field. As such, z_0 should not be confused with the location of the wake edge, itself a function of

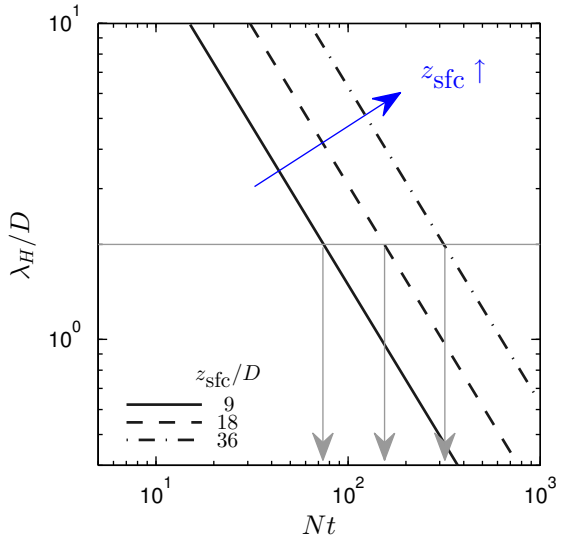

Figure 6.8: Time evolution of λ_H/D in Nt for various wake depths, $z_{\mathrm{sfc}}/D \in [9, 18, 36]$, as predicted by (6.7) using the calibrated virtual origin $z_0/D = 0.62$ for waves propagating at $\theta = 45°$ to the vertical. A given λ_H/D observed at the surface (marked by the horizontal gray line) may correspond to different Nt values (where the vertical gray arrows point at, for each z_{sfc}/D considered in the figure) of the submerged turbulence which may be located at various depths.

Fr (Fig. 7 of DSD).

Application of the linear model

As sketched in Fig. 6.7, the specific application of linear model (6.7) that is of interest is to connect surface observations of λ_H/D at a given point in time, with the information associated with the submerged turbulence, such the dimensionless time Nt elapsed since the passage of the object, and/or the dimensionless distance X/D to the object. Note that the evolution of wavelength in space and time $(z/D, Nt)$ specified by (6.7) is independent of the wake parameters (Re, Fr), therefore knowing these parameters *a priori* may not be a prerequisite for the con-

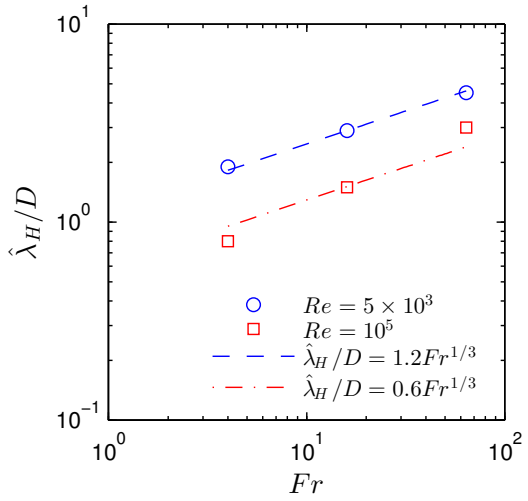

Figure 6.9: Fr- and Re-dependence of the most energetic wavelength $\hat{\lambda}_H/D$ observed at the sea surface.

nection that we would like to make. Fig. 6.8 illustrates some of the implications of (6.7): When the depth z_{sfc} and the Nt value of the submerged turbulence are both known, one can readily compute the corresponding λ_H/D to expect at the surface, with (6.7) and the calibrated z_0 in (6.9). However, inferring Nt solely from surface observations of λ_H/D is not as straightforward, because λ_H/D is not uniquely determined by Nt but rather the combination of z_{sfc}/D and Nt. One can deduce from observations of λ_H/D the combinations of z_{sfc}/D and Nt that would produce such a wavelength, but neither z_{sfc}/D nor Nt individually (see Fig. 6.8).

Selection of peak wavelength by wake turbulence

While the time evolution of the mean observable wavelength at a given $(z/D, Nt)$ is universally determined by the kinematic properties of internal waves prescribed by the linear theory, the most probable wavelength $\hat{\lambda}_H$ to be observed, i.e., the most energetic one, does depend on the parameters of the wave-emitting wake, i.e., (Re, Fr) (see Fig. 6.5). Fig. 6.9 shows the most frequently occurring wavelength

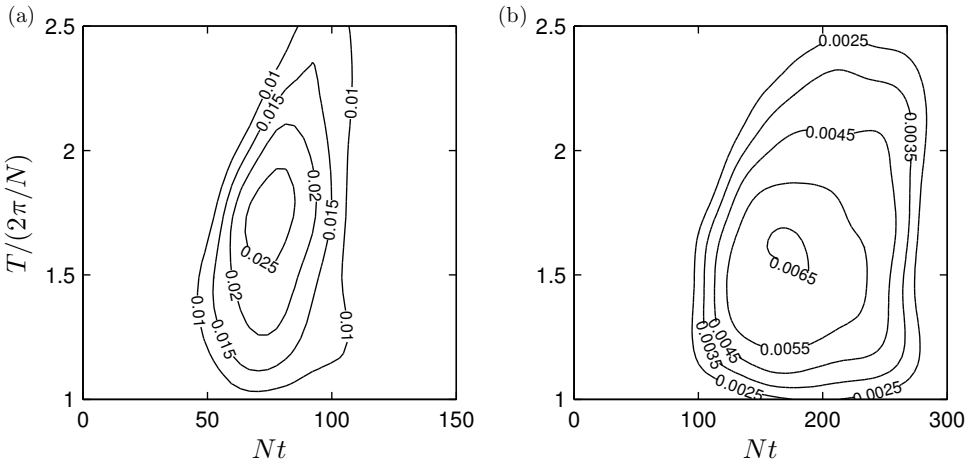

Figure 6.10: Joint probability density contours of most energetic wave packets in the $(T/(2\pi/N), Nt)$ sample space: (a) R5F4 and (b) R100F4.

identified from Fig. 6.5, corresponding to the peaks of the joint PDFs, as a function of Fr. For each value of Re, an approximate $Fr^{1/3}$ scaling can be observed for $\hat{\lambda}_H/D$, which is consistent with previous studies (Abdilghanie and Diamessis, 2013; Spedding *et al.*, 2000). A dependence on Re can also be observed: Increasing Re from 5×10^3 to 10^5 reduces $\hat{\lambda}_H$ by 50% at a given Fr. More discussion on this specific length-scale selection by wake turbulence is given in §6.5.2.

6.3.3 Wave period

Similar to the length-scale computation outlined in §6.3.2, one-dimensional wavelet transform (with the Morlet mother wavelet) has been applied to time series of horizontal divergence Δ_z signals, sampled at every grid point on the surface, to interrogate the period of these waves. One can then isolate, in a given time series of the transform modulus, the most energetic wave packets (with transform modulus above 35% of the maximum value at all Nt's for all locations) as a function of time

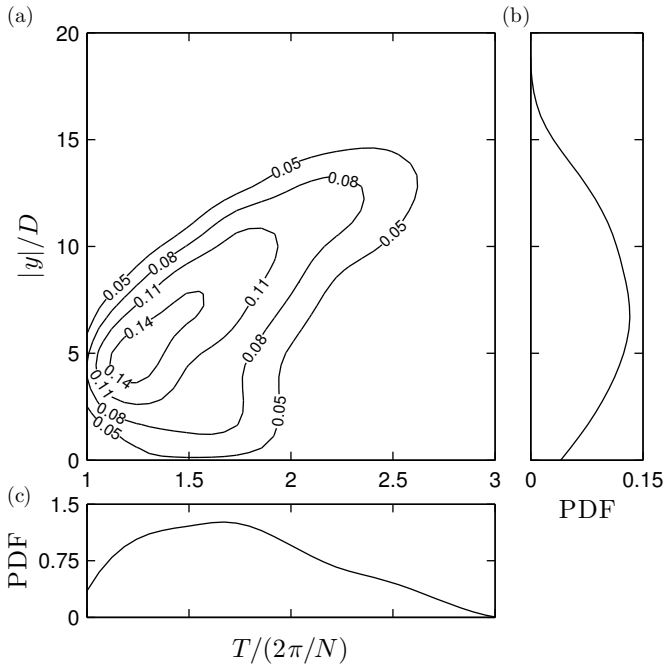

Figure 6.11: Distribution of most energetic wave packets in the $(|y|/D, T/(2\pi/N))$ sample space for $Re = 5 \times 10^3$, $Fr = 4$: (a) Probability density contours, (b) marginal PDF vs. $|y|/D$ and (c) marginal PDF vs. $T/(2\pi/N)$.

of occurrence Nt and wave period T. Again, the x-dependence is to be ignored, i.e., the data are to be collapsed in the statistically homogeneous x axis. Effectively, for each Re and Fr, in the three-dimensional sample space $(y/D, Nt, T/(2\pi/N))$, a large population of energetic wave events are sampled. One can then collapse these three-dimensional data in two ways, either along the Nt axis onto the y/D-$T/(2\pi/N)$ plane or along the T axis on the y/D-Nt plane. On each of these planes, joint PDF may be constructed, as shown in Figs. 6.10, 6.11 and 6.12 for $Fr = 4$ at the two Re's considered.

Fig. 6.10 shows the distribution of most energetic wave packets at $Fr = 4$ in $(y/D, Nt)$ sample space. Results at $Fr \in \{16, 64\}$ are qualitatively similar and thus not shown. The structure of the joint PDF indicates that, although the dominant

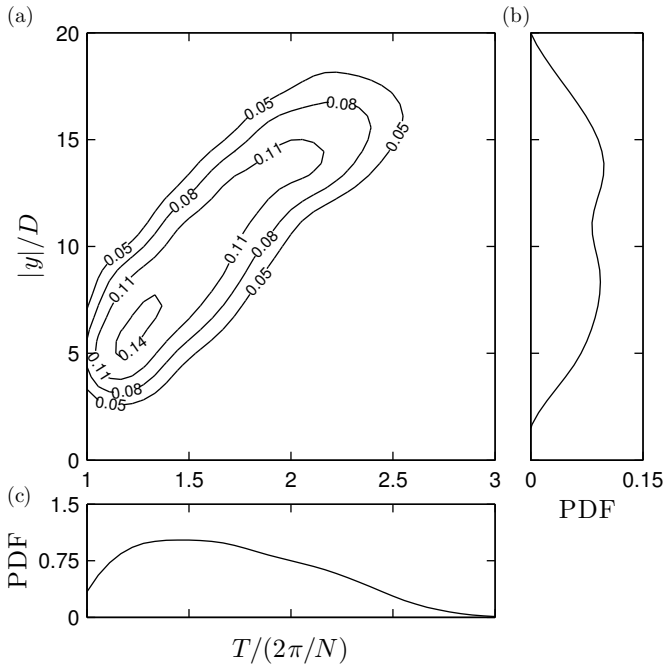

Figure 6.12: Distribution of most energetic wave packets in the $(|y|/D, T/(2\pi/N))$ sample space for $Re = 10^5$, $Fr = 4$: (a) Probability density contours, (b) marginal PDF vs. $|y|/D$ and (c) marginal PDF vs. $T/(2\pi/N)$.

period does not vary considerably as a function of Re, the most energetic wave packets arrive at a later time and over a longer window in time at the higher Re, in agreement with Fig. 6.5. Moreover, unlike the strong variation of wavelengths with Nt, the variability of wave periods reaching the surface with time is rather weak, especially after the peak wave amplitude has been reached at $Nt = 70$ and 180 for R5F4 and R100F4 respectively.

However, a strong variation of wave periods can be observed in space, specifically, in the spanwise direction y. Figs. 6.11 and 6.12 illustrate this spatial variability of wave periods and clearly show the dispersive character of the wake-radiated internal waves. Regardless of Re, the wave period reaches the peak likelihood at around 1.5 times the buoyancy period. Longer periods that are progressively

smaller in likelihood (as shown by the marginal PDFs vs. $T/(2\pi/N)$ in Figs. 6.11(c)&6.12(c)) arrive at larger spanwise offsets, as these waves have a group velocity vector that is more inclined to the horizontal, following the dispersion relation of internal waves. This distinct correlation between spanwise location y at which the waves arrive at the surface and the waves' period T, is found to be independent of Fr. At the higher Re shown at $Fr = 4$, i.e., R100F4 in Fig. 6.12(a), the y/D-$T/(2\pi/N)$ correlation is stronger as compared to the lower Re counterpart, i.e., R5F4 in Fig. 6.11(a). Moreover, at R100F4, the marginal PDF in y/D, as shown in Fig. 6.12(b), starts to decay as far as $15D$ away from the centreline, whereas at R5F4 the PDF decays immediately after it peaks at $|y| = 7D$, as shown in Fig. 6.11(b). Consequently, the waves at higher wake Re are more likely to impact larger spanwise distances from the wake centreline.

Near-field measurements of the wake-emitted waves by A&D reported one relatively narrow band of prevalent wave frequencies (and thus propagation angles) for each of the two Re's respectively. It is also reported that a selective viscous decay mechanism, similar to that proposed for waves from a turbulent bottom Ekman layer (Taylor and Sarkar, 2007), acts in the wake's near-field to further narrow down the frequency band, at the lower Reynolds number $Re = 5 \times 10^3$. In the far-field, however, the waves are in fact observed to be more broadband in the frequency domain, as these various frequencies are given enough distance to disperse when they are allowed to propagate over a greater distance into the far-field. Dispersion of these waves in the wake's lateral direction due to the variability in propagation angles widens the spatial extent in y in which the waves may manifest themselves. In light of this, one would naturally expect the waves to disperse more in space (specifically, in y), should there be a greater vertical offset from the wave source to the observation level; therefore, the degree of wave dispersion in

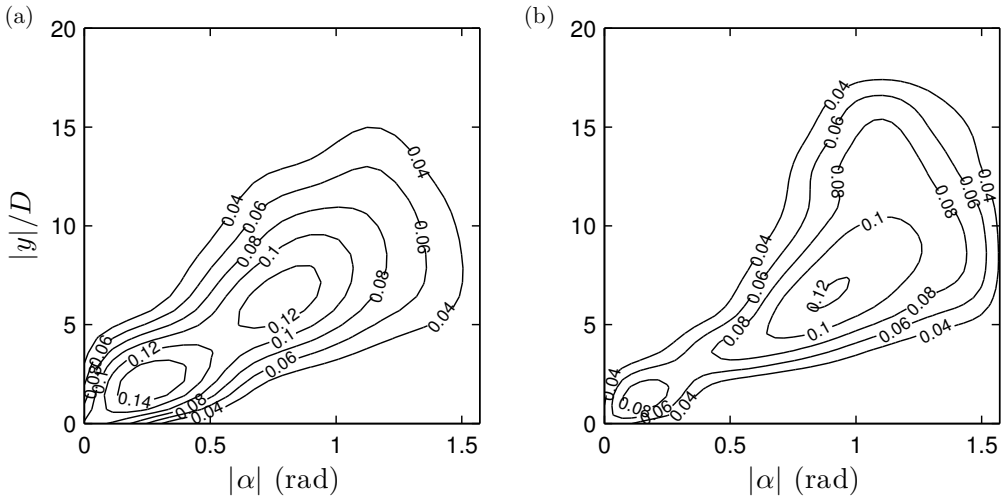

Figure 6.13: Joint probability density contours of significant wave events in the $(|y|/D, |\alpha|)$ sample space: (a) R5F4 and (b) R100F4, where α is the azimuthal angle of the dominant principal strain-rate with respect to the x axis.

the spanwise direction y (characterized by the width of wave impact in y) on the observational plane may possibly give an estimate of the depth of the turbulent source, especially when such information is not available.

6.3.4 Wave orientation

Of interest to an observer is also any preferred orientation in the wave-induced surface strain field. At any given time and at each point on the sea surface, a two-dimensional eigenvalue/vector decomposition may be applied to the surface rate-of-strain tensor due to the horizontal velocities (u, v) (note that the vertical velocity w vanishes at the rigid lid), which provides the magnitudes of the two principal strain rates and the directions of the two corresponding principal axes (PAs) on the xy plane. The dominant PA (with the higher strain-rate magnitude) tends to align perpendicular to the waves' iso-phase lines across which velocity due

to the wave varies the most rapidly. Therefore, the direction of the dominant PA gives a convenient measure of the waves' orientation at a given location on the surface. The joint PDF of the orientation (azimuthal angle α with respect to the wake axis x) of the dominant PA with strain rates exceeding a certain threshold (80% of the peak $\Delta_{z,rms}$ at all Nt's) vs. spanwise offset may then be computed, as shown in Fig. 6.13 for $Fr = 4$ at two Re's. The results at $Fr \in \{16, 64\}$ are similar and thus not shown. Two prevalent preferred directions can be identified in Fig. 6.13: One at $|\alpha| = 0.15$ to 0.25 rad (9° to 14°) which occurs closer to the wake centreline, and the other at $|\alpha| = 0.7$ to 0.8 rad (40° to 46°) at a further distance ($|y| > 5D$). At the higher Re, a noticeable protrusion of the probability density into greater distances ($|y| > 15D$) at azimuthal angle $1 < |\alpha| < 1.5$ rad can be observed. Information on location and orientation at which the IWs are most likely to reach the surface, may assist the recognition of these wave patterns from remotely acquired sea surface images.

6.4 Surface manifestation mechanisms

6.4.1 A general discussion

In this section, possible sea-surface IW manifestation mechanisms are studied. In order for the turbulence-emitted waves to self-manifest, the surface hydrodynamic condition must act in favor of one or more of the various surface modulation mechanisms of remote sensing significance (see §1.5.2). Two outstanding issues, which need to be addressed from remote sensing perspectives, are *contrast* and *spatial scales*. First, to generate enough contrast on remote sensing images to be perceivable, e.g., to create enough Bragg scattering for the features to appear on

the radar image (Alpers, 1985), or to generate surface slicks of enough thickness (Moum *et al.*, 1990), the characteristic surface strain rate, i.e., Δ_z, must exceed a certain threshold specified by the modulation mechanism. Second, the spatial scales of these surface anomalies must be small enough to fit the field of view of a certain remote sensor, and large enough compared to the sensor's resolution. As a first attempt to assess the potential remote visibility of these waves, in §6.4.2, the feasibility of generating surface slicks is examined, and in §6.4.3, wave-induced surface mass transport is discussed.

6.4.2 Wave strains and surface slicks

Model formulation

One of the most common avenues through which surface velocity strains can modulate the sea surface and create anomalies on remote sensing images (see §1.5.2) is through the organic-rich surfactant materials within the surface microlayer (Ewing, 1950b,a; Alpers, 1985; Moum *et al.*, 1990; Ermakov *et al.*, 1992; Soloviev and Lukas, 2006; Klemas, 2012). The microlayer can grow its thickness due to the accumulation of surfactant under favorable conditions, i.e., flow convergence and low mixing/dispersion due to wind. The surfactant can potentially form surface "slicks" when the thickness exceeds a certain threshold. These slicks smooth out surface capillary-gravity waves and decrease the surface reflectance to light and microwaves. As a result, the slicks appear as dark bands on optical and radar images and can possibly reveal the compressive surface strains in the surface flow. Moum *et al.* (1990) performed in-situ measurements of the surface chemistry and the subsurface hydrodynamics simultaneously at the slicks. They were able to relate the

formation of the slicks to the flow convergence and reported a 5 to 25% increase in the surfactant concentration across the slicks relative to the background.

In an attempt to predict the feasibility of slick formation under surface strains due to turbulence-radiated internal waves, simulations of the two-dimensional advection equation for the surfactant concentration are performed at the topmost free-slip surface of the computational domain (see Fig. 6.1), forced by the surface velocity field generated by the wake simulations. These auxiliary simulations of the passive scalar field employ second-order finite difference in space and fourth-order Adams-Bashforth-Moulton in time. More refined models which incorporate the diffusion/relaxation of surfactant gradients (Ermakov *et al.*, 1992) and coupling with surface wave actions (Alpers, 1985; Ermakov *et al.*, 1992) have been proposed and can be readily incorporated should the site-specific parameters involved in these models become available.

Numerical results

The surface surfactant field simulations are initialized with a uniform initial scalar concentration Γ_0, with this scalar serving as a proxy for surfactant concentration (Ermakov *et al.*, 1992). As the internal waves impact the surface, the distribution of the scalar field is re-organized into a spatial pattern that overall correlates well with the internal wave field (see a snapshot in Fig. 6.14), with the exception of some slicks around $y = 0$ which are formed by wave straining that has occurred earlier at these locations. Of interest to a remote sensing specialist is the ratio Γ/Γ_0, where $\Gamma(x, y, t)$ is the instantaneous scalar concentration at a point and Γ_0 is the initial concentration. When this ratio exceeds a threshold value (Moum *et al.*, 1990), the resulting slicks may indeed become remotely visible. The numerical

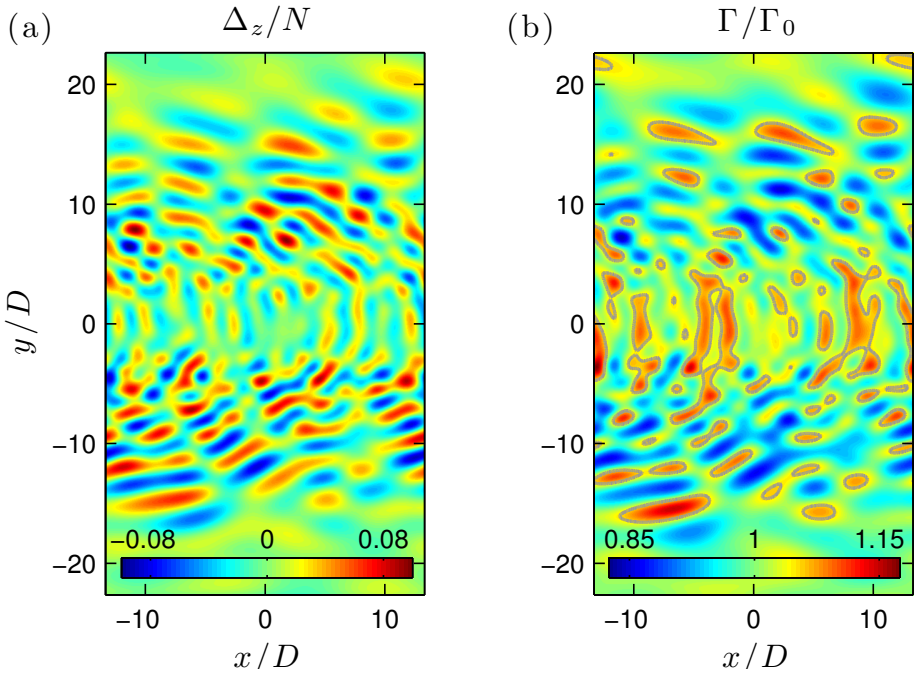

Figure 6.14: Surface snapshot of (a) wave-induced horizontal divergence Δ_z and (b) strain-driven surfactant concentration fields at $Nt = 70$ for R100F64. Concentration of $\Gamma/\Gamma_0 > 1.05$ may correspond to surface slicks that can be detectable via remote sensing. Isolines with $\Gamma/\Gamma_0 = 1.05$ are marked in gray, delineating possible locations of slicks.

results suggest that the above threshold is regularly exceeded (as in Fig. 6.14) for a considerably long duration, particularly at $Re = 10^5$, bearing strong implications for the detectability of the turbulence-emitted IWs.

Linear analysis

It is desirable to correlate the ratio Γ/Γ_0 with the surface velocity strain magnitude. A scaling analysis of the two-dimensional governing equation is performed here. Decompose concentration Γ as

$$\Gamma(x, y, t) = \Gamma_0 + \Gamma'(x, y, t), \tag{6.10}$$

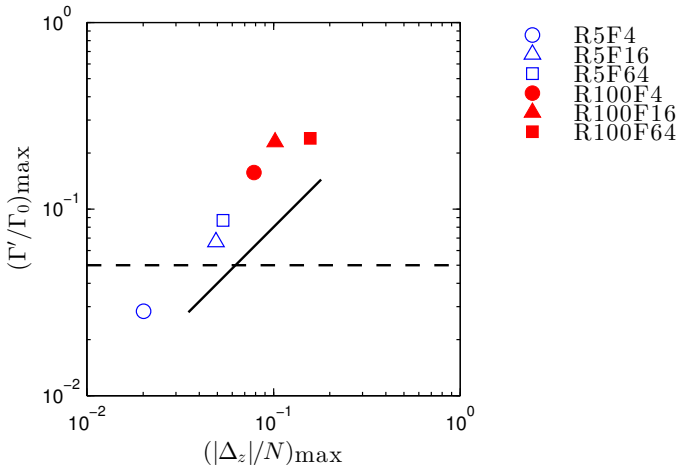

Figure 6.15: Peak surfactant perturbation ratio Γ'/Γ_0 versus the peak dimensionless surface strain $|\Delta_z|/N$ observed in all six simulations. Only $\Gamma' > 0$, i.e., surfactant enrichment, and $\Delta_z < 0$, i.e., flow convergence, are considered. The characteristic enrichment ratio $\Gamma'/\Gamma_0 = 0.05$ (dash line) across observable slicks according to field measurements (Moum *et al.*, 1990) is exceeded by all cases except for R5F4. A scaling of $\Gamma'/\Gamma_0 \sim \Delta_z/N$ (solid line) can be observed.

where Γ' is the perturbation to the background state Γ_0. With this decomposition, the two-dimensional advection equation

$$\frac{\partial \Gamma}{\partial t} + \frac{\partial (\Gamma u)}{\partial x} + \frac{\partial (\Gamma v)}{\partial y} = 0, \tag{6.11}$$

can be re-written as

$$\frac{\partial \Gamma'}{\partial t} + \Delta_z(\Gamma_0 + \Gamma') + u\frac{\partial \Gamma'}{\partial x} + v\frac{\partial \Gamma'}{\partial y} = 0. \tag{6.12}$$

With small perturbations

$$\Gamma' \ll \Gamma_0, \tag{6.13}$$

and the particle's horizontal velocity magnitude much smaller than the waves' celerity, (6.12) reduces to

$$\frac{\partial \Gamma'}{\partial t} + \Delta_z \Gamma_0 = 0. \tag{6.14}$$

Given that

$$\frac{\partial}{\partial t} \sim \frac{1}{T} \sim \omega \sim N, \tag{6.15}$$

the perturbation ratio Γ'/Γ_0 scales as

$$\frac{\Gamma'}{\Gamma_0} \sim \frac{\Delta_z}{N} \tag{6.16}$$

This simple analytical scaling is further confirmed by simulation data (Fig. 6.15), which indeed show that the ratio Γ'/Γ_0 scales with Δ_z/N, a measure of the internal wave steepness (A&D). The surface measured Δ_z/N and subsequently Γ'/Γ_0 show a distinct increase with both *Re* and *Fr* (see §6.3.1), suggesting that at operational parameter values (see §6.5.4), at least for an idealized uniform stratification, these turbulence-emitted waves can produce remotely visible surface patterns.

6.4.3 Wave-driven Lagrangian flows

One may also be interested in the mass transport driven by the reflecting internal waves at the free-slip surface (with vertical velocity $w = 0$). To investigate it, two-dimensional tracking of Lagrangian particles forced by surface (u, v) velocity field from the wake simulations has been performed. These Lagrangian tracers are inserted into the surface two-dimensional flow field at earliest Nt's of each simulations when the surface flow velocities are virtually zero. Large number of tracers are inserted at regularly distributed locations (x_0^+, y_0^+) at the surface at approximately every $0.1D$. The particle tracking scheme employs fourth-order cubic spline interpolation to obtain the particles' instantaneous velocities from the simulation data, and marches in time using a locally fourth-order Adams-Bashforth-Moulton method (Press *et al.*, 2007). In particular, we are interested in the mass transport in the spanwise direction y due to the wave impact. To this

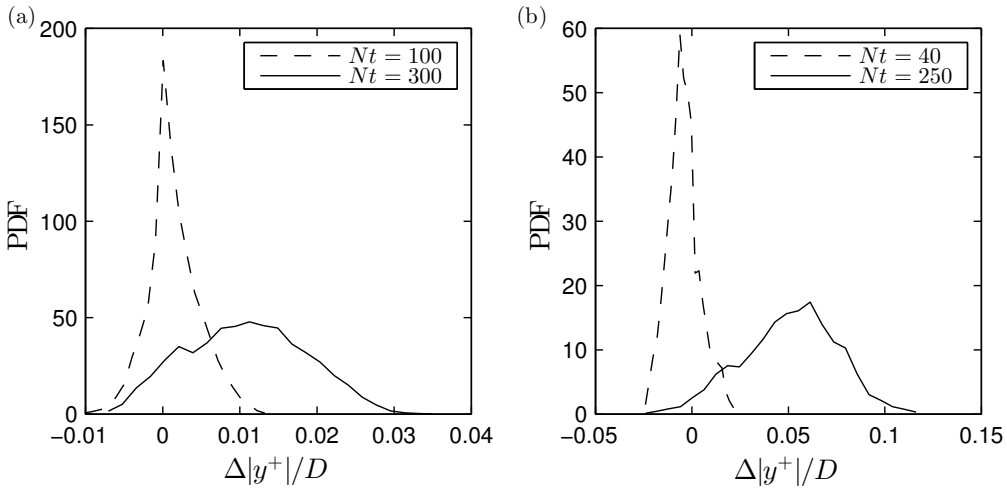

Figure 6.16: PDF of lateral particle displacements of away from the wake centreline at (a) R100F4 and (b) R100F16. Dash lines denote the PDF before the most energetic waves interact with the surface, and the solid lines the PDF after the most energetic wave impact.

end, the lateral displacement

$$\Delta|y^+| \equiv \begin{cases} y^+ - y_0^+ & \text{for } y_0^+ \geq 0, \\ y_0^+ - y^+ & \text{for } y_0^+ < 0, \end{cases} \tag{6.17}$$

can be defined, where $y^+(t)$ is the particle's instantaneous position. Note that $\Delta|y^+|$ is displacement with respect to the initial position y_0^+ and is constructed to be positive when the particle moves *away* from the wake centreline at $y = 0$.

We focus on the lateral transport due to the nonlinear effects of the waves during reflection (Zhou and Diamessis, 2015a). This transport is found to be more significant at the higher $Re = 10^5$ with IWs of higher amplitude interacting with the surface, and the results are shown for R100F4 and R100F16 in Fig. 6.16 (Similar effects were observed for R5F64 but not for R5F4 or R5F16, where the wave amplitudes reaching the surface are much weaker in amplitude and shorter in duration). Before the most energetic waves reach the surface (sampled at $Nt = 100$

and 40 for R100F4 and R100F16 respectively), the PDF of $\Delta|y^+|$ centers around zero with a weak diffusion; after the most intense wave impact (sampled at $Nt =$ 300 and 250 for R100F4 and R100F16 respectively), the PDF diffuses out more and drifts significantly towards the positive values of $\Delta|y^+|$, which implies that the waves push the Lagrangian tracers away from the wake centreline. This collective net motion of tracers at both sides of the wake centreline creates a local divergence in the lateral mass transport at $y = 0$. The magnitude of the drift increases significantly with Fr, i.e., the maximum displacement approximately quadruples as Fr increases from 4 to 16 at $Re = 10^5$. Following the same trend, much larger particle displacements are observed at R100F64. However, the particles at R100F64, especially the ones inserted close to the lateral boundaries of the computational domain, move far enough to reach the lateral sponge layers, where motions are artificially damped out, and get trapped therein, which makes the interpretation of this particular Lagrangian data set ambiguous. Future work is needed in this regard to investigate the Lagrangian dynamics of IW-impacted sea surface at high Fr of the wave-emitting turbulence, with an even wider domain in the lateral direction to accommodate increasing particle excursion length scales with Fr. Although the Lagrangian effects reported here may be considerably weak, i.e., net drifts on $O(0.01)$ to $O(0.1)$ of the diameter of the turbulence-generating body, the effect seems to scale strongly with Fr and may potentially be significant at operational parameter values (see §6.5.4).

6.5 Discussion

6.5.1 Physical processes relevant to IWs in the far-field

In the present study, the far-field evolution of turbulence-emitted internal waves has been examined within a uniform stratification underneath a free-slip rigid lid at which the waves reflect. It turns out that the most relevant process determining details of wave observations at the sea surface is the dispersion of these waves in both wavenumber and frequency domains. In §6.3.2, it is shown that the dispersion in the wavenumber domain causes a decay of observable wavelength as $(Nt)^{-1}$ which can be predicted by a linear propagation model and thus reveals the linear nature of these waves in the far-field. The linear propagation model, combined with the knowledge of most energetic wavelength $\hat{\lambda}_H$, also successfully predicts the $Fr^{1/3}$-scaling of the arrival time of peak wave impact in Nt, as discussed in §6.3.1. In §6.3.3, it is demonstrated that waves of a wide range of frequencies disperse broadly in the lateral direction of the wake flow, and the degree of this dispersion is expected to correlate to the distance of vertical propagation of the waves. Dispersion in both domains may bear observational implications for inferring the dynamic state of wave-emitting turbulence as measured by the Nt value. Moreover, these linear far-field effects may be contrasted to the presumably nonlinear wave-turbulence interactions through which these waves are generated.

On the other hand, it is known that finite-amplitude internal waves can incur nonlinear effects upon reflection or collision of beams (Lamb, 2004; Tabaei *et al.*, 2005; Zhou and Diamessis, 2013). Are nonlinear reflection or other forms of wave-wave interaction a relevant process to the waves' surface signatures? To clarify this, auxiliary simulations (not shown) have been performed to replicate the R5F4

and R100F4 cases in a very similar set-up but in a taller domain (by $4D$) and with a sponge layer ($2D$-thick) installed at the topmost horizontal surface. In such a modified set-up, upward-going waves are absorbed by the top sponge layer and thus not allowed to reflect back to the domain, or interact with subsequently arriving waves. Comparison can be made between the free-slip surface in the original set-up and the xy-plane in the modified set-up which used to be the free-slip surface, i.e., at $z = 9D$; the latter case is expected to have no nonlinear effects due to wave-wave interactions. Visual inspections (not shown) of the wave field at the two horizontal planes do not seem to show noticeable difference in terms of spatial patterns, which suggests that nonlinear wave effects do not cause any major modification to the surface observations at $Fr = 4$; however, we are not able to perform the same comparison at $Fr \in \{16, 64\}$ for which the wave amplitudes are higher, due to the prohibitive computational cost. Moreover, it is found in §6.4.3 that wave-induced Lagrangian transport, which is expected to be a second-order nonlinear effect in the wave's amplitude (Zhou and Diamessis, 2015a), scales strongly with Fr. In summary, while the nonlinear effects found in the wave-reflecting subsurface are not very strong in the cases examined here, it is still premature to reject their importance in the real oceanic parameter range (see more in §6.5.4) where the wave amplitudes might be higher.

With nonuniform stratification, the far-field evolution of these waves would become more complicated due to various linear (Mathur and Peacock, 2009) and nonlinear (Akylas *et al.*, 2007; Grisouard *et al.*, 2011; Mercier *et al.*, 2012; Diamessis *et al.*, 2014; Wunsch *et al.*, 2014) processes, such as generation of harmonics and internal solitary waves. But the wave characteristics reported here can be used as the input wave characteristics just entering the pycnocline for IW propagation models such as the ray-tracing method (Broutman *et al.*, 2004). The complex

near-surface processes (Soloviev and Lukas, 2006), such as wind-driven turbulence and/or Langmuir circulation, can also modify the surface manifestation, which deserves further study.

6.5.2 Wave selection mechanism

It has been shown in that the wake parameters, i.e., Fr and Re, play a significant role in selecting the most energetic wavelength $\hat{\lambda}_H$ emitted by the turbulence. The question remains as to how the wavelengths of these IWs correlates to the the various length scales of the localized stratified turbulence. One might be tempted to correlate $\hat{\lambda}_H$ to the size of quasi-two-dimensional coherent structures within the wake. It is known that the Strouhal number $St = D/\lambda_x$ scales as $(x/D)^{-1/3}$, where λ_x is the horizontal length scale of the coherent structures, and λ_x scales similarly with the wake half-width L_H (Spedding, 2014). As a result,

$$\frac{\lambda_x}{D} \propto (\frac{x}{D})^{1/3} \propto (Nt)^{1/3} Fr^{1/3}. \tag{6.18}$$

Although the $Fr^{1/3}$ scaling is recovered, the horizontal scales λ_x or L_H are not sensitive to Re, whereas the most energetic λ_H is indeed Re-dependent (see Fig. 6.9).

One may alternatively look for vertical length scales which may possibly decide the wavelength of the emitted IWs. A&D argued that the the wavelength may be determined by the wake half-height L_V, which stays relatively constant during the NEQ regime (DSD) and is 2 to 4 times of the Ozmidov scale $\ell_O \equiv \sqrt{\varepsilon/N^3}$ at the onset of buoyancy control, the latter scaling as $Fr^{1/3}$ (Spedding, 2002). The challenge associated with testing this hypothesis is that the Ozmidov scale involves the dissipation rate ε which cannot be determined directly from the implicit large-

eddy simulations performed here (DSD).

Alternatively, one can consider the vertical integral length scale of the stratified turbulence. At buoyancy Reynolds number $\mathcal{R} = \varepsilon/(\nu N^2) > 1$ (as is the case during the transition to NEQ and onward in our $Re = 10^5$ simulations; see DSD),

$$\ell_V \sim \frac{u'}{N}, \tag{6.19}$$

where ℓ_V can be interpreted as the vertical Taylor scale of the turbulence (Billant and Chomaz, 2001; Riley and Lindborg, 2012). In the context of a wake,

$$u' \sim U_0, \tag{6.20}$$

where U_0 is the maximum centreline velocity and thus

$$\ell_V \sim \frac{U_0}{N}. \tag{6.21}$$

Therefore,

$$\frac{\ell_V}{D} \sim \frac{U_0}{ND} = \frac{1}{2}\frac{U_0}{U} Fr. \tag{6.22}$$

Noting that

$$\frac{U_0}{U} \propto Fr^{-2/3} \tag{6.23}$$

at a given Nt (Spedding, 1997), one can write

$$\frac{\ell_V}{D} = C_\ell Fr^{1/3}. \tag{6.24}$$

However, it is unclear whether the above scaling arguments which led to (6.24) hold for the $Re = 5 \times 10^3$ considered here. At this Re, the wake flow is significantly impacted by viscosity and (6.24) not likely to hold. Nevertheless, simulation results (not shown) indicate that at the early stage of the NEQ regime, i.e., $2 \leq Nt \leq 20$, (6.24) does hold for both Re considered. This window of time has been identified

as the one when IWs are most radiated (A&D). C_ℓ is found to be dependent on Re during the above time interval as

$$C_\ell = \begin{cases} 0.2 \quad \text{at } Re = 5 \times 10^3, \\ 0.1 \quad \text{at } Re = 10^5. \end{cases} \tag{6.25}$$

The computation of the volume-averaged vertical Taylor scale ℓ_V follows the definition proposed by Riley and de Bruyn Kops (2003). In §6.3.2, the most energetic wavelengths $\hat{\lambda}_H$ as identified by the peaks of the PDFs (Fig. 6.5) are found to follow

$$\frac{\hat{\lambda}_H}{D} = C_\lambda Fr^{1/3}, \tag{6.26}$$

where

$$C_\lambda = \begin{cases} 1.2 \quad \text{at } Re = 5 \times 10^3, \\ 0.6 \quad \text{at } Re = 10^5, \end{cases} \tag{6.27}$$

as seen in Fig. 6.9. Therefore, ℓ_V and $\hat{\lambda}_H$ indeed scale very similarly in both Fr and Re, i.e., a $Fr^{1/3}$ scaling and a 50% decrease occurs as Re increases from 5×10^3 to 10^5, according to (6.24) to (6.27). A scaling of

$$\hat{\lambda}_H \sim 6\ell_V, \tag{6.28}$$

based on the coefficients in (6.25) and (6.27), seems to hold within the parameter range examined, where $\hat{\lambda}_H$ is the most energetic horizontal wavelength emitted by the turbulence of vertical Taylor scale ℓ_V during the NEQ regime. However, this observation only holds at the two Re's examined here and requires verification at higher Re's; the physical mechanism behind this correlation is unknown to us and requires further study focusing on wave-turbulence interactions in the wake's near-field.

6.5.3 Comparison to Abdilghanie and Diamessis (2013)

A&D reported the *near-field* wave characteristics from a very similar numerical set-up to the present study. They reported a significant *prolongation* of wave radiation at $Re = 10^5$ as compared to $Re = 5 \times 10^3$, which was attributed to the hypothesized persistent wave generation by the secondary turbulence linked to Kelvin-Helmholtz instability events during the NEQ regime of the wake. However, this hypothesis is not supported by our observations in the *far-field*; based on our analysis (§6.3.1) that is consistent with the observations, the most energetic waves simply are *delayed* in reaching the observation plane at the sea surface, because the most energetic wavelength $\hat{\lambda}_H$ is smaller at higher Re (by a factor of 2 as compared to the lower Re; see Fig. 6.9) and thus the waves are slower in propagation.

Note that the effectiveness of the linear model (§6.3.2) in describing the wavelength variation in time as $(Nt)^{-1}$, relies on the fact that the waves are all generated within a fairly short time interval in the early wake at $t_0 \ll t$, where t is the time at which these waves are observed in the far-field. Should the secondary turbulence (which occurs at $30 \leq Nt \leq 100$ as observed by DSD) indeed contribute significantly to wave emission, the assumption that the waves are generated impulsively in the early wake would break down, and the linear model (§6.3.2) would not have worked. Therefore, at the range of wake parameters examined here, secondary turbulence does not seem to generate internal waves efficiently, at least not enough to noticeably impact the far-field; all waves seem to be generated fairly impulsively in the early wake by the more energetic turbulence, as can be inferred from the time variation of wavelength at the sea surface.

6.5.4 Higher *Fr*? Higher *Re*?

Spedding (2014) estimated the Re and Fr of geophysical and naval wakes, which are in a higher range than those investigated in the present study. For example, wakes relevant to naval applications have $Re = O(10^8)$ and $Fr = O(10^3)$. In the range of Fr investigated, the potential of IW generating far-field effects increases with Fr. However, at infinite Fr, i.e., when the fluid is unstratified, there is no IW expected to be radiated from the wake. Therefore, a natural question to ask is if there exists an optimal wake Fr for maximum far-field impact. On the other hand, Re-dependence is seen in IW amplitude and dominant wavelength. Question remains as to whether these wave characteristics reach an asymptote at high Re's of oceanic relevance. Moreover, the breaking of these turbulence-emitted waves in the wake's near-field may be possible when the wave amplitude further increases with Re and Fr, which may further complicate the manifestation of these waves in the far-field. Although computations at higher Re's and Fr's can be considerably expensive, ongoing efforts are devoted towards investigating wake physics at a higher Re than the maximum value considered here, and this is discussed in the next chapter of this dissertation.

CHAPTER 7

REYNOLDS NUMBER EFFECTS IN STRATIFIED WAKES

In this chapter, we focus on the stratified turbulence in a towed-sphere wake, a canonical *localized* stratified turbulent flow, with an emphasis on the effects of Reynolds number Re on the dynamics of the turbulence, i.e., evolution of vortical structure, mean flows, the scaling of turbulence length scales, and turbulent transport coefficients (in both horizontal and vertical directions). What has enabled us to investigate the Reynolds number effects more systematically in this dissertation is a set of massively-parallel simulations performed at $Re = 4 \times 10^5$ and $Fr \in \{4, 16, 64\}$, taking $O(2 \times 10^7)$ CPU hours. It is the first time that the spectral multi-domain Navier-Stokes solver (Diamessis *et al.*, 2005) (hereinafter referred to as "DDH") has been implemented in the implicit large-eddy simulation (LES) mode to simulate the towed-sphere wake at such a Reynolds number, quadrupling what was achieved by Diamessis *et al.* (2011) (hereinafter referred to as "DSD"), i.e., $Re = 10^5$.

7.1 Numerical considerations

In this section, key numerical aspects of these simulations are reviewed, including the specific choice of grid resolution and LES filters to ensure the adequate resolution of the flow physics, as well as numerical stability. As discussed in §3, the implicit LES solver employed in this study does not implement explicitly a particular subgrid scale (SGS) model; instead, spectral filtering is applied directly to the flow field to drive the downscale energy flux in spectral space and prevent spectral blockage at the smallest resolved scales. Spectral filtering is applied to both horizontal directions and in the vertical in a similar fashion; for the ease of discussion, we will focus on the horizontal directions, as the relation between a

Fourier mode and the corresponding length scale can be more directly established. The particular filter function used corresponds to a *transfer function* $\widehat{G}$ (Pope, 2000) of an exponential form:

$$\widehat{G}(k) = \exp[-\alpha(\frac{k}{N})^p], \tag{7.1}$$

where $k = -N+1, ..., -1, 0, 1, ..., N$ is the mode number (e.g., in the periodic x direction, N_x grid points in physical space correspond to $2N$ Fourier modes), and $\alpha = -\ln \epsilon_M$, where ϵ_M is the machine epsilon. It is of interest to define a cut-off wavenumber (after (13.14) of Pope (2000)),

$$k_c \equiv \frac{\pi}{\Delta}, \tag{7.2}$$

a wavenumber above which the energy is damped by the particular choice of filter. In other words, Δ is the cut-off length scale between the resolved and sub-grid (or, to be exact, "sub-filter") scales, or the *turbulence-resolution length scale* (Pope, 2004). If the length scale of the characteristic of the flow geometry is $\mathcal{L}$ (for our discussion, let $\mathcal{L} \sim D$, where D is the sphere diameter), and the grid spacing is h, in order to choose a filter length scale Δ (which is achieved by varying p and N in (7.1)), one is to optimize two dimensionless ratios: $\Delta/\mathcal{L}$ (or Δ/D) and Δ/h. Following the discussions in §13.2.4 and §13.2.5 of Pope (2000), it is desirable to *minimize* $\Delta/\mathcal{L}$ (or Δ/D) in order to retain most of the energy in the resolved field, and at the same time, to *maximize* Δ/h in order that the sub-filter field is resolved adequately such that the simulation is numerically accurate (specifically, the solution being independent of the choice of h, see Pope (2004)) and stable. The two conflicting sets of criteria pose a challenge to choosing the optimal filter length scale Δ for our LES; below our rationale for our particular choice of Δ is described.

With $\mathcal{L}$ (or D) fixed for a given problem, one has the freedom to choose Δ and

h (varying the latter is of course subject to the limit of computational resources) to achieve the desirable Δ/D and Δ/h. If we consider the x direction for an example, the transfer function of the exponential filter (7.1) is written below in various forms to facilitate our discussion (note that p is replaced by p_F, where the latter denotes the order of *Fourier* filter in the horizontal directions):

$$\begin{aligned}\widehat{G}(k_x; N, p_F) &= \exp[-\alpha(\frac{k_x L_x}{2\pi N})^{p_F}] \\ &= \exp[-\alpha(\frac{\beta k_x D}{2\pi N})^{p_F}] \\ &= \exp[-\alpha(\frac{k_x h}{\pi})^{p_F}],\end{aligned} \tag{7.3}$$

where the wavenumber

$$k_x = k\frac{2\pi}{L_x},$$

the uniform grid spacing

$$h = \frac{L_x}{N_x} = \frac{L_x}{2N},$$

and

$$\beta = \frac{L_x}{D} = \frac{80}{3}$$

measures the length of the domain in x relative to the sphere and is fixed across all simulations.

Several observations can be made based on (7.3):

- $\widehat{G}$ for a given k_x depends on both N (grid resolution) and p_F (filter order), if one is to fix L_x;
- $\widehat{G}$, **when expressed in terms of** $k_x D$, depends on both N and p_F: N determines the end point of the spectrum (see Fig. 7.1)

$$(k_x D)_{max} = N\frac{2\pi}{L_x}D = N\frac{2\pi}{\beta},$$

and p_F effectively sets the cutoff wavenumber (see Fig. 7.2)

$$k_c D = \frac{\pi}{\Delta/D}$$

at which the transfer function starts to drop below unity. Either increasing filter order p_F (using a *weaker* filter) or increasing N_x (using better grid resolution) increases $k_c D$ and thus reduces Δ/D, which is desired for retaining more turbulent kinetic energy in the resolved field;

- $\widehat{G}$, **when expressed in terms of** $k_x h$, depends solely on p_F. The maximum $k_x h$

$$(k_x h)_{max} = N\frac{2\pi}{L_x}\frac{L_x}{2N} = \pi$$

is independent of N (N_x) or p_F (see Figs. 7.3 and 7.4), and p_F is the only parameter that one can adjust to achieve the desirable cut-off wavenumber (now normalized by $1/h$)

$$k_c h = \frac{\pi}{\Delta/h},$$

regardless of the number of grid points N_x (see Fig. 7.4). One is to achieve a better (larger) Δ/h ratio (and thus stronger numerical accuracy/stability) by using a smaller filer order p_F (a *stronger* filter).

The filters employed in the simulations of $Re \in \{5 \times 10^3, 10^5, 4 \times 10^5\}$ in this dissertation are presented below: $\widehat{G}$ is plotted as a function of $k_x D$ in Fig. 7.5, and $\widehat{G}$ as a function of $k_x h$ in Fig. 7.6. Our focus is on how the particular choice of N_x and p_F affect the cut-off wavenumber k_c and thus the Δ/D and Δ/h ratios. On one hand, added resolution (larger N_x and finer h) at increasing Re's ensures a sufficiently small Δ/D ratio, i.e., $\{0.16, 0.12, 0.059\}$ for R5, R100, R400 respectively[1], such that the resolved scale is at least one decade into the inertial

[1]Hereinafter, each simulation will be labeled as RaFb, where $a = Re/10^3$ and $b = Fr$.

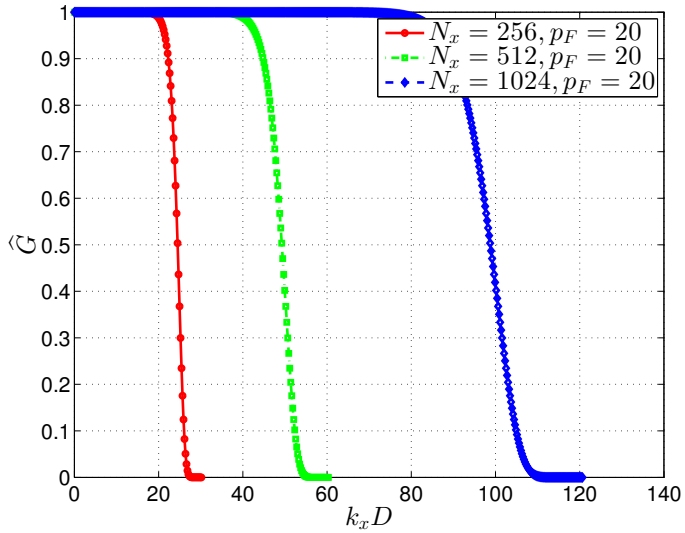

Figure 7.1: Transfer function $\widehat{G}$ as a function of $k_x D$ with $p_F = 20$ and $N_x \in \{256, 512, 1024\}$ respectively. The dimensionless cut-off wavenumber $k_c D$ increases as N_x increases, resulting in smaller Δ/D ratio, while p_F is fixed.

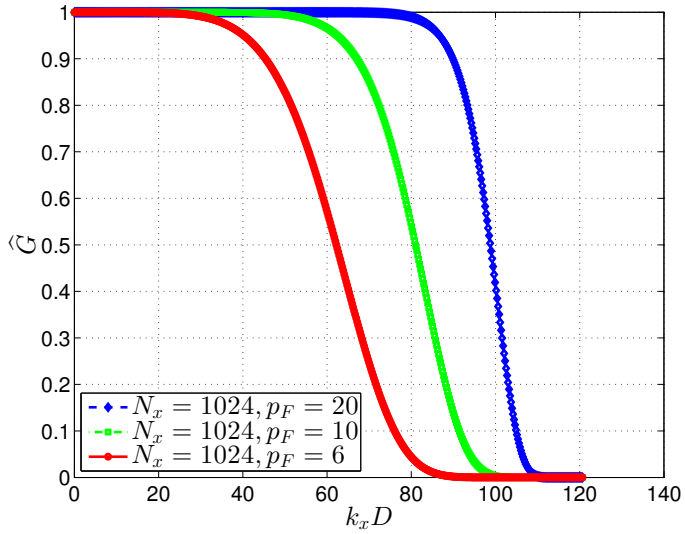

Figure 7.2: Transfer function $\widehat{G}$ as a function of $k_x D$ with $N_x = 1024$ and $p_F \in \{20, 10, 6\}$ respectively. The dimensionless cut-off wavenumber $k_c D$ increases as p_F increases, resulting in smaller Δ/D ratio, while N_x is fixed.

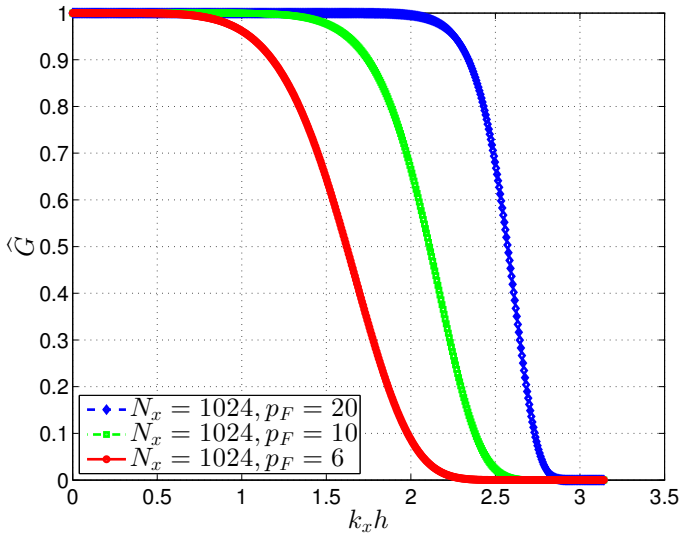

Figure 7.3: Transfer function $\widehat{G}$ as a function of $k_x h$ with $N_x = 1024$ and $p_F \in \{20, 10, 6\}$ respectively. The dimensionless cut-off wavenumber $k_c h$ decreases as p_F decreases, resulting in larger Δ/h ratio, while N_x is fixed.

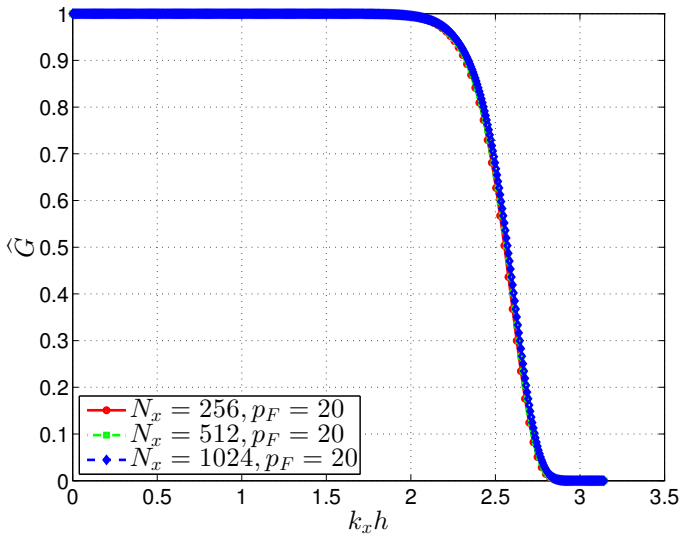

Figure 7.4: Transfer function $\widehat{G}$ as a function of $k_x h$ with $p_F = 20$ and $N_x \in \{256, 512, 1024\}$ respectively. The dimensionless cut-off wavenumber $k_c h$ does not vary with N_x.

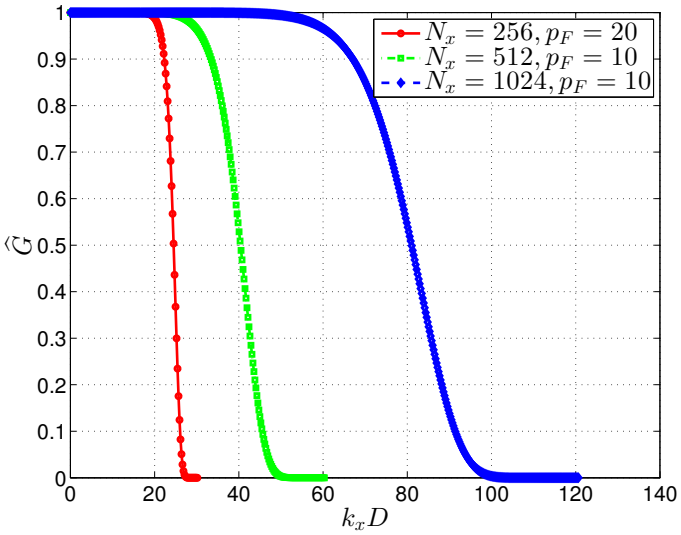

Figure 7.5: Transfer function $\widehat{G}$ as a function of $k_x D$ for $Re \in \{5\times10^3, 10^5, 4\times10^5\}$ in red, green and blue respectively. The dimensionless cut-off wavenumber $k_c D$ (as measured by the wavenumber at which $\widehat{G}$ drops to 0.99) is 19.8, 26.2 and 53.0 for $Re \in \{5\times10^3, 10^5, 4\times10^5\}$ respectively, corresponding to Δ/D ratios of 0.16, 0.12 and 0.059.

subrange at the two higher Re's (not shown). On the other hand, in order to attain a sufficiently large Δ/h for numerical stability, a stronger filter (lower values of p_F) is used at the higher two Re's, where the degree of under-resolution (of the subfilter scales) is expected to be higher. It is recommended by Pope (2004) that $\Delta/h \geq 4$ for a scheme with second-order spatial accuracy and $\Delta/h \geq 2$ for a sixth-order scheme, in order to remove the dependence of the solution on h (Vreman *et al.*, 1997; Chow and Moin, 2003); for our scheme with spectral accuracy numerically, Δ/D ratios (Fig. 7.6) of 1.5 (at R5) and 2.3 (at R100 and R400) seem to be reasonably satisfactory. The grid resolution and filter order used are tabulated in Table 7.1.

Spectral filtering is also applied in the vertical direction on the Legendre modes (modal coefficients corresponding to orthogonal polynomials used to discretize the domain in the vertical, in contrast to Fourier series used in the horizontal) within

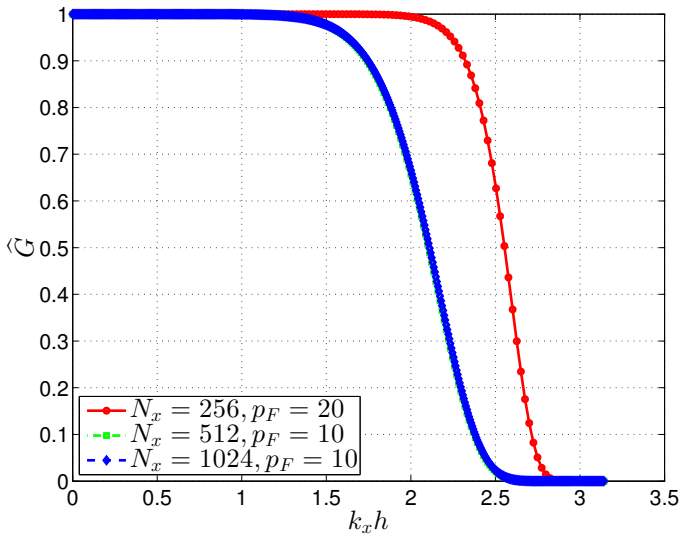

Figure 7.6: Transfer function $\widehat{G}$ as a function of $k_x h$ for $Re \in \{5\times10^3, 10^5, 4\times10^5\}$ in red, green and blue respectively. The dimensionless cut-off wavenumber $k_c h$ (as measured by the wavenumber at which $\widehat{G}$ drops to 0.99) is 2.06, 1.38, and 1.38 for $Re \in \{5\times10^3, 10^5, 4\times10^5\}$ respectively, corresponding to Δ/h ratios of 1.5, 2.3 and 2.3.

	N_x	$(M, \hat{N})$	(p_F, p_L)
$Re = 5 \times 10^3$	256	$(13, 18)$	$(20, 10)$
$Re = 10^5$	512	$(21, 32)$	$(10, 8)$
$Re = 4 \times 10^5$	1024	$(17, 64)$	$(10, 6)$

Table 7.1: Summary of grid resolution and filter orders for all three Reynolds numbers. The number of vertical subdomains M in the vertical is reported on the $z/D \in [-6, 6]$ interval for the ease of comparison, as domain height also varies with Froude number; for the horizontal direction, the number of grid points in x is reported to cover a fixed domain length of $80D/3$; the grid resolution in y is the same as in x at the beginning of the simulation but is subject to regridding (doubling the domain size with the same number of grid points, see details in DSD) as the width of the wake exceeds a certain threshold.

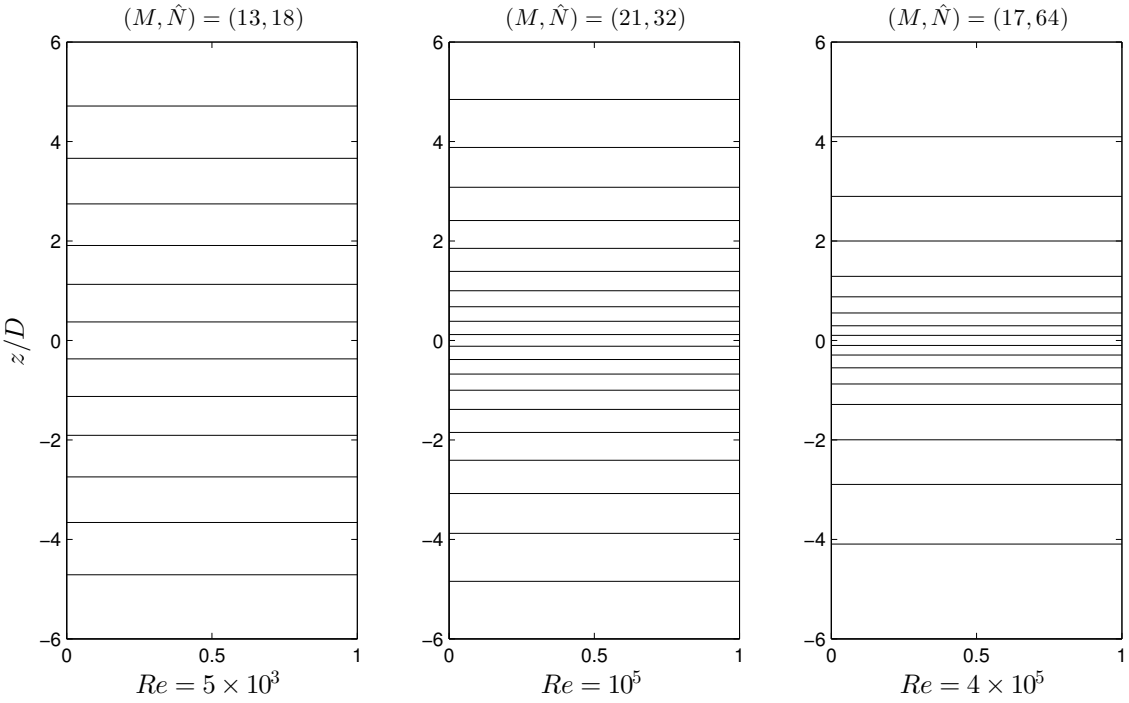

Figure 7.7: Subdomain distributions for for all three Reynolds numbers on the $z/D \in [-6, 6]$ interval. The black horizontal lines delineate subdomain interfaces with the local Gauss-Lobatto-Legendre (GLL) grid omitted for clarity.

each subdomain, and the filter order p_L can be found in Table 7.1. Two measures are taken to ensure adequate resolution in the vertical: First, smaller subdomains are allocated around the wake core (see Fig. 7.7), utilizing the flexibility given by the multidomain approach. Second, the number of grid points is adjusted through the number of subdomains M and order of polynomial approximation $\hat{N}$ (see Table 7.1) to provide better resolution at increasing Re's. For $Re \in \{5 \times 10^3, 10^5\}$, no fewer grid points in the vertical than those used by DSD are used, and the results at these two Re's agree well with those of DSD's, in terms both mean wake evolution, energy spectrum and flow structures (not shown); for the $Re = 4 \times 10^5$ simulation, the vertical resolution is doubled from the $Re = 4 \times 10^5$ case, after the $Re^{-1/2}$ scaling of the vertical scale of turbulence proposed by Riley and de Bruyn Kops (2003) and

employed by DSD to determine the vertical resolution needed. Similar to DSD, while the onset of secondary Kelvin-Helmholtz instabilities in the NEQ regime can be observed in the simulations with sufficiently high Re (see §7.2), the even smaller scales generated by these events may be either marginally resolved or unresolved, subject to the effect of spectral filtering (see more discussions in DSD). Moreover, the implicit LES of stratified wakes at $Re = 10^5$ has been partially verified through direct numerical simulations (DNS) as a part of an ongoing combined DNS/LES study of stratified turbulence. These DNS verifications of our implicit LES results, courtesy of Professor Stephen de Bruyn Kops of University of Massachusetts, are presented in Appendix D.

For the simulations at $Re = 4 \times 10^5$, the domain dimensions, i.e., $(L_x, L_y, L_z) = (80/3, 40/3, 12)D$, are reduced from their lower Re counterpart (Table 6.1), in accordance with the increasing computational cost with Re and the shift of focus from the far-field evolution of the turbulence-emitted internal waves to the dynamics of the turbulence core. Accordingly, the top boundary of the domain is also overlaid with a wave-absorbing sponge layer at $Re = 4 \times 10^5$, in contrast to the simulations at $Re \in \{5 \times 10^3, 10^5\}$ discussed in §6. The domain width $L_y/D = 40/3$ in the spanwise direction is reported at the beginning of the simulation and is subject to regridding as the simulation proceeds and wake width expands (see more in DSD). The wakes are simulated up to 1000 buoyancy time units since the passage of the sphere, i.e., the $Re = 4 \times 10^5$ simulations are terminated at dimensionless time $Nt = 1000$.

7.2 Flow phenomenology

7.2.1 Quasi-horizontal vortical motion

The first objective is to examine the effect of wake Reynolds number Re on the vortical structures in the turbulent flow field. Contour plots of the vertical vorticity ω_z on the Oxy centerplane of the flow (sampled at times $Nt = 1, 10, 30$ and 70) are shown in Fig. 7.8. By the time $Nt = 30$, the flow has transitioned into a more organized structure with quasi-horizontal vortical strucutres[2] (or the precursor to their formation) beginning to emerge. As Re increases from 10^5 to 4×10^5, the fine-scale structure within the flow grows significantly richer. At a given Nt value, the width of the wake is generally larger at a higher Fr. The vortical structure at a later time, i.e., at $Nt = 150$, is shown in Fig. 7.9. While any fine-scale motions have disappeared completely and only the pancake vortices are visible for the R5F4 case, these secondary motions are more intense and persistent at a higher Re. By the time $Nt = 150$ for the R100F4 case, pancake vortices have emerged, with the fine-scale motions embedded within them, whereas for the R400F4 case, the fine-scale motions are dominant and overwhelm what seems to be the precursor to the pancake formation in the flow.

7.2.2 Buoyancy-driven shear layers

Figs. 7.10 and 7.11 show the spanwise vorticity ω_y, sampled over a sub-window on the Oxz centerplane of the flow at times $Nt = 1, 30, 50, 70, 100$ and 200. At $Nt = 1$ which is during the three-dimensional (3D) regime (Spedding, 1997), the flow exhibits a structure typical of active three-dimensional turbulence. The 3D

[2]Commonly referred to as "pancake vortices".

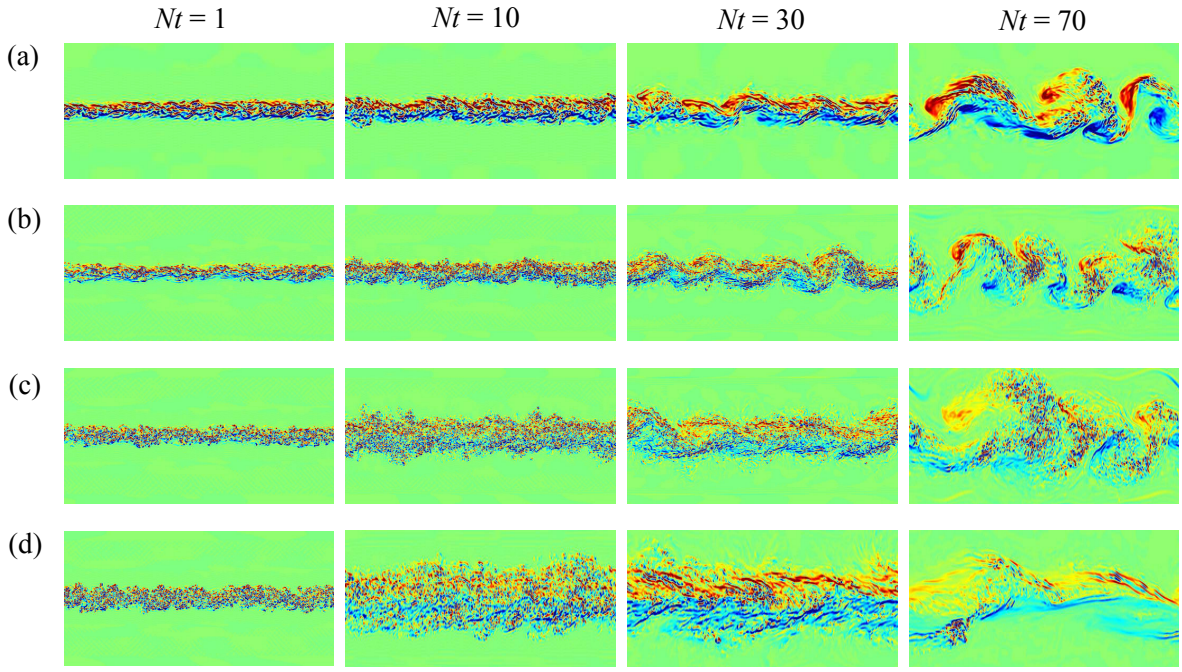

Figure 7.8: Contour plots of ω_z sampled at different times on a $26\frac{2}{3}D \times 13\frac{1}{3}D$ subsection of the Oxy centerplane for simulations: (a) R100F4, (b) R400F4, (c) R400F16 and (d) R400F64. The sphere travels from left to right. At each snapshot, the color bar limits are rescaled dynamically and symmetrically, about $\omega_z = 0$ to $\pm(|\omega_z^{max}| + |\omega_z^{min}|)/6$. The minimum/maximum range for the color bars for $\omega_z/(U/D)$ at $Nt = 70$ for each simulation is (a) $[-0.17, 0.17]$, (b) $[-0.30, 0.30]$, (c) $[-0.13, 0.13]$ and (d) $[-0.055, 0.055]$.

turbulence, under the effect the buoyancy, transitions into structure characterized by distinct inclined layers, symmetrically positioned with respect to the wake centerline. For the snapshots shown, the height of the wake increases with Fr remains near-constant with time, in contrast to the wake width; the thickness of the buoyancy-driven shear layers also increases with Fr and decrease with Re. The similarity scaling of mean wake height will be discussed in §7.3, and the thickness of the shear layers in §7.4. During this non-equilibrium (NEQ) regime, distinct Kelvin-Helmholtz (K-H) instabilities develop between the buoyancy-driven shear

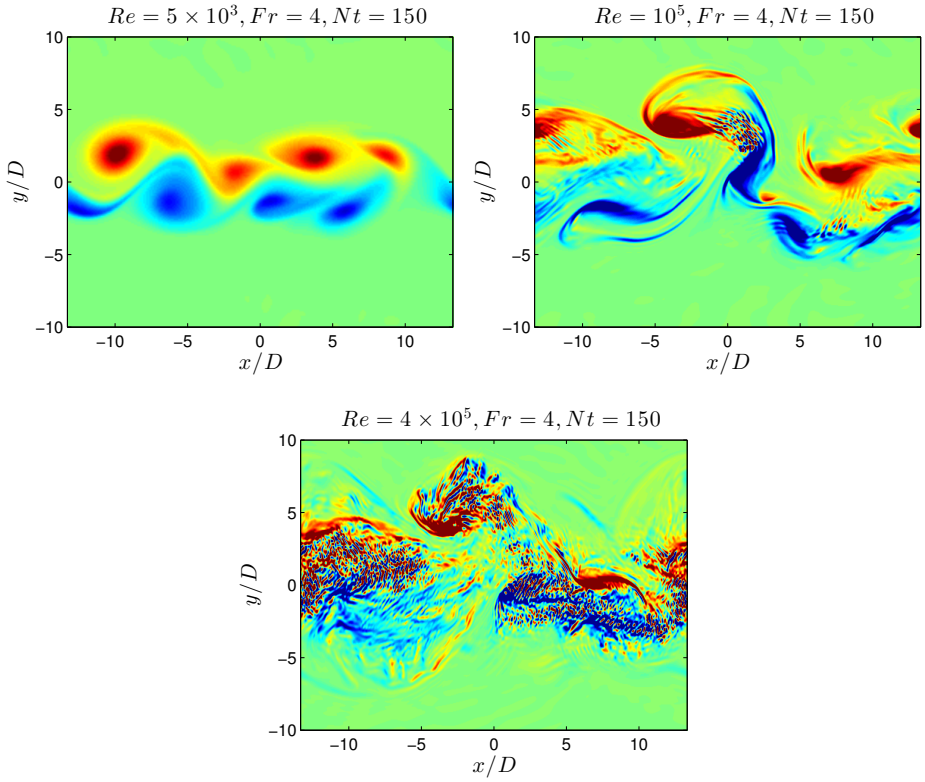

Figure 7.9: Contour plots of ω_z sampled at $Nt = 150$ on a $26\frac{2}{3}D \times 20D$ subsection of the Oxy centerplane for simulations: (a) R5F4, (b) R100F4 and (c) R400F4. The minimum/maximum range for the color bars for $\omega/(U/D)$ for all simulations is (a) $[-0.067, 0.067]$.

layers and destablized them, more constantly at an early Nt value and becoming more intermittent as time goes by. The comparison between panels (a) and (b) of Figs. 7.10 and 7.11 featuring the flow field at R100F4 and R400F4 suggests that the K-H instabilities are both more intense and longer-lived at a higher Re. While the flow has virtually restabilized at $Nt = 100$ for R100F4 (Fig. 7.11a), the secondary K-H instabilities are still visible for R400F4 (Fig. 7.11b) at up to $Nt = 150$, delaying the flow's transitioning into the quasi-two-dimensional (Q2D) regime where the flow is stable and viscously controlled (Spedding, 1997). This particular trend of the delayed NEQ regime with increasing Re is consistent with

DSD who compared the flow structures at $Re = 5 \times 10^3$ and 10^5.

7.3 Mean flow evolution

Here we examine the self-similar evolution of the characteristic mean velocity and length scales of the wake flow. The values of the centerline velocity U_0, wake half-width L_H and half-height L_V at a certain time are obtained by a least-squares fitting of the x-averaged u velocity[3] $\langle u \rangle$, as a function of (y, z), to a two-dimensional Gaussian profile:

$$\langle u \rangle = U_0 \exp[-\frac{1}{2}(\frac{y}{L_H})^2 - \frac{1}{2}(\frac{z}{L_V})^2] \tag{7.4}$$

which was commonly used to describe the self-similar evolution of the mean flow of towed-sphere wake, e.g., by Spedding (1997) and DSD. The results are shown in Fig. 7.12, which is similar to DSD's Fig. 7.

7.3.1 Mean centerline velocity

The mean centerline velocity U_0 is shown in Fig. 7.12(a), (d) and (e). In Fig. 7.12(a), U_0 is plotted as a function of dimensionless distance to the sphere x/D. For small distances, i.e., in the 3D regime, U_0 decays as $(x/D)^{-2/3}$, similarly to an unstratified axisymmetric wake (Tennekes and Lumley, 1972). The 3D regime is followed by the NEQ regime, where the decay rate of U_0 in x (or t) is reduced from $(x/D)^{-2/3}$ to $(x/D)^{-1/4}$, which was explained by Spedding (1997) on the grounds of energy conversion from the available potential energy to the kinetic. The 3D-NEQ transition is observed to occur at a universal dimensionless time $Nt \approx 2$ (Fig. 7.12(d)) which corresponds to a larger x/D value at a

[3] In this chapter, $\langle . \rangle$ denotes average in the statistically homogeneous x direction.

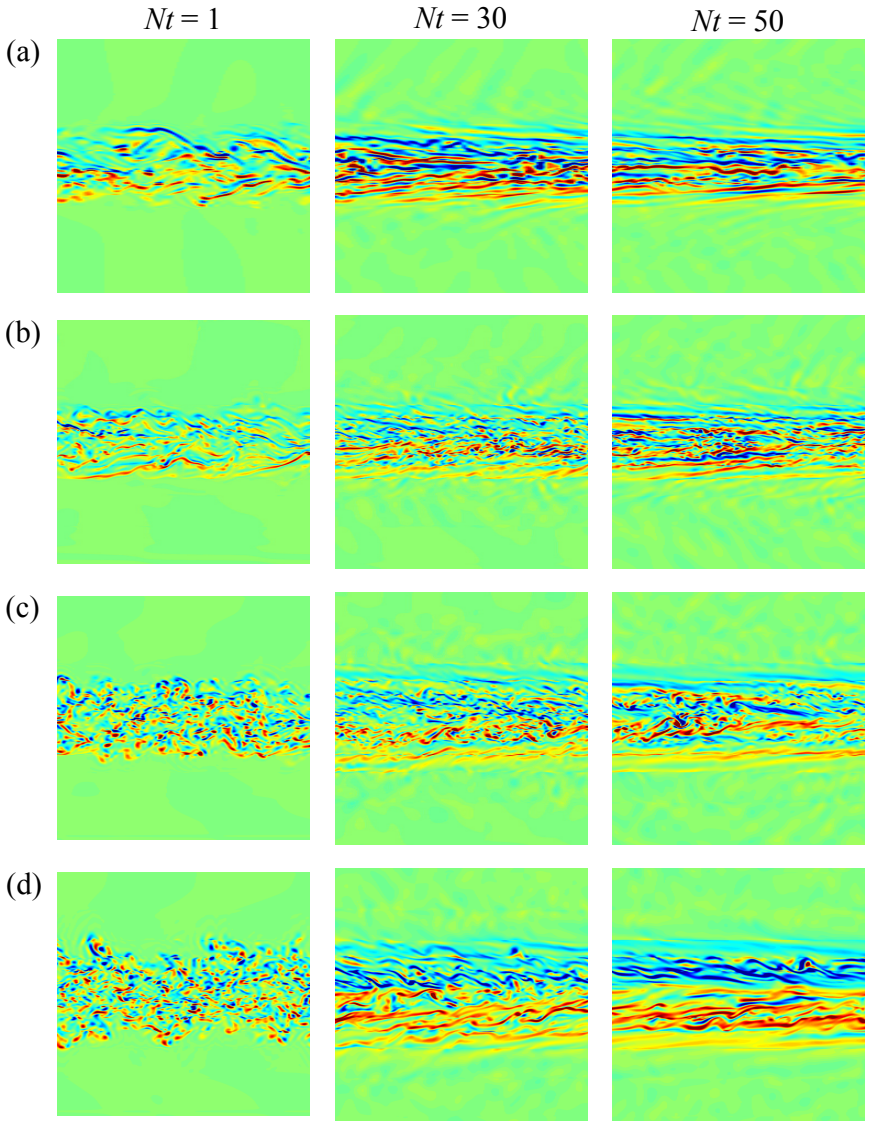

Figure 7.10: Contour plots of ω_y sampled at different times on a $6D \times 6D$ subsection of the Oxz centerplane for simulations: (a) R100F4, (b) R400F4, (c) R400F16 and (d) R400F64. The sphere travels from left to right. At each snapshot, the color bar limits are rescaled dynamically and symmetrically, about $\omega_y = 0$ to $\pm(|\omega_y^{max}| + |\omega_y^{min}|)/6$. The minimum/maximum range for the color bars for $\omega_y/(U/D)$ at $Nt = 50$ for each simulation is (a) $[-0.70, 0.70]$, (b) $[-0.88, 0.88]$, (c) $[-0.33, 0.33]$ and (d) $[-0.082, 0.082]$.

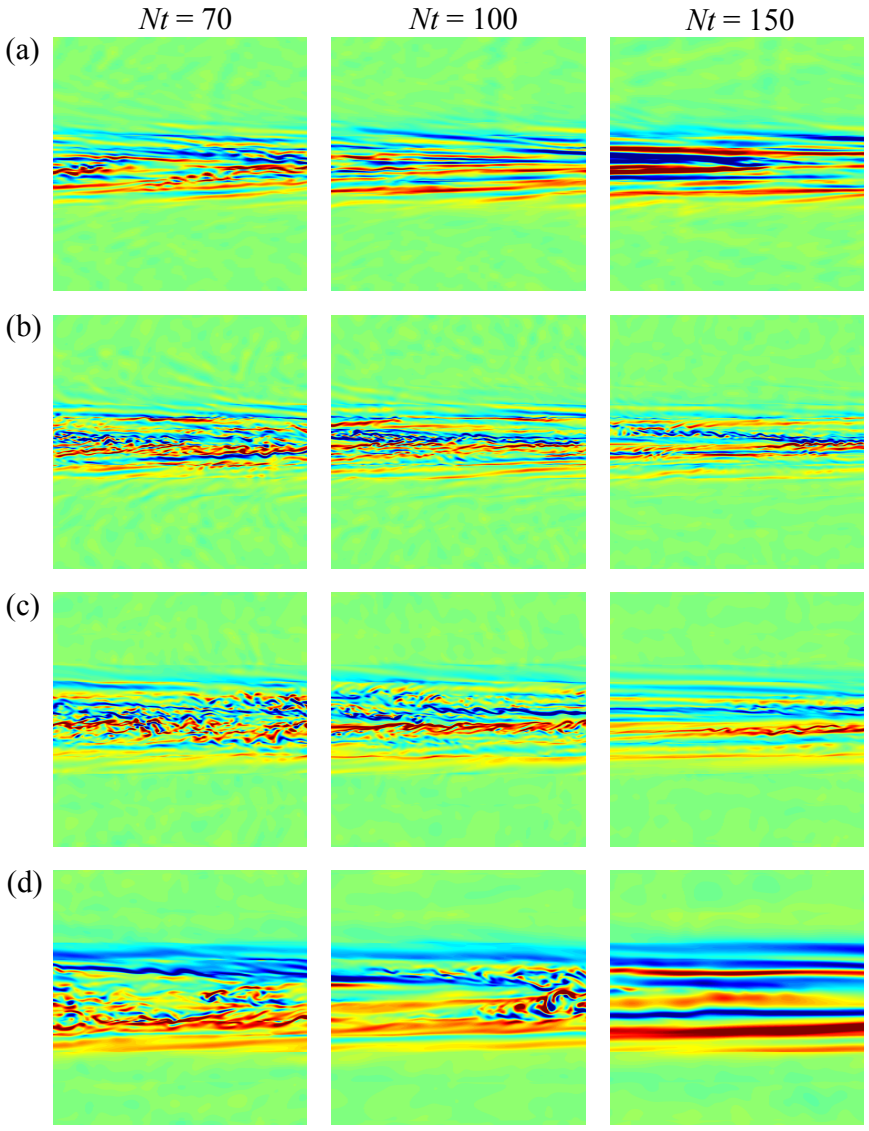

Figure 7.11: The same as in Fig. 7.10, but with snapshots sampled at $Nt =$ 70, 100 and 150.

higher Fr. Spedding (1997)'s $Fr^{-2/3}$ scaling for U_0 at a given Nt seems to hold reasonably well during the NEQ regime (Fig. 7.12(d) and (e)), regardless of Re; however, the Re-dependence seems to be more pronounced at a later Nt, as the curves corresponding to a same Fr but various Re's start to diverge as time advances (Fig. 7.12(e)), with the case of a higher Re in general decays slower. It remains to be examined whether this particular observation is physical, or it is rather an artifact due to the growth of horizontal integral length scales with time, which limits the number of coherent structures that are present in the finite-sized domain and thus introduces statistical uncertainty. The dependence of the NEQ-Q2D transition on Re is so far unclear and warrants further work.

7.3.2 Mean wake dimensions

Fig. 7.12(b) shows the evolution of the mean wake half-width L_H. In the early wake, $x/D < 100$, neither Fr- nor Re-dependence seems to be significant, and L_H grows as $(x/D)^{1/3}$, similarly to an unstratified axisymmetric wake (Tennekes and Lumley, 1972). The curves start to become Fr-dependent for $x/D > 100$, while the Re-dependence is still weak. At a given x/D in the late wake, L_H is larger at a higher Fr; again, question remains as to whether this is due to the statistical uncertainty associated with sampling an insufficient number of coherent structures in the finite-sized computational domain.

Fig. 7.12(c) and (f) show the evolution of the mean wake half-height L_V. In early wake where the control of buoyancy has not been established, L_V grows as $(x/D)^{1/3}$, the same rate as the wake width L_H and similarly to an unstratified axisymmetric wake (Tennekes and Lumley, 1972). This period of "isotropic" growth occurs over a window of x/D values whose extent is dependent on Fr, which is

consistent with the evolution of U_0 (Fig. 7.12(a) and (d)) in the 3D regime. The half-height L_V ceases to grow at $Nt \approx 2$ and remains relatively constant for a considerably long time; the constant L_V scales roughly as

$$L_V/D \approx (.2 \pm .05)Fr^{1/3}, \tag{7.5}$$

as can be seen in Fig. 7.12(f). At the lowest Re simulated, i.e., $Re = 5 \times 10^3$, the growth of L_V resumes at $x/D \approx 100$, a sign that the wake has entered the Q2D regime where the wake resumes expansion in the vertical again, via viscous diffusion (Spedding, 1997).

7.4 Turbulence diagnostics

7.4.1 Buoyancy-driven shear

As examined in §7.2, a key feature of the flow dynamics during the NEQ regime is the buoyancy-driven Kelvin-Helmholtz (K-H) instability events, whose intensity and persistence are found to be highly Re-dependent. Here such a dependence is quantified using the local Richardson number Ri_{loc} which is defined as:

$$Ri_{loc} = \frac{\frac{-g}{\rho_0}\frac{\partial \rho_T}{\partial z}}{(\frac{\partial u}{\partial z})^2 + (\frac{\partial v}{\partial z})^2}, \tag{7.6}$$

where $\rho_T = \bar{\rho}(z) + \rho'(x, y, z, t)$ is the total density. Stability analysis (e.g., see Turner (1973)) suggests that K-H instabilities are likely to occur for $Ri_{loc} < 1/4$ for an isolated idealized shear layer, and Riley and de Bruyn Kops (2003) recommended that the spatially averaged $Ri_{loc} < 1$ as an approximate criterion for secondary instabilities and turbulence to develop on average throughout a turbulent flow. The horizontally averaged values of Ri_{loc} at the two xy-planes of maximum vertical shear are plotted in Fig. 7.13 as a function of Nt for all simulations. It is

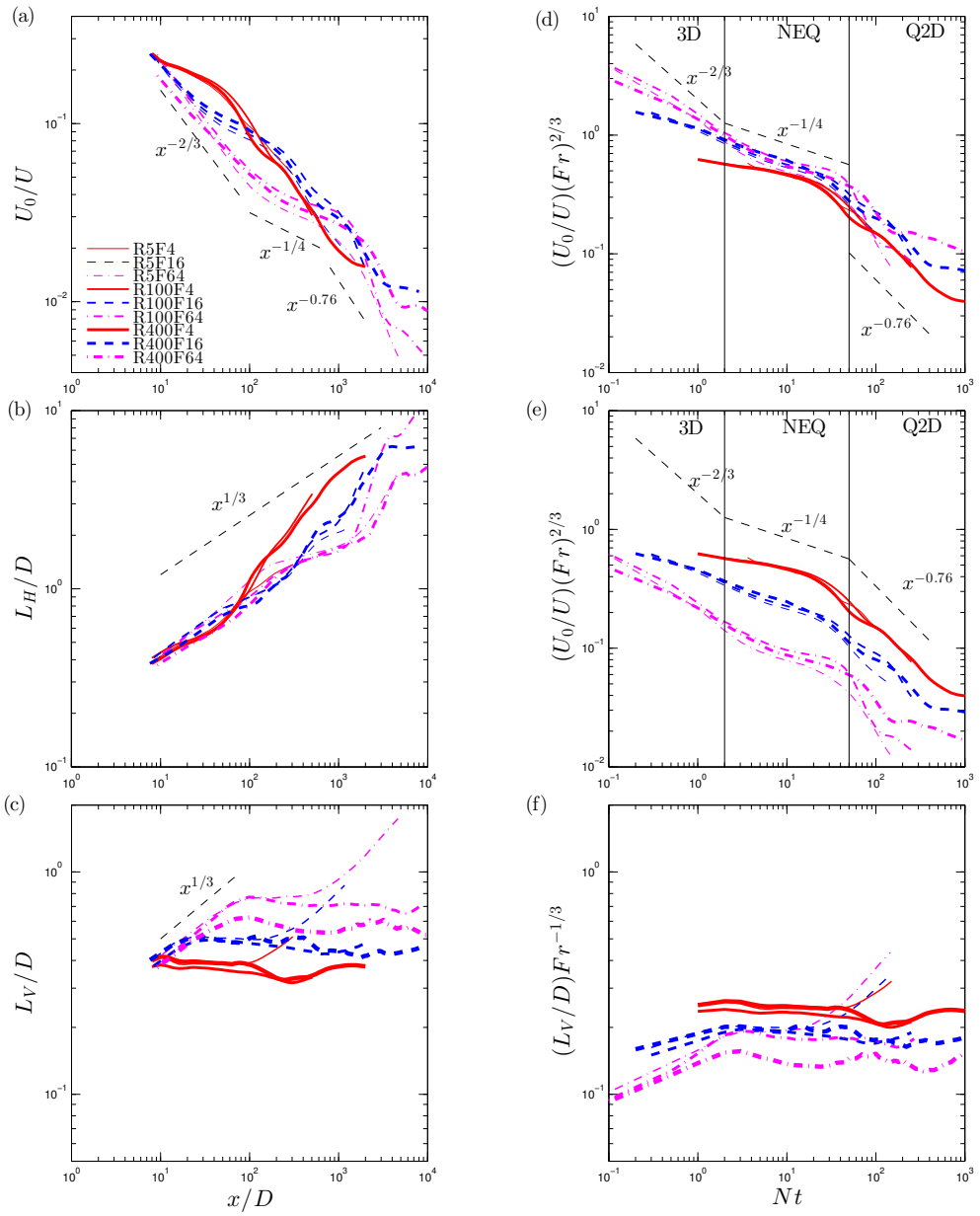

Figure 7.12: Evolution of mean centerline velocity, U_0, wake half-width, L_H, and half-height, L_V, for all simulations: (a) $U_0(x/D)$, (b) $L_H(x/D)$, (c) $L_V(x/D)$, (d) $U_0(Nt)$, (e) $U_0(Nt)$ with $Fr = 16$ and 64 rescaled by factors of 0.4 and 0.16, respectively, and (f) $L_V(Nt)$. Dashed lines represent power laws observed in the laboratory experiments of Spedding or proposed by Meunier *et al.* (2006). Line legend is given in (a). The thin vertical lines delineate transition points between regimes as identified in the low-Re experiments of Spedding (1997).

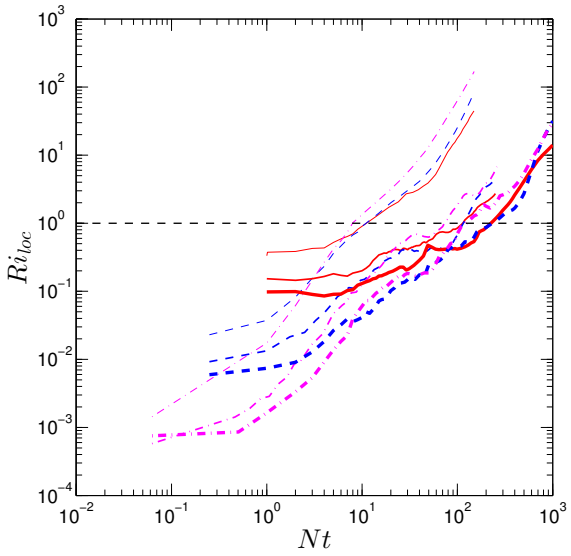

Figure 7.13: Evolution of the wake volume-based local Richardson number, Ri_{loc}. Line legend is the same as Fig. 7.12.

interesting to identify the time at which the average Ri_{loc} exceeds the critical value of unity marking the transition from unstable buoyancy-driven shear layers to a stable state. At a certain Fr, the flow stabilizes at a later Nt at a higher Re: e.g., for $Fr = 4$, the average Ri_{loc} crosses the threshold at $Nt \approx 10, 115$ and 220 for R5, R100 and R400 respectively. This is consistent with the qualitative observations in §7.2 focusing on the vortical structures on the xz plane (see Fig. 7.11) and is one of the key aspects of the Re effects on the localized stratified turbulent flow dynamics.

7.4.2 Buoyancy Reynolds number and turbulent length scales

As reviewed in §1.3, the theoretical scalings of stratified turbulence, e.g., as discussed by Brethouwer *et al.* (2007), are developed based on two dimensionless

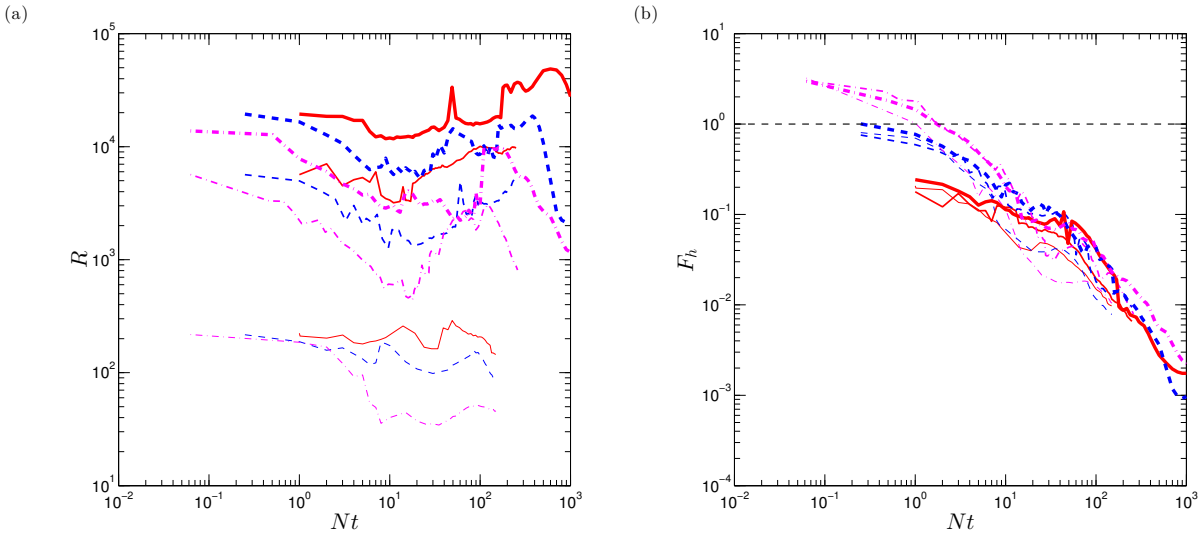

Figure 7.14: Evolution of (a) horizontal Reynolds number, R, and (b) horizontal Froude number F_h. Line legend is the same as Fig. 7.12.

parameters defined on the horizontal plane, i.e., the horizontal Reynolds number $R \equiv U_h \ell_h / \nu$ and Froude number $F_h \equiv U_h/(\ell_h N)$. The time evolution of these two parameters in the stratified wakes are shown in Fig. 7.14. The specific definitions of U_h and ℓ_h follow those used by DSD, i.e., U_h is defined as the average of rms values of horizontal fluctuating velocity computed over the two planes of maximum vertical shear, and ℓ_h is computed from the zero-crossing of the autocorrelation function based on fluctuating u velocity and vertical vorticity ω_z (see (5.4) of DSD). As can be seen in Fig. 7.14, the horizontal Reynolds number R turns out to be highly *Re*- and *Fr*-dependent and undulates weakly in time for a fixed *Re* and *Fr*; the horizontal Froude number F_h exhibits strong *Fr*-dependence in early wake (at $Nt < 10$) and decays significantly in time, indicating an increasingly strong buoyancy influence over the turbulent flow.

A key metric of dynamical state[4] of stratified turbulence is the buoyancy

[4]For example, $\mathcal{R}$ measures the scale separation between the largest horizontal scale that can overturn, i.e., the Ozmidov scale $\ell_o \equiv (\varepsilon/N^3)^{1/2}$, and the Kolmogorov scale η. According to

Reynolds number, $\mathcal{R} \equiv \varepsilon/(\nu N^2)$. As discussed in §1.3, the magnitude of $\mathcal{R}$ may determine whether the inviscid or viscous scaling applies to determine the vertical scale of the turbulence: For $\mathcal{R} > 1$, the flow follows an inviscid scaling, which was first proposed by Billant and Chomaz (2001); and for $\mathcal{R} < 1$, a viscous scaling (Godoy-Diana *et al.*, 2004) prevails. Moreover, $\mathcal{R}$ is a key parameter for the prediction of vertical (diapycnal) mixing and transport coefficients for oceanographic applications (e.g., Ivey *et al.* (2008)), which will be discussed further in §7.4.3. One of the limitations of our numerical scheme is that direct estimates of the dissipation rate ε is not feasible due to the lack of an explicit SGS model; however, $\mathcal{R}$ has been shown by Hebert and de Bruyn Kops (2006) to be equivalent to RF_h^2, and the latter representation is employed here to estimate $\mathcal{R}$ from our implicit LES data.

RF_h^2, as an approximation to the buoyancy Reynolds number $\mathcal{R}$, is plotted as a function of Nt for all simulations in Fig. 7.15(a). For $Re = 5 \times 10^3$, $\mathcal{R} \approx RF_h^2 > 1$ holds for only up to $Nt \approx 10$; as Re increases, the occurrence of the transition gets delayed, i.e., for $Re = 10^5$ and 4×10^5, $\mathcal{R} \approx RF_h^2$ crosses the critical value of unity at $Nt \approx 150$ and $Nt \approx 300$ respectively. Fig. 7.15(b) confirms the scaling of $RF_h^2 \sim Ri_{loc}^{-1}$ observed by Hebert and de Bruyn Kops (2006). The effect of Re on the time evolution of buoyancy Reynolds number $\mathcal{R}$, as approximated by RF_h^2, is consistent with the observations by DSD for Re up to 10^5. As can be seen in Fig. 7.16, the curves collapse when rescaled by the wake Reynolds number Re.

With the time evolution of $\mathcal{R}$ having been examined, one can proceed with testing the inviscid and viscous scalings of the vertical length scale in the two distinct regimes characterized by $\mathcal{R}$, at various stages of the wake evolution. Previously reported evidence for the two scalings has been typically obtained from *homogeneous* turbulence driven by constant *forcing* applied at the low wavenumber modes (large

Riley and Lindborg (2012), $\ell_o/\eta \sim \mathcal{R}^{3/4}$.

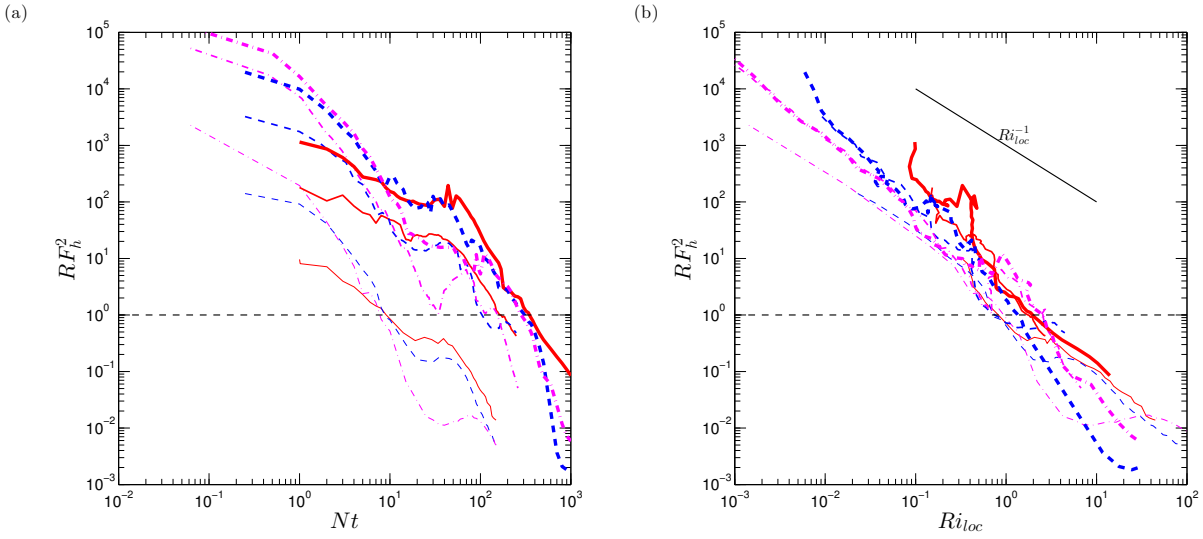

Figure 7.15: (a) Evolution of RF_h^2. (b) RF_h^2 as a function of Ri_{loc}. The dashed line represents the -1 power law observed by Hebert and de Bruyn Kops (2006). Line legend is the same as Fig. 7.12.

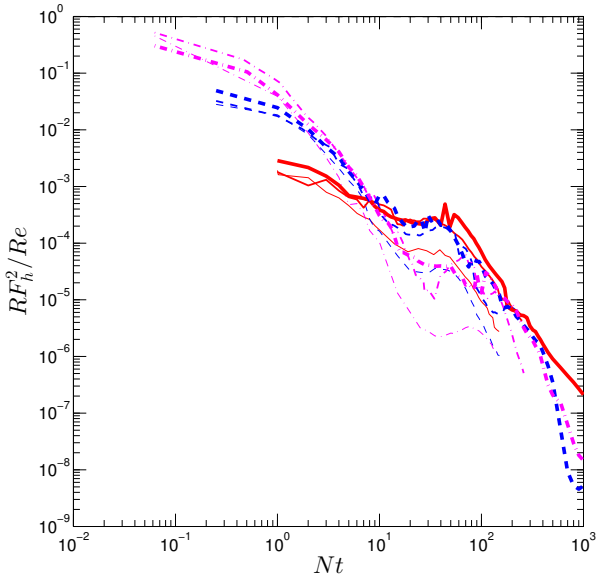

Figure 7.16: Evolution of RF_h^2 which is rescaled by the wake Reynolds number Re.

scales), e.g., Brethouwer *et al.* (2007); the particular significance of our results here is that we study an *inhomogeneous*, *localized*[5] and *temporally evolving* stratified turbulent flow which undergoes a natural life cycle that is typical of oceanic turbulent events which are often localized and episodic, e.g., as reviewed by Ivey *et al.* (2008). As pointed out by Riley and Lindborg (2012), the necessary conditions for both inviscid and viscous scalings to hold is that $F_h \to 0$ and $R \gg 1$; visual inspection of Fig. 7.14 suggests that both conditions are met after $Nt \approx 10$, where $F_h \to 0$ is $O(0.1)$ or lower and R remains considerably high. Fig. 7.17 shows the time evolution of horizontal and vertical integral length scales ℓ_H and ℓ_V, where the latter is specifically computed via[6]

$$\ell_V^2 = \frac{\langle u^2 + v^2 \rangle_{xy}}{\langle (\frac{\partial u}{\partial z})^2 + (\frac{\partial v}{\partial z})^2 \rangle_{xy}}, \tag{7.7}$$

following the definition by Riley and de Bruyn Kops (2003). As Fig. 7.17(a) suggests, ℓ_H depends only weakly on Re or Fr and grows gradually from $O(D)$ to $O(10D)$ from $Nt = 10$ to 1000; as in Fig. 7.17(b), ℓ_V, which is about one order of the magnitude smaller than ℓ_H, decreases distinctly with Re and increases with Fr. These results agree well with the qualitative observations made in §7.2 by visually examining the vortical structures within the flow.

Fig. 7.18 examines the validity of the viscous scaling (Godoy-Diana *et al.*, 2004) which predicts the vertical-to-horizontal aspect ratio of the turbulence Taylor scales to follow

$$\ell_V/\ell_H \sim R^{-1/2},$$

which is similar to the dynamics of a laminar boundary layer (Kundu and Cohen, 2008). Should this scaling work, the $(\ell_V/\ell_H)R^{1/2}$ is to approach a constant as soon

[5]In the sense that the vertical extent of the wake flow is confined and set by the initial conditions of the simulation, in contrast to the triply periodic set-up typical of DNS studies, where the vertical extent of the flow is infinite.

[6]Operator $\langle . \rangle_{xy}$ denotes an average on the two xy planes with maximum vertical shear both above and below the wake centerline.

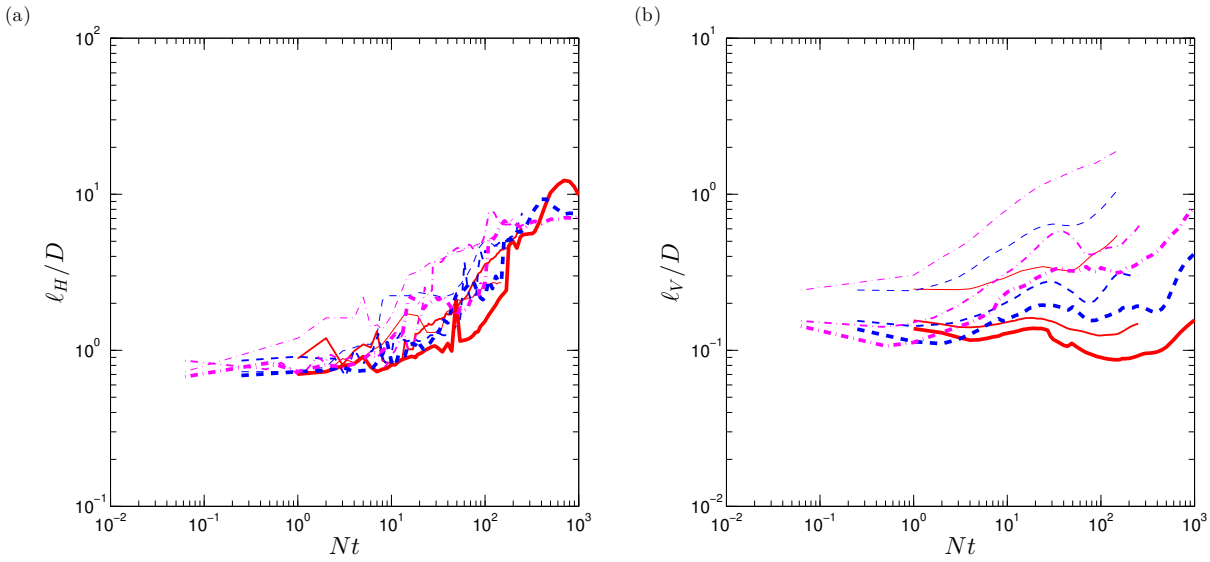

Figure 7.17: Evolution of (a) horizontal length scale ℓ_H and (b) vertical length scale ℓ_V. Line legend is the same as Fig. 7.12.

as $\mathcal{R} \approx RF_h^2$ drops below 1 and F_h drops below $O(0.1)$, both of which are met for the $Re = 5 \times 10^3$ case after $Nt \approx 10$. It can be seen from Fig. 7.18 that the corresponding $(\ell_V/\ell_H)R^{1/2}$ values at $Re = 5 \times 10^3$ are $O(1)$ and decays/undulates only weakly in time, which seems to be consistent with the viscous scaling. Similar behavior of ℓ_V was also reported by Riley and de Bruyn Kops (2003) (see their Fig. 6(b)) in their DNS of arrays of Taylor-Green vortices subject to stable stratification. At the two higher wake Re's examined, the value of $(\ell_V/\ell_H)R^{1/2}$ is seen to decay sharply in time during the NEQ regime until the value flattens out noticeably in the late wake where $\mathcal{R} \approx RF_h^2$ drops below 1, i.e., after $Nt \approx 300$ for the $Re = 4 \times 10^5$ cases, which also lends support to the viscous scaling in the $\mathcal{R} < 1$ regime.

Fig. 7.19 examines the validity of the inviscid scaling (Billant and Chomaz, 2001) which predicts the vertical integral length scale ℓ_V to follow

$$\ell_V \sim U_h/N.$$

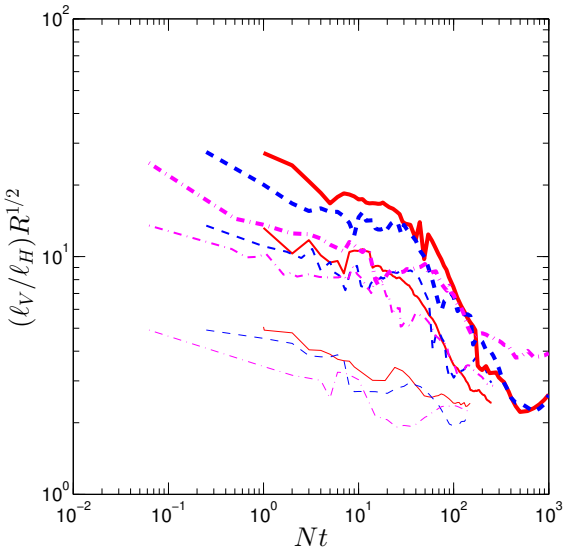

Figure 7.18: Test of the viscous scaling of $\ell_V/\ell_H \sim R^{-1/2}$. Line legend is the same as Fig. 7.12.

Divided by ℓ_H on both sides, the above relation can be rewritten as

$$\ell_V/\ell_H \sim U_h/(\ell_H N) = F_h,$$

which means that the aspect ratio scales linearly with F_h. The requirements for this scaling are that $\mathcal{R} > 1$ and $F_h \ll 1$, which are met by the two higher Re's examined here after $Nt \approx 10$ and until $Nt \approx 150$ and $Nt \approx 300$ respectively for R100 and R400. Fig. 7.19 suggests that within the above ranges of Nt, the corresponding $\ell_V \sim U_h/N$ values do collapse into an $O(1)$ quantity (independent of Re or Fr) that grows very weakly with Nt, and this agrees satisfactorily with the inviscid scaling. The $\ell_V \sim U_h/N$ value starts to grow strongly again beyond a certain value of Nt, presumably due to increasingly important viscous effects as $\mathcal{R}$ decreases. The point of departure from the collapsed segment in Nt seems to get delayed for the R400 cases as compared to the R100 cases. The R5 cases seem to depart from the higher Re cases, which is expected because when the buoyancy control has established ($F_h \ll 1$) for the R5 flows, $\mathcal{R}$ has already dropped below unity, and the requirements for the inviscid scaling are never simultaneously met.

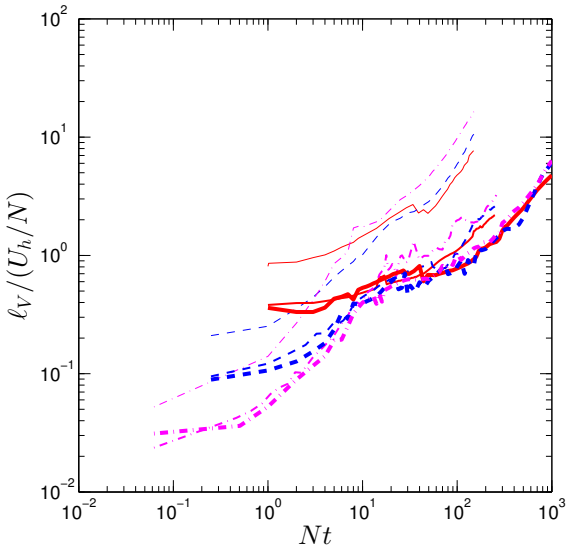

Figure 7.19: Test of the inviscid scaling of $\ell_V \sim U_h/N$. Line legend is the same as Fig. 7.12.

7.4.3 Turbulent viscosities

Meunier *et al.* (2006) (hereinafter referred to as "MDS") developed a predictive self-similarity model for mean wake evolution based on laboratory findings by Spedding (1997, 2001, 2002). The model produced decent agreement with experimental and, available at that time, numerical observations at $Re \approx O(10^4)$. However, there are a few assumptions in the MDS model which require further verification: First, MDS assumed that all vertical transport in the wake ceases upon entry into the NEQ regime at $Nt \approx 2$ where F_h is $O(1)$ or lower; second, it was assumed that in the horizontal direction, the turbulent viscosity ν_H corresponds to a turbulent Reynolds number $Re_{T,H} = U_0 L_y/\nu_H$ of a constant value 4, a result that was reported from experiments on *unstratified* sphere wakes by Bevilaqua and Lykoudis (1978). The major objective of this section is to quantify the turbulent viscosities in both horizontal and vertical directions from the implicit LES data, which tests the above key assumptions behind the MDS model and seeks possibilities of

refining them.

Horizontal turbulent viscosity

The horizontal turbulent viscosity ν_H can be estimated by least-squares fit to the gradient-diffusion model

$$\langle u'v' \rangle = -\nu_H \frac{\partial \langle u \rangle}{\partial y} \tag{7.8}$$

at each value of Nt, where $\langle u'v' \rangle$ and $\langle u \rangle$ can be obtained from the implicit LES data by taking the x-average at each (y, z) location. A linear regression can be performed on the scatter plot of $\langle u'v' \rangle$ versus $\partial \langle u \rangle / \partial y$, at any given time, to determine the instantaneous value of turbulent transport coefficient ν_H. The quality of such linear fit varies with time, stronger in early wakes where the turbulence is more energetic and the correlation becomes much weaker at $Nt > 100$ where pancake vortices start to dominate the flow; only the time instances at which the coefficient of determination exceeds a threshold of 0.6 are included in the plots in Fig. 7.20. Tennekes and Lumley (1972) introduced two approaches through which ν_H can be normalized/parameterized, and they are both implemented in Fig. 7.20. In the first approach, ν_H is normalized by the instantaneous *mean* maximum centerline velocity U_0 and wake width L_H, which produces the reciprocal of turbulent Reynolds number $1/Re_{T,H} = \nu_H/(U_0 L_H)$. Fig. 7.20(a) suggests that $\nu_H/(U_0 L_H)$ varies with both Nt and Fr, and to a lesser extend, with Re. The MDS model used a constant $1/Re_{T,H}$ value of 1/4, which overestimates ν_H and ignores any dependence on Nt and Fr. In the other approach, ν_H is normalized by an alternative set of velocity and length scales (u_*, ℓ_*), where

$$u_*^2 \equiv \max(-\langle u'v' \rangle),$$

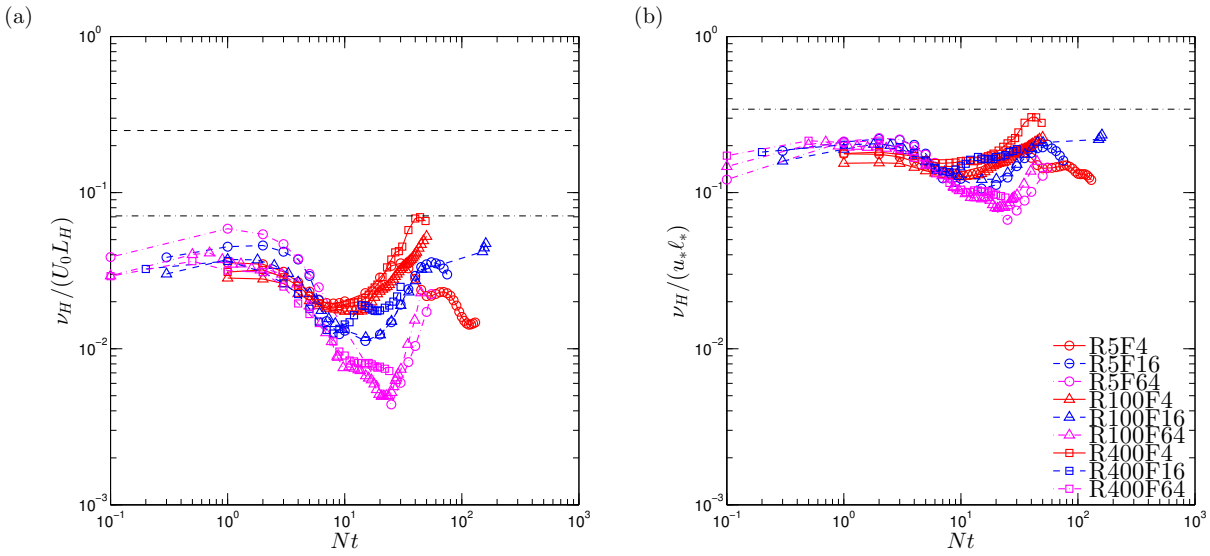

Figure 7.20: (a) Horizontal turbulent viscosity ν_H normalized by $U_0 L_H$, as a function of Nt, and (b) ν_H normalized by $u_* \ell_*$. In (a), dash line corresponds Bevilaqua and Lykoudis (1978)'s proposed turbulent Reynolds number value of $Re_{T,H} = 4$, and dash-dot line denotes Tennekes and Lumley (1972)'s $Re_{T,H}$ value of 14.1; both values are for an axisymmetric wake in a unstratified fluid. In (b), dash-dot line denotes $\nu_H/(u_* \ell_*) = 1/2.92$ as given by Tennekes and Lumley (1972) for unstratified axisymmetric wake.

is a *turbulent* velocity scale and

$$\ell_* \equiv \frac{U_0}{\max(\partial \langle u \rangle / \partial y)} e^{-1/2},$$

following (4.5.1) and (4.5.2) of Tennekes and Lumley (1972) respectively. In Fig. 7.20(b), the scattering of data in Nt has been reduced by using the alternative normalization (u_*, ℓ_*) but has not vanished completely.

Vertical turbulent viscosity

Similarly, the vertical turbulent viscosity ν_V can be estimated by least-squares fit to the gradient-diffusion model

$$\langle u'w' \rangle = -\nu_V \frac{\partial \langle u \rangle}{\partial z} \tag{7.9}$$

at each value of Nt. The quality of these fits are in general not as strong as their horizontal counterparts, and only the time instances at which the coefficient of determination exceeds a threshold of 0.5 are included in the plots in Figs. 7.21 and 7.22. As shown in Fig. 7.21, globally (over the wake core), there is vertical turbulent transport at the higher Re's well after $Nt \approx 2$, which persists up to $Nt \approx 10$, in contrast to MDS's assumption of zero vertical mean momentum transport beyond $Nt = 2$ which might be justified for only low-Re wakes. The absence of any data beyond the point $Nt = 10$ in Fig. 7.21 corresponds to a less well-defined correlation between vertical turbulent momentum flux and vertical mean shear; individual Kelvin-Helmholtz events, nevertheless, are expected to promote local vertical transport. The magnitude of ν_V, when normalized by $U_0 L_V$ to produce the reciprocal of turbulent Reynolds number $1/Re_{T,V} = \nu_H/(U_0 L_V)$, has comparable magnitude and follows similar time evolution pattern to its horizontal counterpart in Fig. 7.20(a).

A robust parameterization of the turbulent transport coefficient in the vertical has been the focal point of oceanographic research, e.g., as reviewed by Ivey *et al.* (2008). Here we report attempts to parameterize the measured ν_V in early wakes ($Nt < 10$) as a function of buoyancy Reynolds number $\mathcal{R}$ which is approximated by RF_h^2. Shih *et al.* (2005) measured ν_V through DNS of *forced homogeneous* stratified turbulence subject to a constant vertical shear at $0.5 < \mathcal{R} < 1000$. One can also resort to the conventional approach in the physical oceanography literature

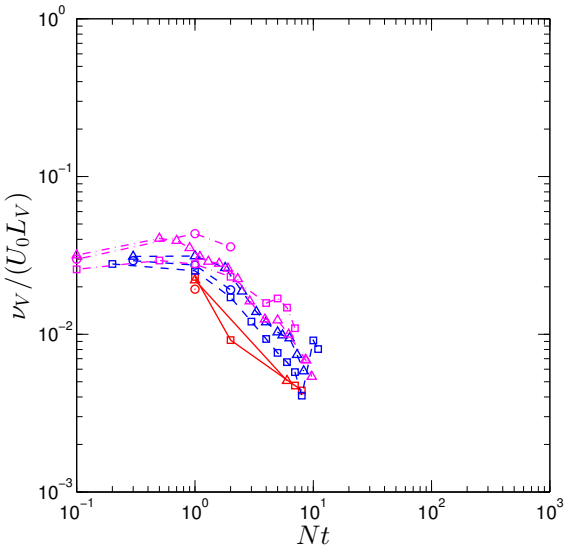

Figure 7.21: Vertical turbulent viscosity ν_V normalized by $U_0 L_V$, as a function of Nt. Legend is the same as Fig. 7.20. Rare cases of negative values of ν_V, indicative of counter-gradient transport, often correspond to lower values of coefficients of determination and are ignored in this plot and in Fig. 7.22.

(Osborn, 1980) to estimate the diapycnal diffusivity κ_ρ as (see Ivey *et al.* (2008) (5))

$$\kappa_\rho = \Gamma \frac{\varepsilon}{N^2}$$

where Γ is the mixing efficiency and can be assumed to be a typical value of 20% (e.g., as discussed by Peltier and Caulfield (2003)). If one is to further assume that the turbulent Prandtl number $Pr_T = \nu_V/\kappa_\rho$ is unity[7], ν_V can be approximated as

$$\nu_V \approx \kappa_\rho = 0.2 \frac{\varepsilon}{N^2}$$

Fig. 7.22 compares the wake measurements shown in Fig. 7.21 to Shih *et al.* (2005) and the Osborn model by assuming $\Gamma = 20\%$ and $Pr_T = 1$. It appears that the canonical Osborn model matches the wake measurements up to $\mathcal{R} \approx 100$, beyond which point the model tends to overestimate the total viscosity; however,

[7]More sophisticated models for Pr_T for homogeneous stably stratified turbulence can also be found, e.g., in Venayagamoorthy and Stretch (2010).

in the range where the Osborn model and Shih *et al.* (2005) match each other, i.e., $10 < \mathcal{R} < 100$, no significant correlation between vertical turbulent momentum flux and vertical mean shear is observed in the wake flow (and thus no data points in this range of $\mathcal{R}$). Note that the Osborn model assumes an equilibrium state of turbulent kinetic energy (TKE), i.e., $\partial\langle u_i'^2\rangle/\partial t = 0$ and neglects any transport of TKE by the mean flow (Ivey *et al.*, 2008); the applicability of canonical models of this kind to the *unstationary* and *inhomogeneous* wake flow may require certain caution. Moreover, the physical reason as to why the gradient-diffusion model, i.e., (7.8) and (7.9), fails to describe the momentum transport beyond certain Nt value in the intermediate/late wake also deserves further study. Finally, it is unclear how the dynamical role that the secondary K-H instability events and the subsequent turbulence may play, in terms of driving mean momentum flux in the vertical to affect the mean flow evolution within the wake.

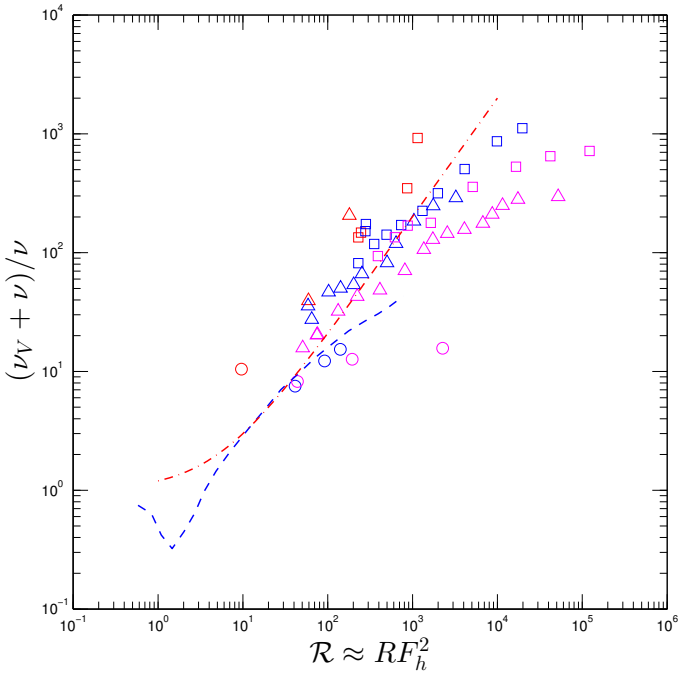

Figure 7.22: Total (turbulent plus molecular) vertical momentum diffusivity (normalized by molecular viscosity ν) as a function of RF_h^2, the latter as an approximation to the buoyancy Reynolds number $\mathcal{R}$. Symbol legend is the same as Fig. 7.20; blue dash line denotes data extracted from Fig. 2 of Shih *et al.* (2005), and red dash-dot line denotes the Osborn model $\nu_V \approx \kappa_\rho = 0.2\varepsilon/N^2$.

CHAPTER 8

CONCLUDING REMARKS AND FUTURE WORK

8.1 Nonlinear effects in internal waves

8.1.1 Eulerian

By means of direct numerical simulation, we have studied the nonlinear dynamics, i.e., mean-flow and harmonic generation, that occur in the region where a finite-amplitude IW beam is reflected off a free-slip surface (§4). The mean flow forms a layered structure in the subsurface region, which induces mean shear. The relative strength of the mean flow to the wave is found to scale linearly with the wave amplitude and increase with the phase-tilt angle of the beam with respect to the vertical, while remaining independent of the compactness of the beam and the particle-based Reynolds number. These basic findings agree well with (Tabaei *et al.*, 2005) (TAL), who formulated a weakly nonlinear and inviscid theory, whereas our simulations are fully nonlinear and viscous.

In terms of determining the relative mean-flow strength $\mathcal{M}$, although it is assumed that their amplitude parameter being small ($\epsilon \ll 1$), TAL's solution seems to be applicable to the full range of wave amplitudes that we have simulated. On the other hand, various instabilities can occur in IWs of steepness A on the order of 1 to 10% ($\epsilon \sim 10^{-3}$), as seen in the marginal stability curves (Sutherland, 2010) of IWs and our own observations in §4. Therefore, it is very likely that weakly nonlinear theory of TAL is valid for the full range of amplitudes under which a wave remains stable.

The role that viscosity plays in this flow is a subtle one. First of all, the nonlin-

ear dynamics in the reflection zone, at least in terms of mean flow, do not seem to depend on viscosity. This is because gravity, and not viscous effects, is the major counter-balancing force to nonlinearity *locally* in the reflection region. Additionally, nonlinear effects are strongly dependent on the wave amplitude, whereas in a viscous medium the wave's amplitude is progressively damped as it propagates. In the *global* picture, as one observes an IW beam propagating from its source to ultimately get reflected off the surface, the viscous effect has to be taken into account as it determines the *in-situ* amplitude of the wave that is dynamically relevant to the nonlinear effects. This is particularly important to note when interpreting the nonlinearity of IWs in experimental and numerical settings, where the Reynolds number is finite.

The evolution of the mean flow induced by an IW can often be studied by applying the wave Reynolds stress model (Sutherland, 1996; Zikanov and Slinn, 2001; Abdilghanie and Diamessis, 2012), which relates the growth of mean flow, say $\partial\langle u\rangle/\partial t$, to the divergence of Reynolds stress, say $\partial\langle uw\rangle/\partial z$. However, we have shown in Appendix A, via application of TAL's solution to a plane wave (see in Appendix A), that the steady-state mean flow (see (A.13)) can exist in the absence of Reynolds stress gradients, as is the case for a plane IW reflection. This suggests that the Reynolds stress model might be useful to describe the transient in a mean flow development but not in steady-state counterpart as in the present study, where we expect the divergence of Reynolds stress to be balanced by the mean gradients of dynamic pressure.

An IW beam inherently contains a limited number of wavelengths included within the wave amplitude envelope. In the present study, we have considered only *quasi-monochromatic* waves (Sutherland, 2010), waves for which the envelope

size is greater than or at least comparable to the wavelength. It has been shown that, for this class of waves, the beam compactness does not affect the nonlinear dynamics observed during reflection, such as the amplitude of wave-induced currents. Additional simulations we have performed (not reported here) have also examined even more compact beams than those presented in this manuscript, with envelope half-with σ_{sfc} as small as $0.49\lambda_x$; the corresponding observations on reflection-induced mean flow are all consistent with the broader beams examined in detail. Note that we have not been able to generate robust beams with even greater compactness (i.e., $\sigma_{sfc}/\lambda_x < 0.49$), where apparently the quasi-monochromatic assumption is no longer valid.

From the engineering point of view, i.e., remote sensing of surface signature of IW activities, open questions remain as to the extrapolation of these results to a more realistic oceanic situation. One outstanding concern of such kind is the applicability of the free-slip rigid-lid top boundary condition in our numerical set-up to represent physical condition of ocean surface. This particular boundary condition implies that the top surface is stress-free and is not allowed to displace vertically. The former restriction can be justified when considering the free surface of a calm ocean or laboratory tank surface, where the surface tangential stress is negligible. The latter condition is linked to the magnitude of the vertical displacement induced by the internal wave field relative to the characteristic horizontal length scale of the wave as manifested at the surface; a small surface "slope" is expected for the rigid lid to be valid. Moum and Smyth (2006) reported strongly nonlinear internal solitary waves which induce surface displacement of $O(1$ cm$)$ over a wave length scale of $O(100$ m$)$, hence a surface slope of $O(10^{-5})$ to $O(10^{-4})$. Following Moum and Smyth's pressure disturbance model, we have estimated the surface slope induced by the reflecting internal waves in the present study to be

no greater than $O(10^{-5})$, and the rigid-lid approximation is thus justified.

Some preliminary attempts have been made in this study to examine the role of a subsurface mixed layer on reflection dynamics. The base of the mixed layer is found to act similarly to a free-slip surface in terms of generating mean flows. Additionally, the mean flow magnitude at the surface is significantly diminished in the presence of a mixed layer.

8.1.2 Lagrangian

Following what has been presented in §5 on the Lagrangian flows within reflecting IWs, a relevant topic of discussion are the possible extensions of this study to realistic oceanic conditions. In this dissertation, a uniform stratification in the water column and a free-slip surface at the upper boundary are considered. This combination may, at first glance, seem to be a simplistic configuration, but it serves as a very important first step towards exploring more complex and realistic conditions. First, uniform stratification allows one to isolate the effects of nonlinear wave reflection, a canonical scenario of wave-wave interaction; the extension of this Lagrangian study to more realistic oceanic set-ups taking into account the various dynamics due to IW interaction with a variable environment (stratification profile and background flows) certainly deserve further research efforts. Second, it was found out by Z&D (Zhou and Diamessis, 2013) that a free-slip boundary acts very similarly to the base of a mixed layer in terms of the dynamics of mean flow generation — the applicability of the results shown here can in fact be much broader than the sole case of reflection off the sea surface.

An important observation in this work is the strong sensitivity of the nonlinear

Lagrangian effects to beam angle θ, i.e., the empirical scalings of $U_L/c_x \propto \tan^2\theta$ and $K_x/(\lambda_x^2/T) \propto \tan^4\theta$, at a given wave steepness A. In reality, oceanic IW beams (Cole *et al.*, 2009) of tidal origins tend to have fairly large values of θ, i.e., $\theta > 85°$, and thus high hydrostaticity (Sutherland, 2010). The very shallow angles of these oceanic tidal IW beams can make them very prone to generating Lagrangian mean flows upon reflection, as our results suggest. However, a word of caution here is that these relatively low-frequency IW beams may also be subject to the effect of the Earth's rotation, which needs to be accounted for in a complete analysis. In addition, oceanic tidal IW beams of shallow angles may generate more energetic propagating higher harmonics that may induce significant net Lagrangian effects of their own, which could be another important difference in the realistic oceanic situation.

Extension of the results from a free-slip reflecting surface to a no-slip one may require some extra caution. Laboratory measurements of mean flows within reflecting beams off a no-slip solid slope (Leclair *et al.*, 2011; Grisouard *et al.*, 2013) suggest qualitatively different results of the mean-flow structure than those reported in Z&D, which is expected to be a result of the three-dimensional configuration of the experiments (L. Gostiaux, pers. comm.). Rodenborn *et al.* (2011) also reported discrepancy with the TAL theory (Tabaei *et al.*, 2005) in terms of harmonic generation at a solid bottom slope. It is to note that both leading-order wave (B.15) and Eulerian mean (B.14) in the inviscid solution satisfy the free-slip boundary condition automatically, which makes the small-amplitude solution directly applicable to the analytical inviscid treatment of our problem, but not the one with a no-slip surface. Under the no-slip condition, viscous/dissipative effects are expected to be even more important near the wall, adding another layer of complexity. Therefore, the formulation of these inviscid theories needs to be adapted

for the no-slip configurations. How the reflection-induced Lagrangian dynamics may be altered in such a highly dissipative near-bottom region remains an open question.

8.2 Surface-manifestation of turbulence-emitted internal waves

A complete and systematic characterization of the surface signatures of internal waves emitted by localized stratified turbulence, prototyped by a towed-sphere wake, has been performed in this study (§6). The most striking result might be that the time variation of the conditionally averaged dimensionless wavelength $\overline{\lambda}_H/D$ vs. Nt *at a fixed distance* (in our case, at the sea surface) from the turbulent wave source is universal in wake parameters (Re, Fr). This result gives rise to the potential of correlating surface observations of IWs to the age of the underlying wave-emitting turbulence in Nt, an inference that can be achieved without the full knowledge of the wake parameters Re and Fr, provided that the depth of the turbulent wave source is given. This universality of the time evolution of wavelength in (Re, Fr) relies on the fact that linear theory works well for these turbulence-radiated waves in their far-field propagation. The *virtual* origin of these waves, which is independent of the wake parameters, has been determined. The linear propagation model with the calibrated virtual origin enables the prediction of the prevalent wavelength at a given space and time in the far-field and may assist the interpretation of surface observation of these waves. On the other hand, Fr- and Re-dependence does play a critical role in determining the most energetic wavelength $\hat{\lambda}_H$ (and consequently the Nt or X/D at which this wavelength reaches

the surface); a $Fr^{1/3}$-scaling for $\hat{\lambda}_H/D$ and a considerable decrease of this wavelength with Re are observed. This scaling coincides with that of the vertical Taylor scale of the wake turbulence. Wave dispersion, both in wavenumber and frequency domains, seems to be the dominating physical process in the wake's far-field, in the absence of a variable background stratification and mean-flow profile. At the higher Re examined, the delay of the most intense wave impact in time at a fixed distance to the wake, seems to be caused by the reduction of the most energetic wavelength $\hat{\lambda}_H$ emitted by the turbulence and thus the reduction of the waves' group velocity; this mechanism is in contrast to A&D's hypothesis that it is secondary turbulence in the NEQ wake which produces these waves that appear at a later Nt. This observation motivates a reconsideration of the nature of IW generation by evolving stratified turbulence, i.e., whether the generation is confined at the early stages of NEQ regime, with the energy content of the waves increasing with Re, or it is persistent throughout the entire NEQ regime. The potential for generation of surface slicks and divergence patterns in the long-term Lagrangian transport at the surface is for the first time discussed for obliquely propagating IWs.

8.3 High *Re* localized stratified turbulence

In §7, preliminary analyses have been performed on a set of stratified turbulent wake data obtained by implicit large-eddy simulations (LES). The LES examine stratified wakes at $Re \in \{5 \times 10^3, 10^5, 4 \times 10^5\}$ and $Fr \in \{4, 16, 64\}$, and the analyses focus on the vortical structures within the wake, evolution of mean flow, turbulent length scales and turbulent viscosities. The key finding is that, consistent with the results of Diamessis *et al.* (2011), the wake Reynolds number Re has a

significant impact on the evolution of the dynamically critical buoyancy Reynolds number, $\mathcal{R}$, i.e., as Re increases, the $\mathcal{R}$ at a given dimensionless time Nt is higher, and thus the transition from the *strongly stratified turbulence* regime at $\mathcal{R} > 1$ to the *viscosity-affected stratified flow* (inviscid) regime at $\mathcal{R} < 1$[1] is delayed to a higher value of Nt (see Fig. 7.15(a)). As $\mathcal{R}$ is found to be linked to the local Richardson number $\mathcal{R} \sim Ri_{loc}^{-1}$ (Hebert and de Bruyn Kops, 2006), the delay of $\mathcal{R}$ dropping below $O(1)$ implies a delay of Ri_{loc} reaching beyond $O(1)$, the latter being the requirement for the buoyancy-driven shear layers to restabilize (Riley and de Bruyn Kops, 2003). The prolongation of shear instabilities due to higher $\mathcal{R}$ in a higher-Re wake during the NEQ regime is confirmed through visual observations of the vortical structures and estimates of horizontally averaged Ri_{loc} (see Fig. 7.13). During both the inviscid and viscous regimes, the theoretical scalings of the vertical integral scale ℓ_V (Billant and Chomaz, 2001; Godoy-Diana *et al.*, 2004) seem to hold. In order to improve upon an existing self-similarity model of the mean wake evolution by Meunier *et al.* (2006), turbulent viscosities in both horizontal and vertical directions are estimated from the LES data set. The results question the validity of the constant turbulent viscosity in the horizontal direction and zero turbulent viscosity in the vertical (after $Nt = 2$) that were assumed by Meunier *et al.* (2006). When parameterized by the buoyancy Reynolds number $\mathcal{R}$, the vertical turbulent viscosity, albeit insignificant after $Nt \approx 10$ in the average sense (considering the bulk flow rather than the individual shear-instability event), seems to be comparable to the prediction by the canonical Osborn model (Osborn, 1980) for a range of $\mathcal{R}$ values.

[1]The terminology follows the classification of stably stratified flow by Brethouwer *et al.* (2007).

8.4 Future work

In terms of the **nonlinear effects within the waves (§4 and §5)**, it remains to be discovered how other more complex features typical of the oceanic environment, e.g., background shear, variable stratification, interaction with surface waves etc., can modify the nonlinear dynamics observed in this idealized setting that we have considered here. An additional level of complexity may be introduced when we incorporate spatial and temporal variability into the IW field which undergoes reflection, as is the case with the waves originating from a submerged stratified turbulent source, as discussed in §6. It remains unclear whether it is valid to model such waves with persistent quasi-monochromatic beams which are compact in streamwise (and spanwise) direction(s), or whether these turbulence-generated IWs are actually intermittent wave packets. In terms of IW-driven Lagrangian transport (§5), only two-dimensional and stable reflecting waves with no transient effects are considered in this study. Highly intriguing areas of future investigations include Lagrangian studies in laterally confined three-dimensional wave configurations (Bordes *et al.*, 2012; Kataoka and Akylas, 2013) and for IWs undergoing gradually growing instabilities such as PSI (Joubaud *et al.*, 2012; Bourget *et al.*, 2013; Zhou and Diamessis, 2013; Gayen and Sarkar, 2013).

In terms of **IWs emitted by stratified turbulence (§6)**, it is highly intriguing to study wave-turbulence interactions in the wake's near-field: How does turbulence choose the wavelength to be emitted? Moreover, as shown in §6.3.4, the turbulence has preferred orientations in which it emits waves and subsequently creates spatial patterns on the sea surface. However, the mechanism by which turbulence chooses the prevalent orientation of the emitted waves is unknown. For example, are there separate dynamic processes in the turbulent wake core which

are responsible for the two distinct emission angles (Fig. 6.13) respectively? A possibility is that the spatial orientation of the waves may correlate to that of the wave-generating coherent structure of the turbulence, which is intriguing and deserves further study.

It remains to be examined why the waves seem to be predominantly generated by the early wake: What is the optimal condition for the stratified turbulence to generate internal waves? Is it a question of the energy content of the wave-generating turbulence, or does also the distinct structural characteristics of the turbulence (e.g., the layered flow structure typical of stratified turbulence) play a role? If the latter is true, secondary turbulence could indeed become a considerable contributor to the wave field, presumably at even higher Re where the layering is more intense (Riley and de Bruyn Kops, 2003). These highly intriguing questions certainly warrant further study in the future. Future work at a higher Fr and/or Re is highly attractive but is currently restricted by computational power. It is also of interest to incorporate more realistic oceanic stratification and mean flow profiles in the subsurface and to take into account the interactions of the surface-approaching IWs with the near-surface processes.

In terms of the **Reynolds number effects in stratified wakes (§7)**: First, what are the key dynamical transition points that could be identified to refine the canonical 3D-NEQ-Q2D paradigm by Spedding (1997)? For example, when exactly does the wake enter the strongly stratified regime where local Froude number F_h is below $O(0.1)$? When exactly does $\mathcal{R} = 1$ occur, which marks the transition from the inviscid to the viscous sub-regime by Spedding (1997)? How do these transition points correspond to the 3D-NEQ and NEQ-Q2D transitions that are previously determined based on mean flow evolution?

Second, a reconsideration of the means towards quantifying the wake dimensions maybe necessary. While the height and width based on the assumed Gaussian profile of mean flows give one a convenient set of measures of the wake dimensions, are they still good metrics when the flow has re-organized into pancake vortices in the horizontal and shear layers in the vertical, a unique phenomenon under the effect of the stable stratification? Alternative measures based on the vorticity and dissipation fields (S. M. de Bruyn Kops, pers. comm.) may yield a more robust measure of the wake dimensions.

Moreover, in order to refine the self-similar model of the mean wake, how can one incorporate the turbulent viscosity measurements made in this dissertation into the model? Why does the gradient-diffusion model cease to be effective for the bulk flow beyond certain point in time, and how can one work around it in order to construct a more robust model the mean flow? What is the dynamical significance of the secondary shear instabilities in terms of affecting the mean flow evolution? How do turbulence-emitted internal waves act as a momentum sink and how significant is it?

Finally, how can one use the results acquired through the high-resolution LES data of *inhomogeneous* and *nonstationary* stratified turbulent flow in this dissertation to inform the development of more physically based sub-grid scale (SGS) model for stratified flows? A robust SGS model which allows coarser grid resolution without compromising the physics, may enable the LES modeling of higher-Re stratified turbulent flows at reasonable computational costs. Alternatives to the relatively more expensive LES could be second-order models, e.g., a Reynolds stress model that incorporates the buoyancy flux (S. B. Pope, pers. comm.). Implementing such models on localized stratified turbulent flows and comparing to LES/DNS

results can be interesting venues for future investigations.

APPENDIX A

WEAKLY NONLINEAR THEORY ON INTERNAL WAVE REFLECTION

In this Appendix, we apply the inviscid and weakly nonlinear solution given by Tabaei *et al.* (2005) (TAL) to obtain an understanding on the mean currents formed upon IW reflection. TAL describe the flow in terms of the dimensionless streamfunction ψ' in their (3.7):

$$\begin{aligned} \psi' &= \epsilon\{Q'(x',y')e^{-i\omega_0 t} + c.c.\} \\ &\quad +\epsilon^2\{Q'_0(x',y') + \cdots\} + O(\epsilon^3)\ . \end{aligned} \tag{A.1}$$

Here and elsewhere in this text, the superscript $'$ indicates dimensionless quantities following the scaling adopted by TAL and an earlier work by Tabaei and Akylas (2003). This length scale is chosen as to be "a characteristic length $\mathcal{L}$ associated with the waves" by Tabaei and Akylas (2003). We further specify $\mathcal{L}$ as the horizontal wavelength λ_x, i.e.,

$$\mathcal{L} \equiv \lambda_x = 2\pi/k, \tag{A.2}$$

and therefore the horizontal wavenumber is

$$k' = 2\pi/\lambda'_x = 2\pi, \tag{A.3}$$

The time scale $\mathcal{T}$ is taken as N^{-1}. It is implied that, based on the dimensionless momentum equation (2.3) in TAL, that their velocity scale scale should be chosen as $\mathcal{L}/\mathcal{T} = \lambda_x N$. The parameter ϵ in (A.1) is regarded "an amplitude parameter" without an explicit definition, based on wave field variables, having been offered. We shall revisit this parameter soon, although we wish to emphasize that it is critical to establish its connection with wave steepness A. Also note that TAL

uses a coordinate system in which $y = 0$ at the reflecting surface, and thus TAL's wall-normal spatial independent variable y is equivalent to $L_z - z$ in the present study.

The horizontal velocity u' is linked to the streamfunction ψ' by $u' = \psi'_{y'}$. Expressing u' in a similar expansion to (A.1) gives:

$$\begin{aligned} u' &= \epsilon\{U'(x', y')e^{-i\omega_0 t} + c.c.\} \\ &\quad +\epsilon^2\{U'_0(x', y') + \cdots\} + O(\epsilon^3) \ , \end{aligned} \tag{A.4}$$

where $U' \equiv Q'_y$ and $U'_0 \equiv Q'_{0y'}$, which represent the wave and mean components respectively. The temporal mean component of the streamfunction in given by (3.9a) in TAL:

$$\begin{aligned} Q'_0 &= \frac{i}{\sin\Theta} J(Q', Q'^*) \\ &= \frac{i}{\sin\Theta}(Q'_x Q'^*_y - Q'_y Q'^*_x) \ , \end{aligned} \tag{A.5}$$

where

$$\Theta = \pi/2 - \theta, \tag{A.6}$$

and

$$Q' = Q^{inc'} + Q^{refl'}$$

describes the leading-order linear inviscid solution, which for an IW beam reflection becomes:

$$\begin{aligned} Q^{inc'} &= \int_0^\infty A(\tilde{k}') \exp(i\tilde{k}'(x' + y' \cot\Theta)) d\tilde{k}', \\ Q^{refl'} &= -\int_0^\infty A(\tilde{k}') \exp(i\tilde{k}'(x' - y' \cot\Theta)) d\tilde{k}'. \end{aligned} \tag{A.7}$$

To simplify further, we consider the case of a plane wave reflection, for which

$$\begin{aligned} Q^{inc'} &= \exp(ik'(x' + y' \cot\Theta)), \\ Q^{refl'} &= -\exp(ik'(x' - y' \cot\Theta)) \ . \end{aligned} \tag{A.8}$$

The leading-order U' can be written as

$$U' = Q'_{y'} = ik' \cot\Theta (Q^{inc'} - Q^{refl'}),$$

and then

$$\begin{aligned} & U(x', y') e^{-i\omega_0 t} + c.c. \\ = \ & -4k' \cot\Theta sin(k'x' - \omega_0 t) \cos(k'y' \cot\Theta) \\ = \ & -4k' \tan\theta sin(k'x' - \omega_0 t) \cos(k'y' \tan\theta) \ . \end{aligned} \tag{A.9}$$

We are to first apply this formulation to a plane wave, as the unit envelope function allows us to obtain a closed-form expression that can be directly evaluated. Applying (A.5) to plane wave,

$$\begin{aligned} Q'_0 &= -4k'^2 \frac{\cos\Theta}{\sin^2\Theta} \sin(2k'y' \cot\Theta) \\ &= -4k'^2 \frac{\sin\theta}{\cos^2\theta} \sin(2k'y' \tan\theta) \ , \end{aligned} \tag{A.10}$$

and then using

$$\begin{aligned} U'_0 = Q'_{0y'} &= -8k'^3 \frac{\cos^2\Theta}{\sin^3\Theta} \cos(2k'y' \cot\Theta) \\ &= -8k'^3 \frac{\sin^2\theta}{\cos^3\theta} \cos(2k'y' \tan\theta) \ , \end{aligned} \tag{A.11}$$

gives the dimensionless mean flow distribution due to the reflection of a plane wave and is consistent (Thorpe, 1987).

Recall (A.2) and that $m = \tan\theta k$ is the vertical wavenumber. Substituting (A.9) and (A.11) into (A.4) and express u in dimensional form:

$$\begin{aligned} u &= u'\lambda_x N \\ &= -8\pi\epsilon\lambda_x N \tan\theta \sin(kx - \omega_0 t)\cos(my) \\ &\quad -64\pi^3\epsilon^2\lambda_x N \frac{\sin^2\theta}{\cos^3\theta}\cos(2my) + \cdots , \end{aligned} \tag{A.12}$$

where $\cdots$ denotes terms corresponding to second and higher harmonics.

In an attempt to express ϵ in physical quantities that are used in the present study, apply (A.12) at $x = 0$ and $z = L_z$, i.e., at the reflecting surface ($y = 0$):

$$\begin{aligned} u &= 8\pi\epsilon\lambda_x N \tan\theta \sin(\omega_0 t) \\ &\quad -64\pi^3\epsilon^2\lambda_x N \frac{\sin^2\theta}{\cos^3\theta} + \cdots . \end{aligned} \tag{A.13}$$

We express u in our nomenclature as (4.11), i.e.,

$$u = (U_0 e^{-i(\omega_0 t+\phi)} + c.c.) + \langle u \rangle.$$

where $\langle u \rangle$ is the mean velocity and U_0 is a characteristic velocity of the wave (not to confuse with U_0', which denotes mean flow). In order for the two sets of nomenclature, i.e., (4.11) and (A.13), to match on the magnitude of leading-order wave component, we require

$$8\pi\epsilon\lambda_x N \tan\theta = 2U_0.$$

Therefore,

$$\epsilon = \frac{U_0}{4\pi\lambda_x N \tan\theta}, \tag{A.14}$$

which can be linked to wave steepness A by

$$\epsilon = \frac{\cos\theta}{4\pi} A. \tag{A.15}$$

The relative mean flow strength $\mathcal{M}$, as defined in (4.12), can be computed based on (A.13) for plane wave reflection:

$$\begin{aligned} \mathcal{M} &= \langle u \rangle / U_0 \\ &= 16\pi^2 \epsilon \frac{\sin\theta}{\cos^2\theta} \\ &= 4\pi A \tan\theta \ . \end{aligned} \tag{A.16}$$

The mean flow for the reflection of a wave beam, with a particular spatial envelope function (A.7), can only be computed numerically using TAL's formulation. The resulting mean flow is found to be approximately equal in strength with the plane wave counterpart (see Fig. 4.9).

APPENDIX B

STOKES DRIFT WITHIN REFLECTING INTERNAL WAVES

B.1 Scaling Stokes drift

Consider a fluid particle with an initial/reference position (x_0^+, z_0^+) at $t = t_0$. Note that the superscript $^+$ will be used to denote quantities associated with the Lagrangian frame. The instantaneous position of this particle at time t is given exactly as

$$(x^+, z^+) = (x_0^+ + \int_{t_0}^{t} u^+(t')dt', z_0^+ + \int_{t_0}^{t} w^+(t')dt'). \tag{B.1}$$

where

$$u^+(t') \equiv u(x^+(t'), z^+(t'), t'), \tag{B.2}$$

$$w^+(t') \equiv w(x^+(t'), z^+(t'), t'). \tag{B.3}$$

and (u, w) are the Eulerian velocities. For small particle displacements, one can approximate (Longuet-Higgins, 1969; Kundu and Cohen, 2008) the instantaneous velocity $u^+(t)$ by a Taylor series expansion in space around (x_0^+, z_0^+):

$$u^+(t) = u(x_0^+, z_0^+, t) + \frac{\partial u}{\partial x}|_{(x_0^+, z_0^+, t)}\Delta x^+(t) + \frac{\partial u}{\partial z}|_{(x_0^+, z_0^+, t)}\Delta z^+(t) + \text{h.o.t.}, \tag{B.4}$$

where the displacement

$$(\Delta x^+, \Delta z^+) \equiv (x^+, z^+) - (x_0^+, z_0^+). \tag{B.5}$$

One can also define the temporal wave average of any quantity f as

$$\langle f \rangle \equiv \frac{1}{T} \int_{t_0}^{t_0+T} f(t')dt', \tag{B.6}$$

with T being the wave period, and apply this wave average to (B.4) to obtain an expression for the wave-mean Lagrangian velocity $\langle u^+ \rangle$ for a particle initially at

(x_0^+, z_0^+) at the beginning of the wave cycle, i.e., $t = t_0$:

$$\langle u^+ \rangle = \langle u \rangle + \langle \frac{\partial u}{\partial x} \Delta x^+ \rangle + \langle \frac{\partial u}{\partial z} \Delta z^+ \rangle + \text{h.o.t.}, \tag{B.7}$$

where the first term on the RHS, i.e., $\langle u \rangle$, corresponds to the mean Eulerian velocity at there reference point (x_0^+, z_0^+), and all the other terms on the RHS sum up to the *Stokes drift* u_S. One can symbolically rewrite (B.7) as

$$\langle \text{Lagrange} \rangle = \langle \text{Euler} \rangle + \text{Stokes}, \tag{B.8}$$

which is a canonical decomposition for wave-mean Lagrangian motions in wavy flows (Longuet-Higgins, 1969; Monismith and Fong, 2004; Bühler, 2009).

Examining the Stokes drift terms in (B.7) more closely, one may define:

$$u_S \equiv \langle \frac{\partial u}{\partial x} \Delta x^+ \rangle + \langle \frac{\partial u}{\partial z} \Delta z^+ \rangle + \text{h.o.t.}. \tag{B.9}$$

The two leading terms of u_S can be considered as the operator

$$\langle \frac{\partial (.)}{\partial x} \Delta x^+ \rangle + \langle \frac{\partial (.)}{\partial z} \Delta z^+ \rangle \tag{B.10}$$

which is applied to u. Following the scaling used in §4.1, i.e.,

$$\frac{\partial}{\partial x} \sim \frac{\partial}{\partial z} \sim \frac{1}{\lambda_x}, \Delta x^+ \sim \Delta z^+ \sim U_0 T, \langle\ \rangle \sim \frac{1}{T} \int_{t_0+T}^{T} dt \sim 1, \tag{B.11}$$

the leading-order Stokes operator, i.e., (B.10), scales linearly in wave amplitude A:

$$\langle \frac{\partial (.)}{\partial x} \Delta x^+ \rangle \sim \langle \frac{\partial (.)}{\partial z} \Delta z^+ \rangle \sim \frac{U_0 T}{\lambda_x} \sim O(A). \tag{B.12}$$

This Stokes operator, $O(A)$ by itself, is to be applied to various orders of dynamics in u to produce the corresponding leading-order Stokes drift due to each order of u respectively. (B.12) bears the simple but non-trivial implication that, for the $O(A^n)$ dynamics of u, the corresponding leading-order Stokes drift due to u of this order is, at most, produced on the immediate higher order, i.e., $O(A^{n+1})$.

For the IW reflection problem, both the weakly nonlinear theory (Thorpe, 1987; Tabaei *et al.*, 2005) and DNS by Z&D suggest that, along with the primary reflecting wave of leading-order $O(A)$, an Eulerian mean flow and a second harmonic coexist on the second order $O(A^2)$. The $O(A)$ primary wave, consisting of both incident and reflected waves, is expected, based on the aforementioned scaling, to produce a Stokes drift on $O(A^2)$; the $O(A^2)$ second harmonic drives a Stokes drift which is at best $O(A^3)$, and will be excluded from the scope of an $O(A^2)$ analyses. Therefore, to obtain an approximation for mean Lagrangian flow $\langle u^+ \rangle$ up to $O(A^2)$, i.e., $\langle u_{L,II} \rangle$[1], one would need to take into account both the $O(A^2)$ Eulerian mean $\langle u \rangle$ and Stokes drift $u_{S,II}$, the latter being exclusively driven by the $O(A)$ primary wave. Recalling (B.7), one can write the $O(A^2)$ balance:

$$\langle u_{L,II} \rangle = \langle u \rangle + u_{S,II}, \tag{B.13}$$

where $u_{S,II}$ can be obtained by applying the Stokes operator (B.10) to u velocities due to the $O(A)$ primary wave, i.e., u_I.

B.2 Euler-Stokes cancellation for plane IW reflection

(B.13) now guides the derivation of an $O(A^2)$ approximation to the mean Lagrangian flows due to a plane IW reflection.

Eulerian mean flow. For the reflection of a plane IW, a semi-infinite domain where $-\infty < x < \infty$ and $-\infty < z' \leq 0$ is considered. The reflecting surface is located at $z' = 0$, and the incident wave has a upward (positive) group velocity at an angle θ with respect to z'. According to the inviscid weakly-nonlinear solution

[1]Here and elsewhere, Roman numerals in subscripts denote orders of dynamics, e.g., "II" in the subscript of $u_{S,II}$ denotes an $O(A^2)$ effect.

(Thorpe, 1987; Tabaei *et al.*, 2005) for reflections off a rigid lid, the Eulerian mean flow due to wave-wave interaction in reflecting IW at a horizontal boundary is (see the derivation in Appendix A)

$$\langle u \rangle = -\frac{2U_0^2}{c_x} \cos(2k_z z'). \tag{B.14}$$

The Eulerian mean flow $\langle u \rangle$ is constant in x and periodic in z' with a wavelength equal to half of the vertical wavelength $2\pi/k_z$ of the incident (or reflected) wave.

Stokes drift. To obtain the $O(A^2)$ Stokes drift $u_{S,II}$, one is to apply the Stokes operator in (B.10) to the inviscid leading-order (linear) solution (LeBlond and Mysak, 1978) for plane IW reflection. The solution contains the contribution from the incident wave

$$(u, w)_{inc,I} = [U_0 \sin(k_x x - k_z z' - \omega t + \alpha), U_0 \cot\theta \sin(k_x x - k_z z' - \omega t + \alpha)]$$

and the reflected wave

$$(u, w)_{refl,I} = [U_0 \sin(k_x x + k_z z' - \omega t + \alpha), -U_0 \cot\theta \sin(k_x x + k_z z' - \omega t + \alpha)]$$

respectively, where α is an arbitrary phase lag. Note that the dimensionless wave amplitude (steepness) (Sutherland, 2010; Zhou and Diamessis, 2013) A can be computed based on the maximum horizontal velocity U_0 within each of the leading-order waves (see the derivation in §4.1). Summing the two linear waves up results in:

$$\begin{aligned} (u, w)_I &= (u, w)_{inc,I} + (u, w)_{refl,I} \\ &= (2U_0 \sin\phi \cos(k_z z'), -2U_0 \cot\theta \cos\phi \sin(k_z z')), \end{aligned} \tag{B.15}$$

where $\phi(x, t) = k_x x - \omega t + \alpha$.

Consider a particle with initial position $(x, z') = (x_0^+, z_0^+)$ at $t = t_0$. The leading-order, i.e., $O(A)$, approximation to its instantaneous displacement can be obtained by integrating the velocities $(u, w)_I$ at the initial position (Longuet-Higgins, 1969; Kundu and Cohen, 2008):

$$\Delta x^+ \approx \int_{t_0}^{t} u_I(x_0^+, z_0^+, t')dt' = \frac{2U_0 \cos(k_z z_0^+)}{\omega}(\cos\phi_0(t) - \cos\phi_{00}), \tag{B.16}$$

and

$$\Delta z^+ \approx \int_{t_0}^{t} w_I(x_0^+, z_0^+, t')dt' = \frac{2U_0 \cot\theta \sin(k_z z_0^+)}{\omega}(\sin(\phi_0(t)) - \sin\phi_{00}), \tag{B.17}$$

where $\phi_0(t) \equiv \phi(x_0^+, t)$ and $\phi_{00} \equiv \phi(x_0^+, t_0)$. The gradients of u at (x_0^+, z_0^+), which are approximated up to $O(A)$ by those of u_I, are

$$\frac{\partial u}{\partial x}\,|_{(x_0^+, z_0^+, t)} \approx \frac{\partial u_I}{\partial x}\,|_{(x_0^+, z_0^+, t)} = 2k_x U_0 \cos(k_z z_0^+)\cos\phi_0(t), \tag{B.18}$$

$$\frac{\partial u}{\partial z}\,|_{(x_0^+, z_0^+, t)} \approx \frac{\partial u_I}{\partial z}\,|_{(x_0^+, z_0^+, t)} = -2k_z U_0 \sin(k_z z_0^+)\sin\phi_0(t). \tag{B.19}$$

The Stokes operator in (B.10) can now be readily computed to obtain the two contributors to Stokes drift:

$$\langle \frac{\partial u}{\partial x}\Delta x^+ \rangle \approx \langle \frac{\partial u_I}{\partial x}\int u_I dt \rangle = 2\frac{k_x}{\omega}U_0^2 \cos^2(k_z z_0^+) = \frac{2U_0^2}{c_x}\cos^2(k_z z_0^+), \tag{B.20}$$

and

$$\langle \frac{\partial u}{\partial z}\Delta z^+ \rangle \approx \langle \frac{\partial u_I}{\partial z}\int w_I dt \rangle = -2\frac{k_x}{\omega}U_0^2 \sin^2(k_z z_0^+) = -\frac{2U_0^2}{c_x}\sin^2(k_z z_0^+), \tag{B.21}$$

which sum up to the total $O(A^2)$ Stokes drift

$$u_{S,II} = \frac{2U_0^2}{c_x}(\cos^2(k_z z_0^+) - \sin^2(k_z z_0^+)) = \frac{2U_0^2}{c_x}\cos(2k_z z_0^+) \tag{B.22}$$

due to the $O(A)$ primary wave. The $O(A^2)$ Stokes drift $u_{S,II}$ has dependence on neither x, a homogeneous direction in the set-up, nor t_0, the initial time of the wave averaging.

Euler-Stokes cancellation. With (B.14), (B.22) and (B.13), one can obtain a second-order accurate estimate of the mean Lagrangian drift:

$$\begin{aligned} \langle u_{L,II} \rangle &= \langle u \rangle + u_{S,II} \\ &= -\frac{2U_0^2}{c_x} \cos(2k_z z_0^+) + \frac{2U_0^2}{c_x} \cos(2k_z z_0^+) \\ &= 0, \end{aligned} \tag{B.23}$$

which suggests that the second-order Eulerian mean flow due to wave-wave interaction and Stokes drift due to leading-order primary wave cancel out each other completely within a reflecting plane IW, yielding zero Lagrangian mean flow up to $O(A^2)$. To reach this conclusion, the inviscid solutions to the reflection problem have been used and small-amplitude approximations invoked.

APPENDIX C

SET-UP OF WAVE-ABSORBING SPONGE LAYER

In §6 and §7, stratified turbulent wakes of a wide range of parameter values are simulated. Since internal waves are emitted to the ambient from the turbulent wake core, it is imperative that the wave energy does not re-enter the finite-sized computational domain through the periodic boundaries in the horizontal (Gourlay *et al.*, 2001) or reflect off the bottom (and top if needed) of the domain to affect the flow within. The same requirement also applies to the internal wave reflections considered in §4. In order to absorb the wave energy at these boundaries, sponge layer of the "Rayleigh-damping" type are installed along the boundaries, following Abdilghanie (2010).

The sponge layer terms $\mathbf{S_u}$ and S_ρ in (3.1) takes the form $-R(\eta)\mathbf{u}$ and $-R(\eta)\rho$ respectively, where η is the normal distance to the boundaries. The ratio $1/R(\eta)$ sets a characteristic time scale of the absorbing layer over which the layer acts to effectively damp out the disturbance within it. The $R(\eta)$ parameters take the form (Klemp and Lilly, 1978; Abdilghanie, 2010):

$$R(\eta) = \begin{cases} \frac{1}{T_{sp}} \sin^2\left(\frac{\pi}{2}\frac{\eta-\delta_t}{\delta_t}\right) & \text{for } \eta \le \delta_t, \\ 0 & \text{for } \eta > \delta_t, \end{cases} \tag{C.1}$$

where T_{sp} is the sponge layer time scale and δ_t is the thickness of sponge layer. T_{sp} is chosen to be the buoyancy period $2\pi/N$, and the optimal thickness δ_t is adjusted according to the predominant wavelength emitted by the turbulence to optimize the wave-absorbing performance (Abdilghanie, 2010). Specifically, sponge layers with $\delta_t = 2D$ are used for $Fr \in \{4, 16\}$, where D is the sphere diameter, and $\delta_t = 4D$ is used for the $Fr = 64$ simulations to accommodate for the larger wavelength observed. No sponge layers are installed on the top boundary for the

simulations considered in §6, where the main goal is to investigate the internal wave manifestation at the model sea surface; in the $Re = 4 \times 10^5$ simulations considered in §7, however, smaller domain heights are used to minimize computational cost, and the top boundary is sealed by sponge layer. The thickness of sponge layers for the internal wave simulations in §4 are summarized in Table 4.2. Note that the time scale T_{sp} also impose an constraint on the maximum time step size allowed, in addition to the CFL number constraints (Diamessis *et al.*, 2005); this is discussed in greater detail in Abdilghanie (2010). Typically about 20% of the total number of grid points used in these simulations are allocated to the sponge layers.

APPENDIX D

DNS VERIFICATION OF STRATIFIED WAKE SIMULATIONS

To assess the quality of the implicit large-eddy simulations (LES), direct numerical simulations (DNS) are performed by Professor Stephen de Bruyn Kops through a collaborated study on stratified turbulence. The DNS are initialized by taking the flow field from the LES dataset at a given time in the NEQ regime of the wake, at $Nt = 41$, and interpolating on to the finer DNS grid with the filtered scales filled with artificial noises according to a model spectrum. The DNS is carried out for one buoyancy time unit $(1/N)$ and compared to the LES flow field at the same time instance, i.e., at $Nt = 42$. The spatial resolution of the DNS is quadrupled from that of the LES. It is expected that the DNS resolves the full inertial subrange and the dissipative range which are under the influence of spectral filtering in the implicit LES.

Here representative results at $Re = 10^5$ and $Fr = 4$ are shown in Figs. D.1 and D.2. Fig. D.1 compares the mean and rms u velocities computed in the homogeneous x direction on the wake center Oxy plane at $Nt = 42$; DNS and LES agree reasonably well. Fig. D.2 compares the horizontal energy spectra of density perturbation ρ on the Oxy plane. As expected, free from the effect of filtering, the DNS spectra extend further in the spectra space; the LES spectra start to drop earlier due to filtering, and there does not appear to be significant blockage of energy around the cut-off wavenumber of the filter. The LES, without an explicitly specified subgrid scale (SGS) model, appear to resolve accurately most of the energy and compare reasonably well with the DNS, as far as the resolved scales are concerned. Developing a physics-based SGS model which is informed by DNS data and takes into account the inherent anisotropic nature is an ongoing

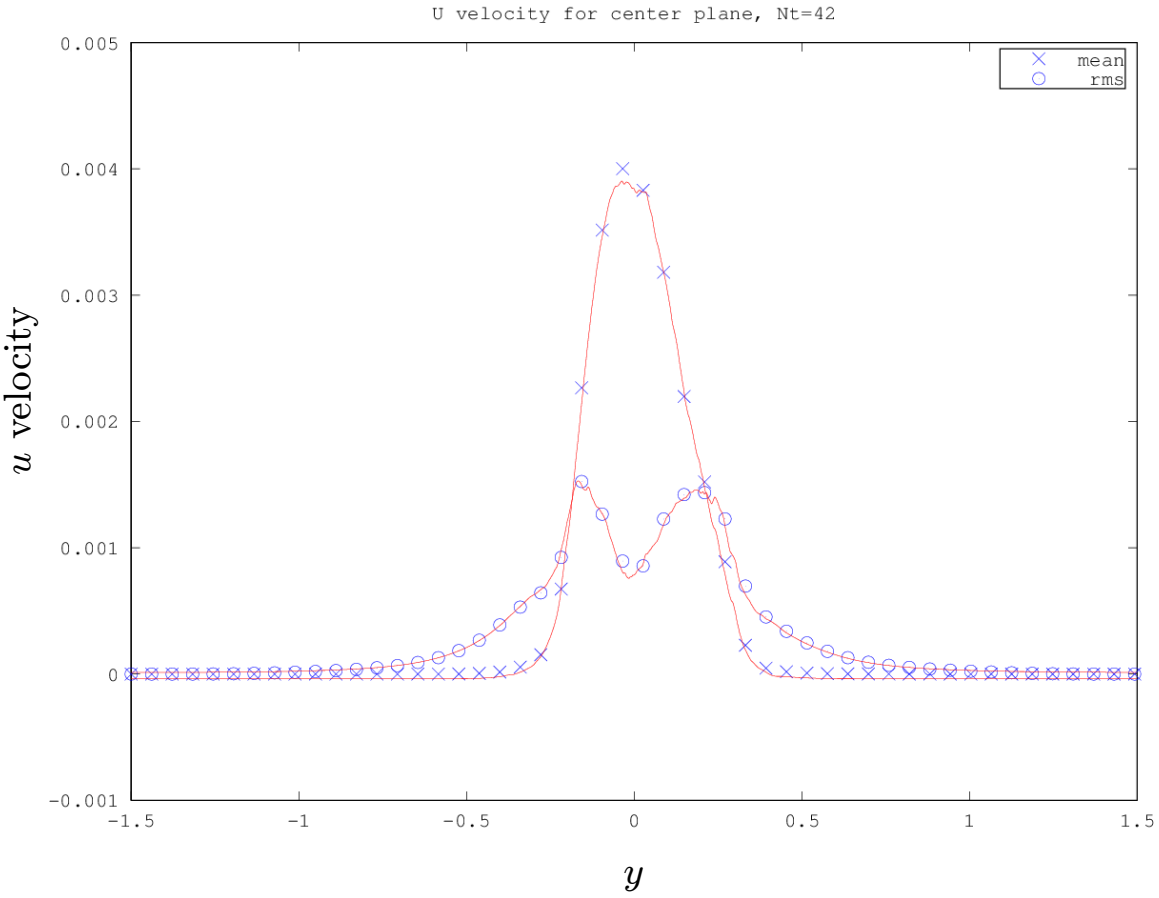

Figure D.1: Comparison of DNS and LES results on the wake center Oxy plane. Mean and rms u velocities in the homogeneous x direction are plotted as a function of y. LES data are drawn as symbols, and the DNS counterparts are solid lines. DNS data are courtesy of Prof. Stephen de Bruyn Kops.

research effort.

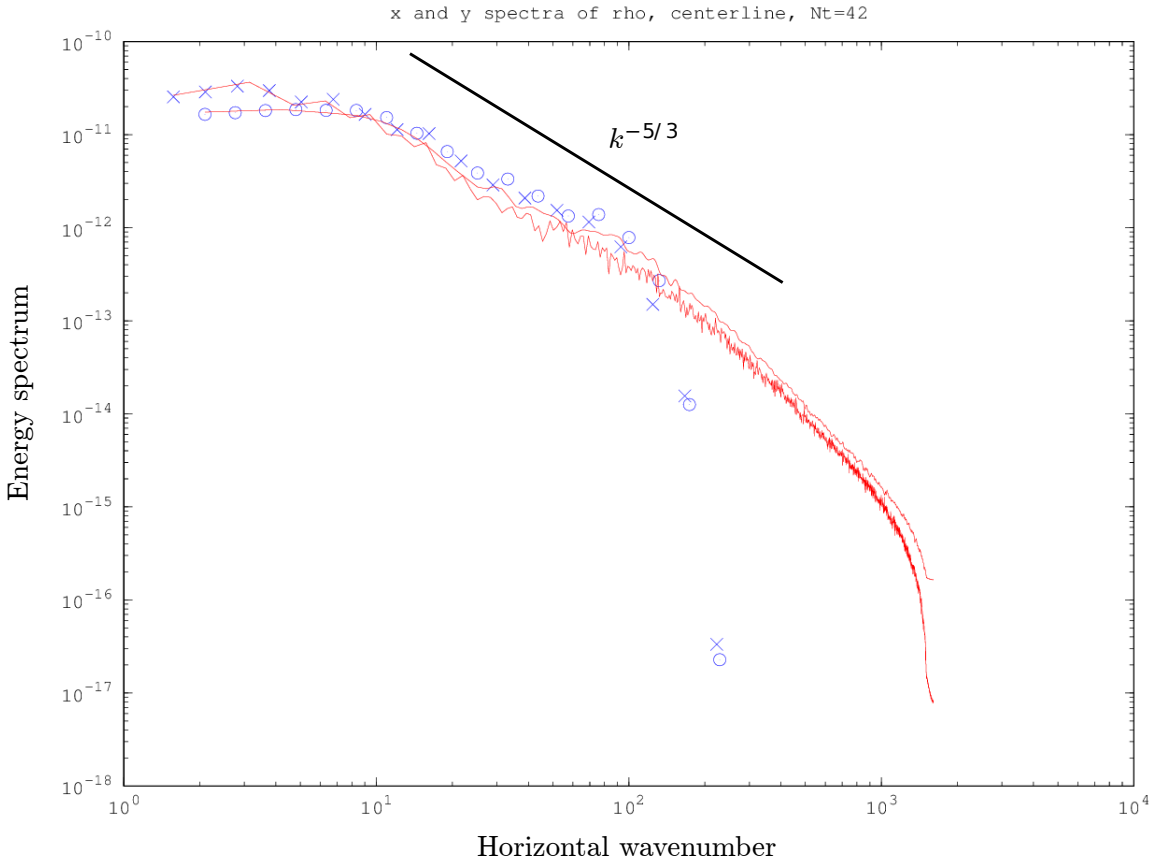

Figure D.2: Comparison of DNS and LES results on the wake center Oxy plane. Energy spectra of density perturbation ρ, in x and y directions respectively, are plotted as a function of wavenumber. LES data are drawn as symbols (circles for x-spectrum and crosses for y), and the DNS counterparts are solid lines. The cut-off wavenumber k_c of the LES filter is around 170. DNS data are courtesy of Prof. Stephen de Bruyn Kops.

BIBLIOGRAPHY

A. M. Abdilghanie. *A numerical investigation of turbulence-driven and forced generation of internal gravity waves in stratified mid-water*. PhD thesis, Cornell University, Ithaca, New York, 2010.

A. M. Abdilghanie and P. J. Diamessis. On the generation and evolution of numerically simulated large-amplitude internal gravity wave packets. *Theor. Comp. Fluid Dyn.*, 26:205–224, 2012.

A. M. Abdilghanie and P. J. Diamessis. The internal gravity wave field emitted by a stably stratified turbulent wake. *J. Fluid Mech.*, 720:104–139, referred to in text as "A&D", 2013.

T. R. Akylas, R. H. J. Grimshaw, S. R. Clarke, and A. Tabaei. Reflecting tidal wave beams and local generation of solitary waves in the ocean thermocline. *J. Fluid Mech.*, 593:297–313, 2007.

W. Alpers. Theory of radar imaging of internal waves. *Nature*, 314:245–247, 1985.

P. Augier and P. Billant. Onset of secondary instabilities on the zigzag instability in stratified fluids. *J. Fluid Mech.*, 682:120–131, 2011.

P. Augier, J.-M. Chomaz, and P. Billant. Spectral analysis of the transition to turbulence from a dipole in stratified fluid. *J. Fluid Mech.*, 713:86–108, 2012.

P. Bartello and S. M. Tobias. Sensitivity of stratified turbulence to the buoyancy Reynolds number. *J. Fluid Mech.*, 725:1–22, 2013.

P. A. Bevilaqua and P. S. Lykoudis. Turbulence memory in self-preserving wakes. *J. Fluid Mech.*, 89:589–606, 1978.

P. Billant and J.-M. Chomaz. Experimental evidence for a new instability of a vertical columnar vortex pair in a strongly stratified fluid. *J. Fluid Mech.*, 418: 167–188, 2000.

P. Billant and J.-M. Chomaz. Self-similarity of strongly stratified inviscid flows. *Phys. Fluids*, 13:1645, 2001.

P. Bonneton, J.-M. Chomaz, and E. J. Hopfinger. Internal waves produced by the turbulent wake of a sphere moving horizontally in a stratified fluid. *J. Fluid Mech.*, 254:23–40, 1993.

G. Bordes, A. Venaille, S. Joubaud, P. Odier, and T. Dauxois. Experimental observation of a strong mean flow induced by internal gravity waves. *Phys. Fluids*, 24:086602, 2012.

B. Bourget, T. Dauxois, S. Joubaud, and P. Odier. Experimental study of parametric subharmonic instability for internal plane waves. *J. Fluid Mech.*, 723: 1–20, 2013.

J. P. Boyd. *Chebyshev and Fourier Spectral Methods (2nd Revised Ed.)*. Dover Publications, 2001.

G. Brethouwer, P. Billant, E. Lindborg, and J.-M. Chomaz. Scaling analysis and simulation of strongly stratified turbulent flows. *J. Fluid Mech.*, 585:343–368, referred in text as "BBLC", 2007.

D. Broutman, J. W. Rottman, and S. D. Eckermann. Ray methods for internal waves in the atmosphere and ocean. *Annu. Rev. Fluid Mech.*, 36:233–253, 2004.

K. A. Brucker and S. Sarkar. A comparative study of self-propelled and towed wakes in a stratified fluid. *J. Fluid Mech.*, 652:373–404, 2010.

O. Bühler. *Waves and Mean Flows*. Cambridge University Press, New York, 2009.

O. Bühler, N. Grisouard, and M. Holmes-Cerfon. Strong particle dispersion by weakly dissipative random internal waves. *J. Fluid Mech.*, 719:R4, 2013.

F. K. Chow and P. Moin. A further study of numerical errors in large-eddy simulations. *J. Comput. Phys.*, 184:366–380, 2003.

S. T. Cole, D. L. Rudnick, B. A. Hodges, and J. P. Martin. Observations of tidal internal wave beams at Kauai Channel, Hawaii. *J. Phys. Oceanogr.*, 39:421–436, 2009.

G. Cresswell, C. Zhou, P. C. Tildesley, and C. S. Nilsson. SAR observations of internal wave wakes from sea mounts. *Mar. Freshwater Res.*, 47:489–495, 1996.

J. C. B. da Silva, A. L. New, M. A. Srokosz, and T. J. Smyth. On the observability of internal tidal waves in remotely-sensed ocean colour data. *Geophys. Res. Lett.*, 29:1569, 2002.

T. Dallard and G. R. Spedding. 2-D wavelet transforms: Generalisation of the Hardy space and application to experimental studies. *Eur. J. Mech. B-Fluid*, 12:107–134, 1993.

T. Dauxois, A. Didier, and E. Falcon. Near-critical reflection of internal waves. *J. Fluid Mech.*, 390:271–295, 1999.

T. Dauxois, A. Didier, and E. Falcon. Observation of near-critical reflection of internal waves in a stably stratified fluid. *Phys. Fluids*, 16:1936, 2004.

M. B. de Stadler and S. Sarkar. Simulation of a propelled wake with moderate excess momentum in a stratified fluid. *J. Fluid Mech.*, 692:28–52, 2012.

P. J. Diamessis, J. A. Domaradzki, and J. S. Hesthaven. A spectral multidomain penalty method model for the simulation of high Reynolds number localized incompressible stratified turbulence. *J. Comput. Phys.*, 202:298–322, referred to in text as "DDH", 2005.

P. J. Diamessis, G. R. Spedding, and J. A. Domaradzki. Similarity scaling and vorticity structure in high-Reynolds-number stably stratified turbulent wakes. *J. Fluid Mech.*, 671:52–95, referred to in text as "DSD", 2011.

P. J. Diamessis, S. Wunsch, I. Delwiche, and M. P. Richter. Nonlinear generation of harmonics through the interaction of an internal wave beam with a model oceanic pycnocline. *Dyn. Atmos. Oceans*, 66:110–137, 2014.

D. G. Dommermuth, J. W. Rottman, G. E. Innis, and E. A. Novikov. Numerical simulation of the wake of a towed sphere in a weakly stratified fluid. *J. Fluid Mech.*, 473:83–101, 2002.

P Echeverri, M. R. Flynn, K. B. Winters, and T. Peacock. Low-mode internal tide generation by topography: An experimental and numerical investigation. *J. Fluid Mech.*, 636:91–108, 2009.

S. A. Ermakov, S. G. Salashin, and A. R. Panchenko. Film slicks on the sea surface and some mechanisms of their formation. *Dyn. Atmos. Oceans*, 16:279–304, 1992.

G. C. Ewing. Slicks, surface films and internal waves. *J. Mar. Res.*, 9:161–187, 1950a.

G. C. Ewing. Relation between band slicks at the surface and internal waves in the sea. *Science*, 111:91–94, 1950b.

J. T. Farrar, C. J. Zappa, R. A. Weller, and Andrew T. Jessup. Sea surface

temperature signatures of oceanic internal waves in low winds. *J. Geophys. Res.*, 112:C06014, 2007.

C. Garrett and E. Kunze. Internal tide generation in the deep ocean. *Annu. Rev. Fluid Mech.*, 39:57–87, 2007.

B. Gayen and S. Sarkar. Degradation of an internal wave beam by parametric subharmonic instability in an upper ocean pycnocline. *J. Geophys. Res.*, 118: 4689–4698, 2013.

H. E. Gilreath and A. Brandt. Experiments on the generation of internal waves in a stratified fluid. *AIAA J.*, 23:693–700, 1985.

R. Godoy-Diana, J.-M. Chomaz, and P. Billant. Vertical length scale selection for pancake vortices in strongly stratified viscous fluids. *J. Fluid Mech.*, 504: 229–238, 2004.

L. Gostiaux and T. Dauxois. Laboratory experiments on the generation of internal tidal beams over steep slopes. *Phys. Fluids*, 19:028102, 2007.

L. Gostiaux, T. Dauxois, H. Didelle, J. Sommeria, and S. Viboud. Quantitative laboratory observations of internal wave reflection on ascending slopes. *Phys. Fluids*, 18:056602, 2006.

L. Gostiaux, H. Didelle, S. Mercier, and T. Dauxois. A novel internal waves generator. *Exp. Fluids*, 42:123–130, 2007.

D. Gottlieb and J. S. Hesthaven. Spectral methods for hyperbolic problems. *J. Comput. Appl. Math.*, 128:83–131, 2001.

M. J. Gourlay, S. C. Arendt, D. C. Fritts, and J. Werne. Numerical modeling of initially turbulent wakes with net momentum. *Phys. Fluids*, 13:3783–3802, 2001.

N. Grisouard, C. Staquet, and T. Gerkema. Generation of internal solitary waves in a pycnocline by an internal wave beam: A numerical study. *J. Fluid Mech.*, 676:491–513, 2011.

N. Grisouard, M. Leclair, L. Gostiaux, and C. Staquet. Large scale energy transfer from an internal gravity wave reflecting on a simple slope. *Procedia IUTAM*, 8: 119–128, 2013.

D. A. Hebert and S. M. de Bruyn Kops. Predicting turbulence in flows with strong stable stratification. *Phys. Fluids*, 18:066602, 2006.

E. J. Hopfinger, J.-B. Flor, J.-M. Chomaz, and P. Bonneton. Internal waves generated by a moving sphere and its wake in a stratified fluid. *Exp. Fluids*, 11: 255–261, 1991.

H.-H. Hwung, R.-Y. Yang, and I. V. Shugan. Exposure of internal waves on the sea surface. *J. Fluid Mech.*, 626:1–20, 2009.

G. N. Ivey, K. B. Winters, and J. R. Koseff. Density stratification, turbulence, but how much mixing? *Ann. Rev. Fluid Mech.*, 40:169–184, 2008.

A. Javam, J. Imberger, and S. W. Armfield. Numerical study of internal wave reflection from sloping boundaries. *J. Fluid Mech.*, 396:183–201, 1999.

A. Javam, J. Imberger, and S. W. Armfield. Numerical study of internal wave-wave interactions in a stratified fluid. *J. Fluid Mech.*, 415:65–87, 2000.

C.-H. Jiang and P. S. Marcus. Selection rules for the nonlinear interaction of internal gravity waves. *Phys. Rev. Lett.*, 102:124502, 2009.

T. M. S. Johnston, D. L. Rudnick, G. S. Carter, R. E. Todd, and S. T. Cole.

Internal tidal beams and mixing near Monterey Bay. *J. Geophys. Res.*, 116: C12039, 2011.

S. Joubaud, J. Munroe, P. Odier, and T. Dauxois. Experimental parametric subharmonic instability in stratified fluids. *Phys. Fluids*, 24:041703, 2012.

G. E. Karniadakis, M. Israeli, and S. A. Orszag. High-order splitting methods for the incompressible Navier-Stokes equations. *J. Comput. Phys.*, 97:414–443, 1991.

T. Kataoka and T. R. Akylas. Stability of internal gravity wave beams to three-dimensional modulations. *J. Fluid Mech.*, 736:67–90, 2013.

R. N. Keeler, V. G. Bondur, and C. H. Gibson. Optical satellite imagery detection of internal wave effects from a submerged turbulent outfall in the stratified ocean. *Geophys. Res. Lett.*, 32:L12610, 2005.

Y. V. Kistovich and Y. D. Chashechkin. The reflection of beams of internal gravity waves at a flat rigid surface. *J. Appl. Math. Mech.*, 59:579–585, 1995.

V. Klemas. Remote sensing of ocean internal waves: An overview. *J. Coastal Res.*, 28:540–546, 2012.

J. B. Klemp and D. K. Lilly. Numerical simulation of hydrostatic mountain waves. *J. Atoms. Sci.*, 35:78–107, 1978.

P. K. Kundu and I. M. Cohen. *Fluid Mechanics (4th Ed.)*. Academic Press, San Diego, 2008.

K. G. Lamb. Nonlinear interaction among internal wave beams generated by tidal flow over supercritical topography. *Geophys. Res. Lett.*, 31:L09313, 2004.

P. H. LeBlond and L. A. Mysak. *Waves in the Ocean*. Elsevier Scientific Publishing Company, Amsterdam, 1978.

M. Leclair, N. Grisouard, L. Gostiaux, C. Staquet, and F. Auclair. Reflexion of a plane wave onto a slope and wave-induced mean flow. In *Proceedings of the VII International Symposium on Stratified Flows*, pages 22–26, Rome, 2011.

R.-C. Lien and M. C. Gregg. Observations of turbulence in a tidal beam and across a coastal ridge. *J. Geophys. Res.*, 106:4575–4591, 2001.

J. Lighthill. *Waves in Fluids*. Cambridge University Press, New York, 1978.

D. K. Lilly. Stratified turbulence and the mesoscale variability of the atmosphere. *J. Atoms. Sci.*, 40:749–761, 1983.

J.-T. Lin and Y.-H. Pao. Wakes in stratified fluids. *Ann. Rev. Fluid Mech.*, 11: 317–338, 1979.

E. Lindborg. The energy cascade in a strongly stratified fluid. *J. Fluid Mech.*, 550: 207–242, 2006.

M. S. Longuet-Higgins. On the transport of mass by time-varying ocean currents. *Deep-Sea Res.*, 16:431–447, 1969.

J. M. Magalhaes, J. C. B. da Silva, M. Batista, L. Gostiaux, T. Gerkema, A. L. New, and D. R. G. Jeans. On the detectability of internal waves by an imaging lidar. *Geophys. Res. Lett.*, 40:3429–3434, 2013.

G. O. Marmorino, G. B. Smith, and G. J. Lindemann. Infrared imagery of ocean internal waves. *Geophys. Res. Lett.*, 31:L11309, 2004.

G. O. Marmorino, G. B. Smith, W. D. Miller, and J. H. Bowles. Detection of a buoyant coastal wastewater discharge using airborne hyperspectral and infrared imagery. *J. Appl. Remote Sens.*, 4:043502, 2010.

M. Mathur and T. Peacock. Internal wave beam propagation in non-uniform stratifications. *J. Fluid Mech.*, 639:133–152, 2009.

M. J. Mercier, N. B. Garnier, and T. Dauxois. Reflection and diffraction of internal waves analyzed with the Hilbert transform. *Phys. Fluids*, 20:086601, 2008.

M. J. Mercier, M. Mathur, L. Gostiaux, T. Gerkema, J. M. Magalhaes, J. C. B. da Silva, and T. Dauxois. Soliton generation by internal tidal beams impinging on a pycnocline: Laboratory experiments. *J. Fluid Mech.*, 704:37–60, 2012.

P. Meunier. Stratified wake of a tilted cylinder. Part 2. Lee internal waves. *J. Fluid Mech.*, 699:198–215, 2012.

P. Meunier, P. J. Diamessis, and G. R. Spedding. Self-preservation in stratified momentum wakes. *Phys. Fluids*, 18:106601, referred in text as "MDS", 2006.

S. G. Monismith and D. A. Fong. A note on the potential transport of scalars and organisms by surface waves. *Limnol. Oceanogr.*, 49:1214–1217, 2004.

S. G. Monismith, E. A. Cowen, H. M. Nepf, J. Magnaudet, and L. Thais. Laboratory observations of mean flows under surface gravity waves. *J. Fluid Mech.*, 573:131–147, 2007.

J. N. Moum and W. D. Smyth. The pressure disturbance of a nonlinear internal wave train. *J. Fluid Mech.*, 558:153–177, 2006.

J. N. Moum, D. J. Carlson, and T. J. Cowles. Sea slicks and surface strain. *Deep-Sea Res.*, 37:767–775, 1990.

D. E. Mowbray and B. S. H. Rarity. A theoretical and experimental investigation of the phase configuration of internal waves of small amplitude in a density stratified liquid. *J. Fluid Mech.*, 28:1–16, 1967.

T. R. Osborn. Estimates of the local rate of vertical diffusion from dissipation measurements. *J. Phys. Oceanogr.*, 10:83–89, 1980.

M. F. M. Osborne. The interpretation of infrared radiation from the sea in terms of its boundary layer. *Dtsch. Hydrogr. Z.*, 17:115–136, 1964.

M. F. M. Osborne. The effect of convergent and divergent flow patterns on infrared and optical radiation from the sea. *Dtsch. Hydrogr. Z.*, 18:1–25, 1965.

A. Pal, de Stadler M. B., and Sarkar S. The spatial evolution of fluctuations in a self-propelled wake compared to a patch of turbulence. *Phys. Fluids*, 25:095106, 2010.

T. Peacock and A. Tabaei. Visualization of nonlinear effects in reflecting internal wave beams. *Phys. Fluids*, 17:061702, 2005.

T. Peacock, P. Echeverri, and N. J. Balmforth. An experimental investigation of internal tide generation by two-dimensional topography. *J. Phys. Oceanogr.*, 38: 235–242, 2008.

W. R. Peltier and C. P. Caulfield. Mixing efficiency in stratified shear flows. *Ann. Rev. Fluid Mech.*, 35:135–167, 2003.

R. D. Pingree and A. L. New. Structure, seasonal development and sunglint spatial coherence of the internal tide on the Celtic and Armorican shelves and in the Bay of Biscay. *Deep-Sea Res.*, 42:245–284, 1995.

S. B. Pope. *Turbulent Flows*. Cambridge University Press, New York, 2000.

S. B. Pope. Ten questions concerning the large-eddy simulation of turbulent flows. *New J. Phys.*, 6:35, 2004.

W. H. Press, S. A. Teukolsky, W. T. Vetterling, and B. P. Flannery. *Numerical Recipes (3rd Ed.): The Art of Scientific Computing*. Cambridge University Press, New York, 2007.

J. J. Riley and S. M. de Bruyn Kops. Dynamics of turbulence strongly influenced by buoyancy. *Phys. Fluids*, 15:2047, 2003.

J. J. Riley and M.-P. Lelong. Fluid motions in the presence of strong stable stratification. *Annu. Rev. Fluid Mech.*, 32:613–657, 2000.

J. J. Riley and E. Lindborg. *Ten Chapters in Turbulence*, chapter 7, pages 269–317, referred in text as "R&L". Cambridge University Press, New York, 2012.

I. S. Robinson. *Discovering the Ocean from Space: The Unique Applications of Satellite Oceanography*. Springer/Praxis Publishing, Berlin-Heidelberg, 2010.

B. Rodenborn, D. Kifer, H. P. Zhang, and H. L. Swinney. Harmonic generation by reflecting internal waves. *Phys. Fluids*, 23:026601, 2011.

L. H. Shih, J. R. Koseff, G. N. Ivey, and J. H. Ferziger. Parameterization of turbulent fluxes and scales using homogeneous sheared stably stratified turbulence simulations. *J. Fluid Mech.*, 525:193–214, 2005.

D. N. Slinn and J. J. Riley. Turbulent dynamics of a critically reflecting internal gravity wave. *Theor. Comp. Fluid Dyn.*, 11:281–303, 1998.

A. Soloviev and R. Lukas. *The Near-Surface Layer of the Ocean*. Springer, Dordrecht, 2006.

G. R. Spedding. The evolution of initially turbulent bluff-body wakes at high internal Froude number. *J. Fluid Mech.*, 337:283–301, 1997.

G. R. Spedding. Anisotropy in turbulence profiles of stratified wakes. *Phys. Fluids*, 13:2361–2372, 2001.

G. R. Spedding. Vertical structure in stratified wakes with high initial Froude number. *J. Fluid Mech.*, 454:71–112, 2002.

G. R. Spedding. Wake signature detection. *Ann. Rev. Fluid Mech.*, 46:273–302, 2014.

G. R. Spedding, F. K. Browand, N. Huang, and S. R. Long. A 2-D complex wavelet analysis of an unsteady wind-generated surface-wave field. *Dyn. Atmos. Oceans*, 20:55–77, 1993.

G. R. Spedding, F. K. Browand, and A. M. Fincham. Turbulence, similarity scaling and vortex geometry in the wake of a towed sphere in a stably stratified fluids. *J. Fluid Mech.*, 314:53–103, 1996a.

G. R. Spedding, F. K. Browand, and A. M. Fincham. The long-time evolution of the initially turbulent wake of a sphere in a stable stratification. *Dyn. Atmos. Oceans*, 23:171–182, 1996b.

G. R. Spedding, F. K. Browand, R. Bell, and J. Chen. Internal waves from intermediate, or late-wake vortices. In *Stratified Flows I, Proceedings of the 5th International Symposium on Stratified Flows*, pages 113–118, University of British Columbia, Vancouver, 2000.

C. Staquet and J. Sommeria. Internal gravity waves: From instabilities to turbulence. *Annu. Rev. Fluid Mech.*, 34:559–593, 2002.

J. V. Steinbuck, J. R. Koseff, A. Genin, M. T. Stacey, and S. G. Monismith. Horizontal dispersion of ocean tracers in internal wave shear. *J. Geophys. Res.*, 116:C11031, 2011.

B. R. Sutherland. Internal gravity wave radiation into weakly stratified fluid. *Phys. Fluids*, 8:430, 1996.

B. R. Sutherland. Finite-amplitude internal wavepacket dispersion and breaking. *J. Fluid Mech.*, 429:343–380, 2001.

B. R. Sutherland. *Internal Gravity Waves*. Cambridge University Press, New York, 2010.

B. R. Sutherland and P.F. Linden. Internal wave excitation from stratified flow over a thin barrier. *J. Fluid Mech.*, 377:223–252, 1998.

A. Tabaei and T. R. Akylas. Nonlinear internal gravity wave beams. *J. Fluid Mech.*, 482:141–161, 2003.

A. Tabaei, T. R. Akylas, and K. G. Lamb. Nonlinear effects in reflecting and colliding internal wave beams. *J. Fluid Mech.*, 526:217–243, 2005.

J. R. Taylor and S. Sarkar. Internal gravity waves generated by a turbulent bottom Ekman layer. *J. Fluid Mech.*, 590:331–354, 2007.

H. Tennekes and J. L. Lumley. *A First Course in Turbulence*. The MIT Press, Cambridge, 1972.

S. G. Teoh, G. N. Ivey, and J. Imberger. Laboratory study of the interaction between two internal wave rays. *J. Fluid Mech.*, 336:91–122, 1997.

N. H. Thomas and T. N. Stevenson. A similarity solution for viscous internal waves. *J. Fluid Mech.*, 54:495–506, 1972.

S. A. Thorpe. The excitation, dissipation, and interaction of internal waves in the deep ocean. *J. Geophys. Res.*, 80:328–338, 1975.

S. A. Thorpe. On the reflection of a train of finite-amplitude internal waves from a uniform slope. *J. Fluid Mech.*, 178:279–302, 1987.

S. A. Thorpe. On the interactions of internal waves reflecting from slopes. *J. Phys. Oceanogr.*, 27:2072–2078, 1997.

S. A. Thorpe. *The Turbulent Ocean*. Cambridge University Press, New York, 2005.

J. S. Turner. *Buoyancy Effects in Fluids*. Cambridge University Press, Cambridge, 1973.

S. Venayagamoorthy and D. Stretch. On the turbulent prandtl number in homogeneous stably stratified turbulence. *J. Fluid Mech.*, 644:359–369, 2010.

S. I. Voropayev, H. J. S. Fernando, S. A. Smirnov, and R. Morrison. On surface signatures generated by submerged momentum sources. *Phys. Fluids*, 19:076603, 2007.

S. I. Voropayev, H. J. S. Fernando, and C. Nath. Thermal and dynamic surface signatures of the wake of a submerged sphere. *J. Visual.*, 12:285, 2009.

B. Vreman, B. Geurts, and H. Kuerten. Large-eddy simulation of the turbulent mixing layer. *J. Fluid Mech.*, 339:357–390, 1997.

M. L. Waite. The vortex instability pathway in stratified turbulence. *J. Fluid Mech.*, 716:1–4, 2013.

M. L. Waite and P. Bartello. Stratified turbulence dominated by vortical motion. *J. Fluid Mech.*, 517:281–308, 2004.

G. Watson, R. D. Chapman, and J. R. Apel. Measurements of the internal wave wake of a ship in a highly stratified sea soch. *J. Geophys. Res.*, 97:9689–9703, 1992.

K. B. Winters and E. A. D'Asaro. Two-dimensional instability of finite amplitude internal gravity wave packets near a critical level. *J. Geophys. Res.*, 94:12709–12719, 1989.

S. Wunsch, H. Ku, I. Delwiche, and R. Awadallah. Simulations of nonlinear harmonic generation by an internal wave beam incident on a pycnocline. *Nonlinear Proc. Geophy.*, 21:855–868, 2014.

P. K. Yeung and S. B. Pope. An algorithm for tracking fluid particles in numerical simulations of homogeneous turbulence. *J. Comput. Phys.*, 79:373–416, 1988.

C. J. Zappa and A. T. Jessup. High resolution airborne infrared measurements of ocean skin temperature. *IEEE Geosci. Remote Sens. Lett.*, 2:146–150, 2005.

Q. Zhou and P. J. Diamessis. Reflection of an internal gravity wave beam off a horizontal free-slip surface. *Phys. Fluids*, 25:036601, referred to in text as "Z&D", 2013.

Q. Zhou and P. J. Diamessis. Lagrangian flows within reflecting internal waves at a horizontal free-slip surface. Submitted to *Phys. Fluids*, 2015a.

Q. Zhou and P. J. Diamessis. Surface manifestation of internal waves emitted by submerged localized stratified turbulence. Submitted to *J. Fluid Mech.*, 2015b.

O. Zikanov and D. N. Slinn. Along-slope current generation by obliquely incident internal waves. *J. Fluid Mech.*, 445:235–261, 2001.